A measurement of $\sigma\left(Z \to \mu\mu\right)$ using the LHCb detector at CERN

THE UNIVERSITY
of LIVERPOOL

Department of Physics

University of Liverpool

Thesis submitted in accordance with the requirements of the University of Liverpool for the degree of Doctor of Philosophy by

Emma Hicks

September 2012

Contents

List of Figures

List of Tables

Acknowledgements

Firstly, I would like to thank my supervisor Tara Shears for answering all of my questions, even the silly ones, with endless patience over the last four years. My second supervisor, David Hutchcroft, also deserves much thanks for helping with all things computer related.

A massive thank you must go to James Mylroie-Smith. Whether it be talking physics, cakes or random stories you made my time in the Liverpool office so much fun. Thanks also go to my occasional office companions, Stephanie and Abdi, many a laugh has been shared when we didn't want to work. Thanks to Tom, Matt, Dave and Dan in the Warwick office, for making me feel welcome in my last few months even though I was an interloper.

To my best friends in the world, Amy and Mike, thank you for keeping me sane through years of ups and downs. Especially to Mike, for looking after Theo when I couldn't and generally being awesome (I should take that back - you'll get a big head).

Mark, you made my time in Geneva so much fun. Thank you for putting up with my panics over the most ridiculous things. And for encouraging me to finish when I had almost lost all hope.

Lastly, I would like to thank my parents, I wouldn't be me without you. A special mention must go to Trog, for setting me those maths questions when I was little (and bored of counting apples). Without you giving me a love of "mathemagics" I would not be here.

Declaration

The work presented in this thesis is all my own work, unless it is specifically referenced to the contrary. This thesis has not been submitted, in any form, to this or any other university for another qualification.

Emma Hicks

Abstract

LHCb is one of four main experiments at the LHC in CERN. This thesis analyses 1.03 fb^{-1} of $\sqrt{s} = 7$ TeV data collected in 2011. Measurements of the $Z \to \mu\mu$ cross-section and a differential measurement with respect to Z boson rapidity are presented. The primary motivations for making these measurements are to probe the accuracy of the Standard Model and constrain theoretical parton distribution functions.

Final state radiation causes a downward shift in the reconstructed dimuon invariant mass and broadening in the peak. Reconstructing the radiated photon means the invariant mass distribution shift can be corrected for. Here final state radiation is implemented in LHCb simulation for the first time. It is used to study the effect on the reconstructed Z mass distribution. Selections are placed on the distance between the photon and muon, and the photon P_T. The distribution is fitted to be 12% narrower than the non-reconstructed sample. The measured mass of the Z boson is increased from 91.047 GeV to 91.054 GeV.

The kinematic requirements placed on the muons are: both muons must have transverse momentum, $P_T > 20$ GeV; the dimuon invariant mass, $60 < M_{\mu\mu} < 120$ GeV; and their pseudorapidity, $2 < \eta_\mu < 4.5$. These selections are justified using simulation. Once the event requirements are imposed 56449 Z boson candidates are yielded. Background contamination is estimated using data driven methods where possible, and simulation. The number of background events in the signal region is estimated to be 254.9 ± 7.0. The signal efficiency is determined by analysing each source individually. The overall efficiency for measuring a $Z \to \mu\mu$ event is found to be 0.74 ± 0.02. Taking these results into consideration the cross-section is measured to be:

$$\sigma_{Z\to\mu\mu}\,(2 < \eta_\mu < 4.5,\ P_T^\mu > 20 \text{ GeV},\ 60 < M_{\mu\mu} < 120 \text{ GeV}) =$$
$$(74.2\ \pm 0.4\ (\text{stat})\ \pm 2.0\ (\text{sys})\ \pm 2.6\ (\text{lumi}))\ \text{pb}$$

A comparison with NLO theory predictions using CTEQ6.6 and MSTW2008 PDF sets is performed, and the above result is found to be consistent.

Chapter 1

Introduction

The Standard Model is one of the greatest achievements of modern science. It aims to describe the fundamental aspects of matter and energy. The electromagnetic and weak forces are successfully combined with the prediction of the photon, $W^{\pm}$ and Z^0, all of which have been validated experimentally. The Higgs mechanism has been waiting for the discovery of a fifth boson for over forty years. As of July, this too has been confirmed. One of the biggest stumbling blocks is the amount of CP violation observed in the universe. Theory does not predict the level of matter-antimatter asymmetry seen experimentally.

The LHCb experiment is one of four experiments at the LHC in CERN, and is dedicated to the study of CP violation in the $b-$quark sector. At the LHC, two proton beams are collided together at a centre-of-mass energy of 7 TeV. The work contained within this thesis is based on ~ 1 fb^{-1} of data collected in 2011.

The theoretical context of the physics involved in the measurements presented in this thesis are discussed in chapter 2. Chapter 3 details the setup of the LHCb detector. Particular attention is given to the specifics of how muons are identified. In chapter 4, the topic of final state radiation is introduced at length. A study of its effect on $Z \to \mu\mu$ events is conducted on simulated Monte Carlo. A complete analysis of the cross-section of $Z \to \mu\mu$

events is presented in chapter 5. This includes a differential measurement with respect to the Z boson rapidity, and comparisons with theoretical predictions. Chapter 6 summarises the results presented and concludes this thesis.

Additionally to the above for completeness extra figures have been added in the appendix 7. These detail extra cross-checks completed while carrying out the main analysis.

Chapter 2

Theoretical overview

In this chapter the Standard Model of particle physics is discussed. This theory describes the behaviour of fermions under the weak, electromagnetic and strong forces. Section 2.1 describes the main aspects of the Standard Model. The general mathematical framework of a gauge theory is discussed in section 2.2. Additional details on quantum electrodynamics, quantum chromodynamics and the electroweak force are given in sections 2.2.1, 2.2.2 and 2.2.3 respectively. Section 2.3 describes spontaneous symmetry breaking, which is followed by quark mixing and CP violation in 2.3.1. Details of the collisions taking place at LHC are discussed in section 2.4. This includes the parton model in 2.4.1 and parton distribution functions in 2.4.2. Production of Z bosons, theoretical predictions and final state radiation are described in 2.4.3, 2.4.4 and 2.4.5 respectively. Finally, $Z \to \mu\mu$ cross-section measurements from ATLAS and CMS in 2011 are highlighted in 2.5.

2.1 The Standard Model

Our present understanding of the fundamental particles and the mechanisms which bind them together are brought together under the Standard Model (SM). An overview of the theory is given below. For more information refer to references [1, 2, 3].

Generation	Quarks		Leptons	
I	up (u)	down (d)	electron (e)	neutrino e (ν_e)
II	charm (c)	strange (s)	muon (μ)	neutrino μ (ν_μ)
III	top (t)	beauty (b)	tau (τ)	neutrino τ (ν_τ)
Charge	+2/3	-1/3	-1	0

Table 2.1: Properties of fundamental fermions.

2.1.1 Particles and forces

Currently, the SM is built around 12 fermions and 4 bosons[1]. Fermions have half-integer spin and obey Fermi-Dirac statistics [4]. One fermion cannot occupy the same quantum numbers as another fermion in the same system. The 12 fermions can be either one of two types, quarks or leptons.

Quarks possess colour charge, of which there are 3 types, termed red, green and blue. They also carry fractional electric charge and weak charge. Leptons possess no colour charge, but do carry weak charge. The electron, muon and tau all carry -1 electric charge, and their neutrino partners (electron neutrino, muon neutrino and tau neutrino) have neutral electric charge.

The properties of the individual quarks and leptons are summarised in table 2.1. The fermions are arranged in 3 rows to reflect 3 generations. This starts with the lightest at the top, getting progressively heavier with each generation. Note that the absolute neutrino masses have not been measured experimentally.

There are 4 fundamental forces in nature; the strong force, electromagnetism, the weak force and gravity. The strong force acts on colour charge. It bonds gluons and quarks together to form mesons and baryons. The weak force acts on weak charge. It is through the weak interaction that heavy particles (e.g. top quarks, tau leptons) decay to their lighter counterparts (e.g. up quarks or electrons). It acts on all particles carrying weak charge. The

[1]Five, if the Higgs boson is included.

Force	Boson	Charge	Mass
Strong	gluon (g)	0	0
EM	photon (γ)	0	0
Weak	Z^0	0	91.2 GeV/c^2
	$W^{\pm}$	± 1	80.4 GeV/c^2

Table 2.2: Properties of the force carrying bosons.

electromagnetic force acts on all particles carrying electric charge. Gravity is not included in the SM, though it acts on all particles. In spite of this the SM is still an effective theory of fundamental interactions. This is because gravity is approximately 40 orders of magnitude weaker than the other forces at the energy scales studied.

Each of the forces described above are mediated by a boson, their properties are summarised in table 2.2. These are; gluons for the strong force, $W^{\pm}$ and Z^0 for the weak force and photons for electromagnetism. An additional boson, the Higgs boson, is associated with the Higgs mechanism (more details are given in section 2.3). Gravitation is postulated to have a spin-2 mediator called the graviton.

2.1.2 Issues

Although a very successful theory in itself the SM has some problems, which cannot be overcome simply. In this section some shortcomings will be presented.

- Masses - The SM does not postulate the absolute mass of any particle. Instead they must be input in an ad hoc way.
- Gravity - Gravity can't be described with a quantum field theory like the other forces.
- Hierarchy problem - There is no explanation for why there should be two very distinct mass scales; the Planck scale[2] at 10^{19} GeV, and the

[2]In natural units $\hbar = c = 1$, so mass, momentum and energy are all expressed in eV.

electroweak scale at ~ 100 GeV .

- Matter anti-matter asymmetry - The SM does not account for the asymmetry between matter and anti-matter. This is what the LHCb experiment was designed to investigate. More information is given in section 2.3.1.

2.2 Field theory

The mathematical framework for the SM is quantum field theory. A quantum field is a quantum mechanical system which has many, or infinite degrees of freedom at any point in space.

A Lagrangian is the equation defined classically as the difference between total potential energy and kinetic energy [5]. Equation 2.1, is the quantum Lagrangian of a free spin-1/2 particle. The particle has rest mass m, where $\bar{\psi}$ is the complex conjugate transpose of the fermion wave-function ψ. γ is a matrix, μ is an implicit summation over 3 space-components and 1 time-component, and δ is the partial derivative with respect to μ [6],

$$L = \bar{\psi}(i\gamma^{\mu}\delta_{\mu} - m)\psi. \tag{2.1}$$

This equation is modified in the SM to reflect the respective properties and behaviour of quantum electrodynamics (QED), electroweak theory (EW) and quantum chromodynamics (QCD).

2.2.1 Quantum electrodynamics

Equation 2.1 is invariant under global space-time transformations of the field, meaning $\psi \rightarrow \psi' = e^{-i\omega}\psi$ and $\bar{\psi} \rightarrow \bar{\psi}' e^{-i\omega}\bar{\psi}$ where ω is an arbitrary phase. A local gauge transformation, shown in equation 2.2 [2], is where the wave-function is multiplied by an arbitrary phase, $\alpha(x,t)$, that can change with distance, x and time, t,

$$\psi(x,t) \rightarrow \psi'(x,t) = e^{i\alpha(x,t)}\psi(x,t), \tag{2.2}$$

where $\psi(x,t)$ and $\psi'(x,t)$ are the wave-function and transformed wave-function respectively. However, equation 2.1 is not invariant under such a transformation, as shown by equation 2.3.

$$\delta_\mu \rightarrow \delta_\mu(e^{i\omega(x)}\psi) = e^{i\omega(x)}(\delta_\mu + i\delta_\mu\omega(x))\psi \tag{2.3}$$

In order to restore invariance at the local level additional terms must be added to the original Lagrangian. This is achieved by adding a vector field, A_μ and a covariant derivative, D_μ, which transform as shown in equations 2.4 and 2.5.

$$A_\mu \rightarrow A_\mu - \frac{1}{e}\delta_\mu\omega \tag{2.4}$$

$$D_\mu = [\delta_\mu + ieA_\mu] \tag{2.5}$$

Physically, A_μ is interpreted as the coupling between a fermion with e-electric charge and the electromagnetic field. It is the mediator, the photon (γ). The covariant derivative replaces the partial derivative in equation 2.1 to give equation 2.6.

$$L = \bar{\psi}(i\gamma^\mu D_\mu - m)\psi \tag{2.6}$$

For A_μ to be a true propagating field an extra gauge invariant kinematic term is added, known as the field strength tensor shown in equation 2.7. This describes the energy stored within the interacting fields.

$$F_{\mu\nu} = \delta_\mu A_\nu - \delta_\nu A_\mu \tag{2.7}$$

All of these terms make the final QED gauge invariant Lagrangian (shown in equation 2.8), which describes all electromagnetic interactions. One can see that for QED the addition of a mass term for the photon of the form $\frac{1}{2}m^2 A_\mu A^\mu$, is forbidden as it would lead to a non-gauge invariant Lagrangian.

Experimentally, for the photon this is true.

$$L = \bar{\psi}(i\gamma^{\mu}D_{\mu} - m)\psi - \frac{1}{4}F_{\mu\nu}F^{\mu\nu} \tag{2.8}$$

2.2.2 Quantum chromodynamics

The strong force (QCD) is described in similar way to QED, although it is more complicated to include the three types of colour charge [7]. The QCD Lagrangian is shown in equation 2.9:

$$L = \sum_{f} \bar{q_f}(x)(i\gamma_{\mu}D^{\mu} - m_f)q_f(x) - \frac{1}{4}G^{a}_{\mu\nu}(x)G^{\mu\nu}_{a}(x), \tag{2.9}$$

where $q(x)$ is the quark field, f is the summation over quark flavour, m_f is the corresponding quark mass and $G^{\mu\nu}_{a}(x)$ is the gluonic field strength tensor, directly analogous to the photon field strength tensor in equation 2.7. The covariant derivative, D^{μ} is defined as:

$$D^{\mu}q = \left(\delta_{\mu} - ig_s\left(\frac{\lambda_a}{2}\right)A_{\mu}\right)q, \tag{2.10}$$

where g_s is a coupling constant, A^{μ} is the gluon field and λ_a is the QCD scale.

The main difference between equations 2.8 and 2.9 arises from the mediators. In QED the photon does not carry electric charge, whereas in QCD the gluons do carry colour charge. Thus, gluons can interact with themselves. QCD is a non-Abelian gauge theory which has two main consequences, confinement and asymptotic freedom.

Confinement means that the strength of the strong force between two quarks increases as they are separated. Theoretically it would require infinite energy to separate quarks. It follows that quarks are never found individually, only bound within hadrons.

Asymptotic freedom means at very high energy, quarks and gluons interact very weakly and the strength of the strong force at this scale is small. This means that within the hadron, quarks are essentially free.

2.2.3 Electroweak theory

Experimentally it has been observed that the charged weak force acts only on particles with left-handed helicity[3]. The neutral weak force acts on both left and right-handed fermions [8].

Left-handed fermions transform as doublets under the charged weak interaction. Shown here is each generation, taken from table 2.1, split into doublets of leptons and quarks,

$$\begin{bmatrix} \nu_e & u \\ e^- & d' \end{bmatrix}, \begin{bmatrix} \nu_\mu & c \\ \mu^- & s' \end{bmatrix}, \begin{bmatrix} \nu_\tau & t \\ \tau^- & b' \end{bmatrix}, \tag{2.11}$$

where each "down"-type quark has d' representing its weak eigenstate. The relationship between the quark mass eigenstate, d, and its weak eigenstate, d' is given by the CKM (Cabibbo-Kobayashi-Maskawa) matrix and is discussed in more detail in section 2.3.1 and ref. [9].

Since the charged current acts on only the left-handed parts of the fermions shown in equation 2.11, it is convenient to split them up to show the differences. In the line below the left-handed leptons are shown on the left (denoted by L) in their doublets, and the right-handed leptons are shown in the middle and right (denoted by the R) in their singlet state.

$$\left\{ \begin{pmatrix} \nu_l \\ l^- \end{pmatrix}_L, \quad (\nu_l)_R, \quad l^-_R \right\} \tag{2.12}$$

[3]Helicity - the component of a particles spin in the direction of its motion. Left-handed helicity is defined as when the direction of the spin is anti-parallel to its momentum

Fields	$\psi_1(x)$	$\psi_2(x)$	$\psi_3(x)$
Quarks	$\begin{pmatrix} q_u \\ q_d \end{pmatrix}_L$	$(q_u)_R$	$(q_d)_R$
Leptons	$\begin{pmatrix} \nu_l \\ l^- \end{pmatrix}_L$	$(\nu_l)_R$	$(l^-)_R$

Table 2.3: Weak fields of electroweak theory.

Here ν_l can be any neutrino, and l any lepton. Additionally the same representation can be used for the quarks, where q_u is any "up"-type quark (up, charm or top) and q_d is any "down"-type quark (down, strange or bottom):

$$\left\{ \begin{pmatrix} q_u \\ q_d \end{pmatrix}_L, \quad (q_u)_R, \quad (q_d)_R \right\} \tag{2.13}$$

An additional quantity is assigned to each group of fermions called weak isospin, T_3. For "up"/ν_l type fermions it is +1/2, for "down"/l type fermions it is -1/2, for all right-handed fermions it is 0.

Following on from the notation set out in 2.12 and 2.13, the three sections of fermions can be represented by three different types of field; $\psi_1(x)$, $\psi_2(x)$ and $\psi_3(x)$ as shown in table 2.3.

Since, right-handed fermions interact differently to left-handed fermions under the weak force, to describe both handedness types at the same time another quantity called weak hypercharge, Y, is introduced.

$$Y = 2(Q - T_3) \tag{2.14}$$

Here Q is electric charge.

To describe the charged weak interaction three gauge invariant fields are introduced; W^1_μ, W^2_μ and W^3_μ. To describe the neutral weak interaction a

further field, B_μ is introduced. The physical bosons we observe in experiment $W^\pm$, Z^0 and γ, are related to these four fields as follows.

$$\begin{aligned} W_\mu^\pm &= (W_\mu^1 \pm iW_\mu^2)/\sqrt{2} \\ Z_\mu &= \cos\theta_W W_\mu^3 - sin\theta_W B_\mu \\ A_\mu &= \sin\theta_W W_\mu^3 + cos\theta_W B_\mu \end{aligned} \tag{2.15}$$

Here the Weinberg angle[4], θ_W is defined by:

$$\tan\theta_W = \frac{g'}{g}, \tag{2.16}$$

and g is the weak isospin coupling constant and g' is the weak hypercharge coupling constant.

The Lagrangian for the electroweak interaction is given by:

$$\begin{aligned} L &= i\bar{\psi}\gamma^\mu D_\mu\psi - \tfrac{1}{4}W_{\mu\nu}^a W_a^{\mu\nu} - \tfrac{1}{4}B_{\mu\nu}B^{\mu\nu} \\ &= i\bar{\psi}_R\gamma^\mu(\delta_\mu + ig'YB_\mu)\psi_R + i\bar{\psi}_L\gamma^\mu(\delta_\mu + igW_\mu^l + ig'YB_\mu)\psi_L \\ &\quad -\tfrac{1}{4}W_{\mu\nu}^a W_a^{\mu\nu} - \tfrac{1}{4}B_{\mu\nu}B^{\mu\nu} \end{aligned} \tag{2.17}$$

Here $W_{\mu\nu}^a$ and $B_{\mu\nu}$ are the field strength tensors:

$$\begin{aligned} W_{\mu\nu}^a &= \delta_\mu W_\nu^a - \delta_\nu W_\mu^a + g\epsilon_{abc}W_\mu^b W_\nu^c \\ B_{\mu\nu} &= \delta_\mu B_\nu - \delta_\nu B_\mu \end{aligned} \tag{2.18}$$

The first set of terms ($i\bar{\psi}_R\gamma^\mu(\delta_\mu + ig'YB_\mu)\psi_R$) allows the interaction of right-handed fermions. The second set of terms ($i\bar{\psi}_L\gamma^\mu(\delta_\mu + igW_\mu^l + ig'YB_\mu)\psi_L$) allows the interaction of the left-handed fermions. The kinematic terms ($\frac{1}{4}W_{\mu\nu}^a W_a^{\mu\nu}$ and $\frac{1}{4}B_{\mu\nu}B^{\mu\nu}$) are described in the last remaining

[4]The Weinberg angle is also known as the weak mixing angle. It occurs during spontaneous symmetry breaking which is explained in section 2.3.

Boson	Charge	Mass (GeV)
Z^0	0	91.188
$W^{\pm}$	± 1	80.399

Table 2.4: Summary of the weak gauge bosons and their masses.

part. This Lagrangian remains locally invariant only if the bosons are massless. Clearly another mechanism is needed to incorporate the masses we see in experiment (shown in table 2.4) in a gauge invariant way. The next section describes how this is achieved with the Higgs mechanism.

2.3 Spontaneous symmetry breaking

To include mass terms in the EW theory in a gauge invariant manner the Higgs mechanism [10] is introduced. Here the boson fields of the EW theory interact with a scalar field, Φ, to produce the masses needed. Φ is a doublet made up of one complex and one neutral scalar field.

$$\Phi \equiv \begin{pmatrix} \phi^{(+)}(x) \\ \phi^{(0)}(x) \end{pmatrix} = \frac{1}{2} \begin{pmatrix} \phi_1(x) + i\phi_2(x) \\ \phi_3(x) + i\phi_4(x) \end{pmatrix} \tag{2.19}$$

This has a potential of the form:

$$V(\Phi) = \mu^2 \Phi^\dagger \Phi + \lambda (\Phi^\dagger \Phi)^2, \tag{2.20}$$

where λ and μ are constants.

For $\lambda > 0$, and $\mu^2 < 0$ the potential $V(\Phi)$ has a minimum at $\Phi = 0$. When $\mu^2 > 0$, the potential is no longer minimum at $\Phi = 0$ as can be seen in figure 2.1. This shows the distribution of the potential versus ϕ. The expectation value no longer lies at 0, but at a higher non-zero value.

$$|< 0 \mid \phi^{(0)} \mid 0 >| = \pm\sqrt{\frac{-\mu^2}{2\lambda}} = \pm\frac{v}{\sqrt{2}}, \tag{2.21}$$

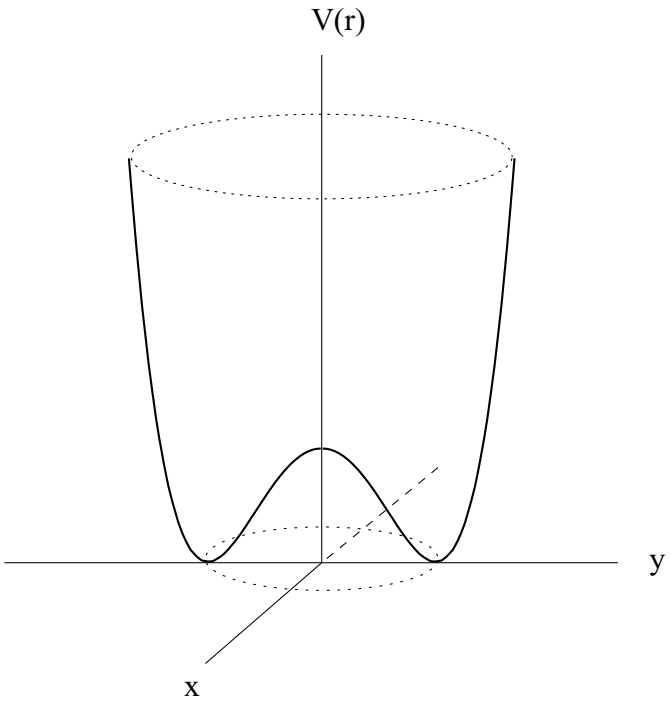

Figure 2.1: Higgs potential, V(Φ), versus ϕ shown in three dimensions when the constant, $\mu^2 > 0$. The "wine bottle" shape gives an infinite number of mimina in this regime [3].

where v is the Vacuum Expectation Value (VEV)[5].

As can be seen from figure 2.1 there are an infinite number of solutions to the ground state of this potential. By arbitrarily choosing one of these minimum ground state values, the electroweak symmetry is broken. This is known as Spontaneous Symmetry Breaking (SSB) [10].

The Goldstone theorem, explained in ref. [11], states that for each generator there is an associated massless boson, called a Goldstone boson. The four parts of the scalar field shown in equation 2.19 give rise to four Goldstone

[5]A VEV of an operator is its average expected value in the vacuum.

bosons. Three of which will be massless, the last, known as the Higgs boson, has a mass, $M_H = \sqrt{2\lambda\nu^2}$. By using a unitary gauge transformation on the field $\Phi(x)$, the three massless bosons can be removed altogether, and instead the three gauge bosons ($W^{\pm}$ and Z^0) acquire mass. The Φ field can now be expressed as:

$$\Phi = \frac{1}{2}\begin{pmatrix} 0 \\ v + h(x) \end{pmatrix}, \tag{2.22}$$

where $h(x)$ is the Higgs field. The Lagrangian for the W_μ and B_μ can now be written to include the interaction with the Higgs field:

$$L = (D_\mu\Phi)^\dagger(D_\mu\Phi) - V(\Phi), \tag{2.23}$$

where the covariant derivative, D_μ now includes the four weak fields described in the last section:

$$D_\mu = \left(\delta_\mu - \frac{ig\sigma^a W_\mu^a}{2} - g'Y B_\mu\right), \tag{2.24}$$

and where σ_a are the Pauli matrices [3].

To form the complete electroweak Lagrangian all of the parts discussed above, L_{field} , $L_{fermions}$, and L_Φ are brought together. In addition the fermionic interaction with the Higgs field, L_{Yukawa}, is also required

$$L_{EW} = L_{field} + L_\Phi + L_{fermions} + L_{Yukawa} \tag{2.25}$$

where L_Φ is the Lagrangian shown in equation 2.23. L_{field} includes the kinetic terms described in equation 2.18 and is of the form:

$$L_{field} = -\frac{1}{4}W^a_{\mu\nu}W_a^{\mu\nu} - \frac{1}{4}B_{\mu\nu}B^{\mu\nu} \tag{2.26}$$

$L_{fermions}$ describes the interaction of fermions with the gauge fields, from equation 2.17:

$$L_{fermions} = \bar{\psi_L}\gamma_\mu D_\mu \psi_L + \bar{\psi_R}\gamma_\mu D_\mu \psi_R. \tag{2.27}$$

The last term, L_{Yukawa} describes how the fermions interact with the Higgs field and also gain mass,

$$L_{Yukawa} = g_f \bar{\psi} \Phi \psi \tag{2.28}$$

where g_f is the Yukawa coupling. This dictates the strength on the coupling, and therefore the mass of the fermion. The magnitude of the Yukawa coupling [12] is not predicted in the SM. Therefore it must be adjusted by hand for each fermionic mass that has been measured by experiment.

2.3.1 Quark mixing and CP violation

Quarks have been observed to not only change flavour under the exchange of $W^{\pm}$, but are also able to change generation (e.g. $s \rightarrow u$). This is allowed because of the mixing between weak and strong quark eigenstates, described in section 2.2.3. The mixing is parameterised by the CKM matrix, a 3×3 matrix which describes the mixing between quark generations, and hence how likely it is one quark flavour will change into another. This is shown in equation 2.29 [9]:

$$\begin{pmatrix} d' \\ s' \\ b' \end{pmatrix} = \begin{pmatrix} V_{ud} & V_{us} & V_{ub} \\ V_{cd} & V_{cs} & V_{cb} \\ V_{td} & V_{ts} & V_{tb} \end{pmatrix} \begin{pmatrix} d \\ s \\ b \end{pmatrix} \tag{2.29}$$

Here d', s' and b' are the weak eigenstates, and d, s and b are the corresponding strong mass eigenstates. In this formalism each element gives the relationship between two sets of quarks, for example V_{us} describes the coupling between a u and an s quark.

The charge operator, C, acts on the charge of a particle so that a negatively charged particle becomes a positively charged one. The parity operator, P, reverses spatial coordinates so $x \rightarrow -x$. If these two operators are combined they are known as a CP transformation. For example, under this type of transformation a right-handed electron would become a left-handed positron.

If the CP operator were completely symmetrical (i.e electrons transformed to positrons and vice-versa with the same probability) then matter and antimatter would be identical. CP asymmetries have been measured experimentally, however the mechanism by which CP violation occurs is not understood, though the amount of CP violation is contained within the CKM matrix. By studying the rate of decay of particles and antiparticles of the same species more information can be determined about CP violation.

2.4 Physics of LHC collisions

This section will briefly cover the techniques used to predict processes occurring at the LHC.

2.4.1 The parton model and factorisation

The parton model was proposed by Richard Feynman in 1969 [13] as a way of breaking down high energy collisions into calculable interactions. A proton with sufficiently high energy can be thought of as being made up of independent "partons" which only interact very weakly with each other, see fig. 2.2. Hence, we can model them as being free in calculations.

The factorisation theorem [14] is the theorem that realises the parton model in QCD. At leading order the physics resulting from hadron-hadron interactions can be broken down to the product of the composite partonic level cross-sections. A generalised expression for the first order cross-section of a hadronic initial state collision (A and B) into final state Y is given by;

$$\sigma(AB \to Y) = \int dx_a \int dx_b f_f(a/A) f_{\bar{f}}(b/B) \sigma(ab \to Y) \tag{2.30}$$

where a and b are the two individual partons taking part in the process, $f(a/A)$ and $f(b/B)$ are parton distribution functions. $\sigma(ab \to Y)$ is the individual parton cross-section into final state, Y. The pictorial representation of this process is shown in figure 2.3.

Figure 2.2: Parton model representation. Small dots are the valance quarks (down (red) and up (blue)) which only interact very weakly. The light blue represents the "sea" where quark pair production and gluons are found. Note that weakly interacting reflects the strength of the interaction and not the force.

2.4.2 Parton distribution functions

Parton distribution functions (PDFs) are a parameterisation of all of the constituent parts of the colliding hadrons. They are the probability density for finding a parton with a certain momentum fraction of the parent hadron, x, and the energy squared of the hard interaction, Q^2. There are functions describing the momentum distributions of u, $\bar{u}$, d, $\bar{d}$, c, $\bar{c}$, s, $\bar{s}$, b, $\bar{b}$ and g. An example of these are shown in figure 2.4 where the PDF is shown versus x at two different values of Q^2.

PDFs are parameterised from fits to experimental data. Predictions made in kinematic regions not covered by existing measurements must use extrapolation. This problem is solved by using DGLAP evolution [16]; equations that allow us to evolve the PDF sets from one Q^2 to another. Data gathered from different experiments (LHC and Tevatron) at the same x values but different Q^2 can be used to test the DGLAP evolution. There are several groups producing PDFs for the proton over a wide range of x and Q^2 values, testing their reliability, most notably the MSTW group [15], CTEQ [17] and

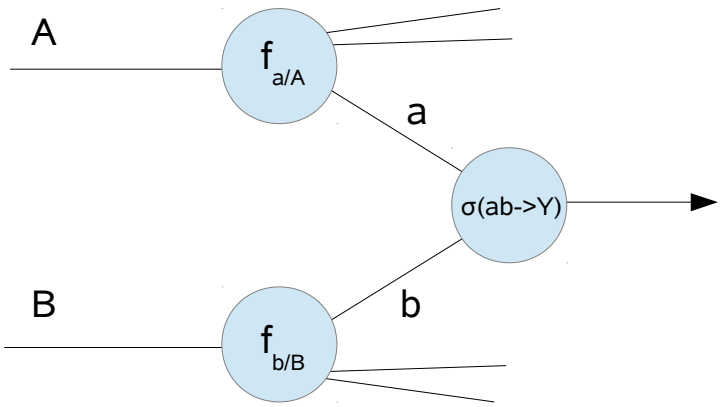

Figure 2.3: A pictorial representation of the process shown in equation 2.30.

NNPDF [18].

Z production at LHCb will probe both the high x values which arise from the valance quark and low x from the sea quark. These areas are shown in figure 2.5 where the LHCb kinematic region is shown in terms of x versus Q^2. Predictions of Z production will be described in the next section.

2.4.3 Z production

The mechanism by which $Z \rightarrow \mu\mu$ events are produced in high-energy hadron-hadron scattering is known as the Drell-Yan process [20]. It proceeds from the collision of a quark-antiquark pair. Predominantly this is mediated by a virtual photon (away from heavy $q\bar{q}$ resonances). With sufficient centre-of-mass energy it also occurs through the production of an on shell Z boson, shown in figure 2.6.

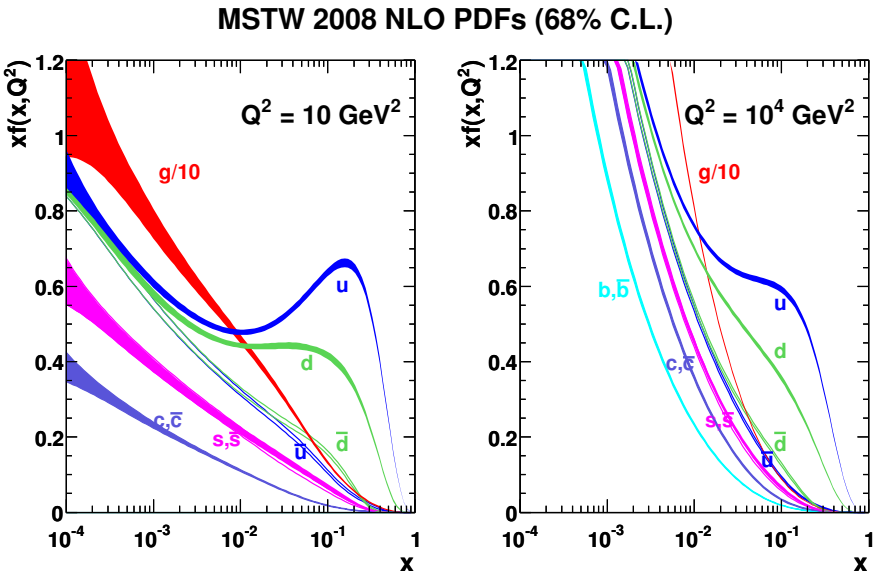

Figure 2.4: Individual PDF shapes, $xf(x, Q^2)$, for u, $\bar{u}$, d, $\bar{d}$, c, $\bar{c}$, s, $\bar{s}$, b, $\bar{b}$ and g as a function of x at different values of Q^2, the uncertainty in the PDF shapes is shown by the thickness of the lines (most obvious in the low x region of the gluon PDF) [15].

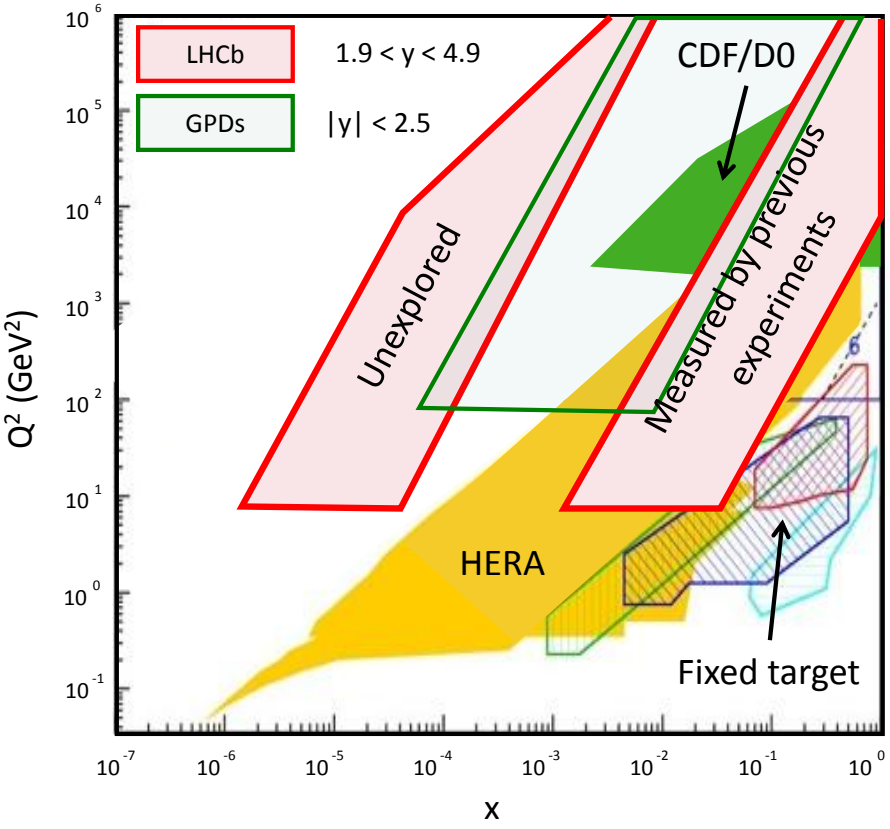

Figure 2.5: x versus Q^2 plane showing the region where experimental measurements have been made, and where LHCb will be able to probe [19]. Z bosons in LHCb will be primarily formed from one high-x quark and a lower-x anti-quark allowing us to probe the lower left corner of the unexplored region ($Q^2 \sim 10^3$ GeV).

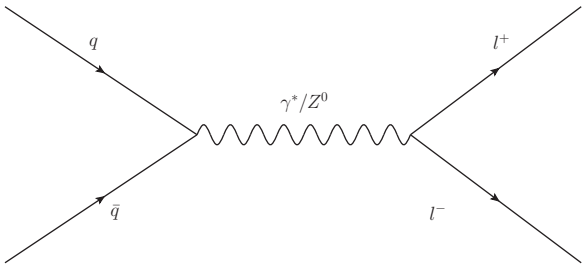

Figure 2.6: Feynman Diagram of Drell-Yan process. A quark-antiquark pair collides to produce a γ/Z^0, which then decays to a lepton-antilepton pair.

In the pp centre of mass frame the 4-momenta for the 2 protons are,

$$p_1 = (p, 0, 0, p) \text{ and } p_2 = (p, 0, 0, -p),$$

and they collide with energy $s = 4p^2$. If we ignore parton masses and transverse momentum, each colliding quark (antiquark) carries a fraction, x of that momentum, $x_1 p_1$ ($x_2 p_2$). It follows on from this that the mediating virtual photon has 4-momentum:

$$\begin{aligned} q = x_1 p_1 + x_2 p_2 = ((x_1 + x_2)p, 0, 0, (x_1 - x_2)p) \\ \text{and } q^2 = 4x_1 x_2 p^2 = x_1 x_2 s (= M^2). \end{aligned}$$

In this equation q^2 is also equal to M^2, the invariant mass of the resulting lepton pair. Given these variables we can express the cross section for the sub-process by:

$$\sigma(q_f \bar{q_f} \to l^+ l^-) = \frac{1}{3} Q_f^2 \frac{4\pi\alpha^2}{3 x_1 x_2 s}. \tag{2.31}$$

Where, Q_f^2 is the electromagnetic charge of the parton, and the $\frac{1}{3}$-factor accounts for the fact that the $q\bar{q}$ pair must be colourless to interact. α is the electromagnetic coupling constant. At the parton level equation 2.31 becomes dependent on q^2, and is modified to be:

$$\frac{d\sigma}{dq^2}(q_f \bar{q_f} \to l^+ l^-) = Q_f^2 \frac{4\pi\alpha^2}{9q^2} \delta(q^2 - x_1 x_2 s). \tag{2.32}$$

Where x_1, x_2 and s are as previously defined. The general cross-section as outlined in equation 2.30 can be determined for on-shell Z production by the addition of relevant PDFs and parton level cross-sections:

$$\begin{aligned} \sigma_{pp \to Z} = \int dx_1 \int dx_1 \hat{\sigma}_{q\bar{q} \to Z} \times \\ \textstyle\sum_q \{ f_{q/p_1}(x_1, Q^2) f_{\bar{q}/p_2}(x_2, Q^2) + f_{\bar{q}/p_1}(x_1, Q^2) f_{q/p_2}(x_2, Q^2) \}. \end{aligned} \tag{2.33}$$

All that is left for a complete cross-section calculation is to multiply by the relevant branching fraction for the final state being considered. For the

dimuon final state this is 3.36% [21].

The LHC collides two proton beams together (see chapter 3). Z bosons are predominantly produced through the combination of $u\bar{u}$ or $d\bar{d}$. This cannot proceed through the beam valance quarks because the proton is made up of uud. For Z bosons detected at LHCb, where the detection is in the forward region production proceeds through one valance quark and one sea antiquark. The quark travelling parallel to LHCb (positive z - see chapter 3) must have high x, and the quark travelling anti-parallel must have low x in order for the boson to be produced in the forward region.

2.4.4 Theoretical predictions

Theoretically Z production is known to NNLO ($\sim 1\%$) for the hard scatter. The uncertainty in the PDFs dominate the uncertainty in predictions. In the central region ($y < 2.5$)[6] these are known to $1 - 2\%$, but this increases to 5% at higher rapidities. Figure 2.7 shows the percentage uncertainty of the PDFs at different boson rapidities. It shows a sub-1% uncertainty up to around $y = 2$ and reduced precision at higher rapidities.

2.4.5 Final state radiation

At leading order the $Z \to \mu\mu$ process is as shown in figure 2.8. The leptons in the final state often also radiate a photon. This process is known as Final State Radiation (FSR) and is shown in figure 2.9. FSR is important to analyse because the photon reduces the momentum of one of the leptons, therefore reducing the overall reconstructed invariant mass of the Z boson. Any experimental measurement will include FSR, whereas predictions made with QCD generators do not. Therefore FSR must be taken into account to make the data sample consistent with the generated samples.

[6]Where y is the rapidity, defined by $y = \frac{1}{2} \ln \frac{E+P_z}{E-P_z}$.

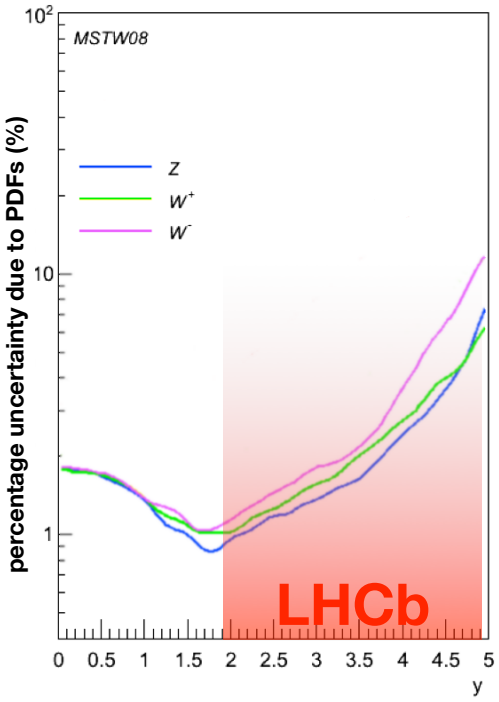

Figure 2.7: PDF uncertainty versus the boson rapidity from MSTW 2008 PDFs [19]. Z production is known in the low rapidity region to $\sim 1\%$, with an uncertainty that increase with boson rapidity. Here, the energy is $\sqrt{s} = 7$ GeV.

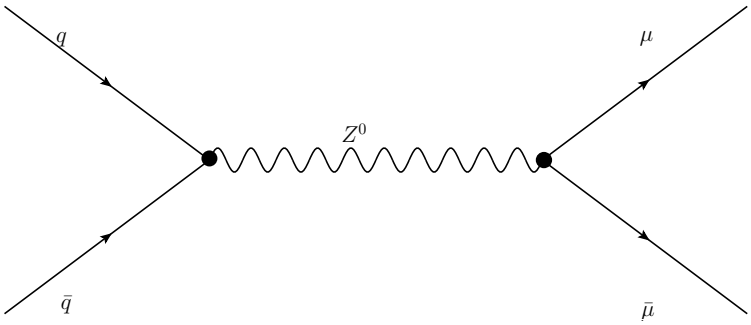

Figure 2.8: Leading order Z boson production Feynman diagram. A quark-antiquark pair collide to produce an on-shell Z boson, which subsequently decays into a muon-antimuon pair.

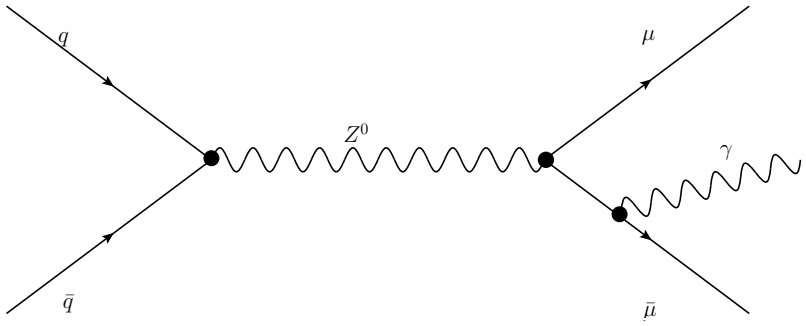

Figure 2.9: Next to leading order Feynman diagram of Z boson production with FSR. A quark-antiquark pair collide to produce an on-shell Z boson, which subsequently decays into a muon-antimuon pair with the additional photon radiation.

2.4.6 Generators

There are three QCD generators used to predict the $Z \to \mu\mu$ cross-section in this thesis. RESBOS [22] offers precision in boson transverse momentum measurements, which approaches NNLO accuracy. POWHEG [23] calculates with NLO precision while integrating with shower Monte Carlo programs. FEWZ [24] offers Z boson production at hadron colliders with NNLO accuracy in the strong coupling.

The simulation packages used to generate Z processes with FSR are different to those at leading order. Generator level calculations can be made with Horace [25], which has exact 1-loop corrections for the leading order production. To generate events which can be passed through the LHCb software chain, PHOTOS [26] is used alongside PYTHIA.

2.5 Survey of 2011 results

The $Z \to \mu\mu$ cross-section has been measured at both ATLAS and CMS using data collected in the 2010 running period. These results are summarised

here. For the complete analysis for ATLAS and CMS see references [27, 28] respectively.

2.5.1 ATLAS results

Using 35 pb^{-1} of data the total cross-section has been measured as $\sigma_{Z\to\mu\mu} = (0.935 \pm 0.009(\text{stat}) \pm 0.009(\text{sys}) \pm 0.032(\text{lumi}))$ nb. The differential cross-section with respect to the Z boson rapidity, y_Z, is shown in figure 2.10, and slightly overlaps the differential measurement made in this thesis. The kinematic selections placed on the muons in the final state are $P_T(\mu) > 20$ GeV, $66 < m_{\mu\mu} < 116$ GeV and both $|\eta_\mu| < 2.4$.

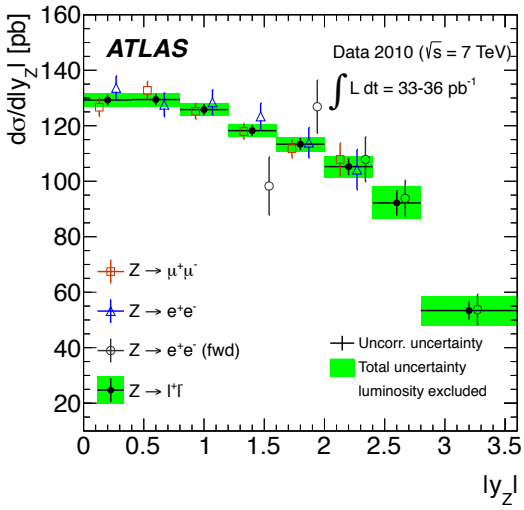

Figure 2.10: Differential $Z \to \mu\mu$ (red) cross-section measurement versus the Z boson rapidity, from 2010 ATLAS data [27].

2.5.2 CMS results

Using 36 pb^{-1} collected 2010, the differential Z cross-section has been measured with respect to the boson rapidity, shown in figure 2.11. Again the measurement slightly overlaps with this thesis. The total cross-section measured is $\sigma_{Z\to\mu\mu} = (0.968 \pm 0.008(\text{stat}) \pm 0.007(\text{sys}) \pm 0.039(\text{lumi}))$ nb. The

kinematic requirements made on muons in this sample are $60 < m_{\mu\mu} < 120$ GeV, $P_T(\mu) > 20$ GeV and $|\eta_\mu| < 2.1$.

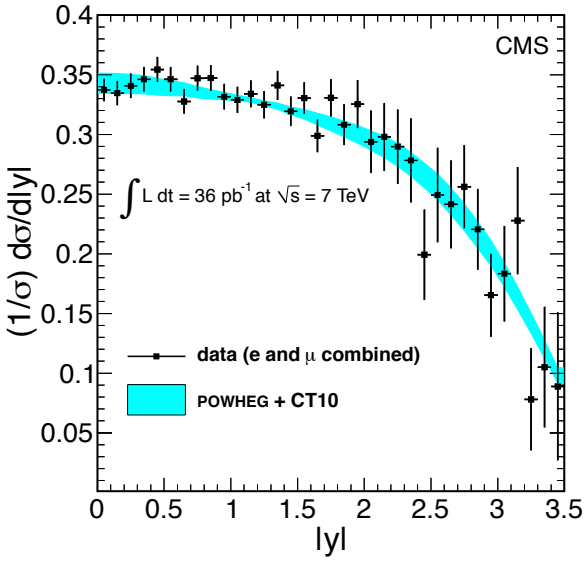

Figure 2.11: Differential Z (black) cross-section measurement (electrons and muons merged) versus the Z boson rapidity, from 2010 CMS data [28].

Chapter 3

The LHCb detector and the LHC accelerator

LHCb is one of four main experiments at the Large Hadron Collider (LHC). The LHC is at present and for the foreseeable future the highest energy and luminosity particle physics accelerator [29].

This chapter begins by describing the relevant details of the LHC in section 3.1. The LHCb detector is covered in section 3.2. Starting with luminosity levelling in section 3.2.1, followed by the tracking system in section 3.2.2. Particle identification is discussed in section 3.2.3 and the trigger system in section 3.2.4. The stripping is covered in section 3.2.5, track identification in 3.2.6 and muon identification in 3.2.7. Finally, a brief overview of the LHCb software chain is given in section 3.2.8.

3.1 The LHC

CERN (European Centre for Nuclear Research), the home of the LHC, is situated on the Franco-Swiss border approximately 7 miles north of the centre of Geneva. The LHC occupies the same tunnel as its predecessor, LEP. It is designed to collide protons together at a centre-of-mass energy, $\sqrt{s} = 14$ TeV, at four different locations around the beam ring, with a rate of 40 MHz [29]. This thesis will analyse the data collected up until the end of 2011,

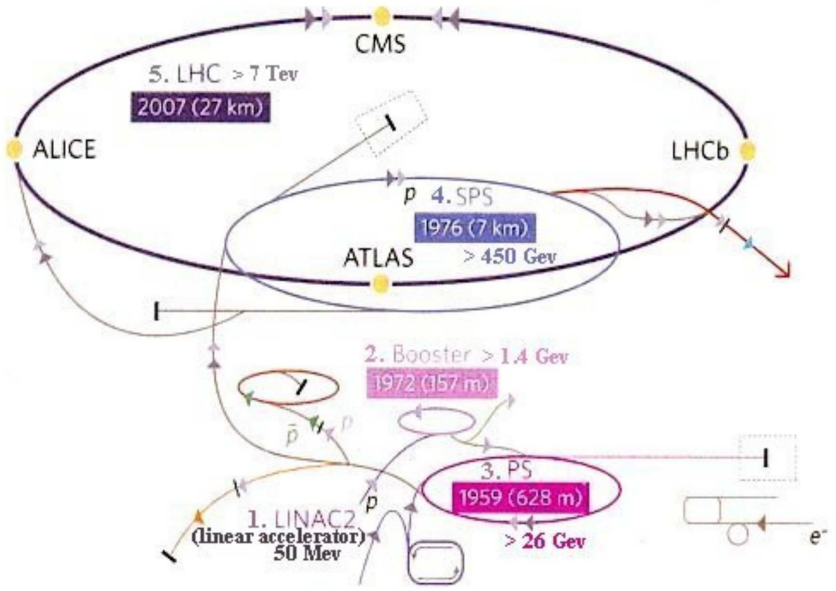

Figure 3.1: Figure showing the main LHC ring in dark blue, and the main acceleration steps the beam passes through to get there: SPS (Black); PS (Deep Pink); PSB (Light Pink); Linac2 (Black). The arrows show the beam direction and pipes which link the accelerators together [30].

taken at $\sqrt{s} = 7$ TeV.

3.1.1 Beam setup

Figure 3.1 shows each section of the LHC accelerator chain leading up to final injection into the LHC beam pipe.

Firstly, protons are collected by stripping the electrons from hydrogen atoms. From this the hydrogen nuclei are injected into the Linac-2 in pulsed beams. The nominal intensity of the source is 200 mA at a maximum energy of 750 keV. The Linac2 is 30 m long and accelerates to a maximum energy of 50 MeV and has a nominal intensity of 180 mA [31].

Next, the beam is transferred to the Proton Synchrotron Booster (PSB). The PSB splits the beam between four identical accelerator rings of 157 m

each, mounted on top of each other. Here the protons accelerate to 1.4 GeV, and each ring holds 1.05×10^{12} protons [32].

The next machine in the chain is the Proton Synchrotron (PS). The PS has a circumference of 628 m, and consists of 277 conventional magnets, including 100 bending dipoles. These are to maintain the beam in a ring as it accelerates to a final energy of 25 GeV. Once each of the four beams are accelerated in the PSB they are recombined into two beams and injected into the PS in two batches. Each injection pulse holds 0.83×10^{13} protons. As the beams are accelerated they are split into groups of protons called bunches. By the time the beams are ready for injection into the next synchrotron, there are 72 bunches each consisting of 10^{11} protons [33, 29].

Stage 4 is the Super Proton Synchrotron (SPS). This ring is approximately 7 km long and is made up of 1317 electromagnets, with 744 dipoles that accelerate protons to 450 GeV. The PS injects the bunches already formed into the SPS including some deliberate gaps. This is important because the magnets used for beam manipulation must be able to ramp up (or ramp down) in the gaps between proton bunches. For example if a beam needed to be ejected from the accelerator (a beam "dump"), a "kicker" magnet[1] must have time to power up in-between bunches. The dump kicker magnet takes 3μs to do this [34].

Lastly, the beams are transferred to the LHC beam line. The LHC is a two-ring superconducting hadron accelerator. The tunnel has eight straight and eight curved sections between 45 m and 175 m below ground on a 1.4% incline towards lake Geneva.

As protons are collided together (rather than proton-antiproton collisions) two separate rings are needed to accelerate the counter rotating beams. Of the eight potential crossing points on the LHC ring only four are occupied

[1]So-called because it kicks the beam off its original course.

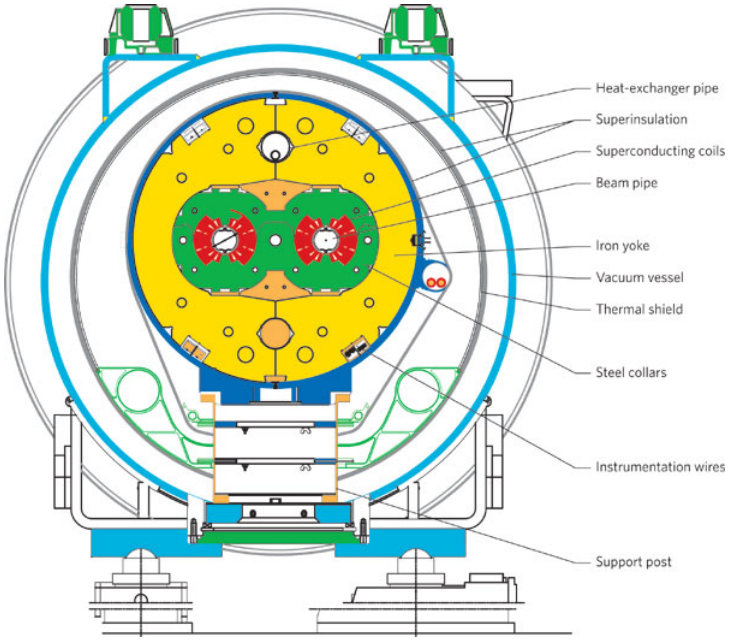

Figure 3.2: Cross-section of the LHC beam pipe. The vacuum area is within the outer blue line. Inside the vacuum shell are layers of insulation and an iron yoke. The superconducting coils used for beam direction are the red areas. The two white areas are the beam pipes [29].

with experiments. The other four crossings are suppressed to prevent extra beam disruption.

The LHC tunnel has an internal diameter of 3.7 m making it impossible to install two completely separate beam rings. Instead, twin bore magnets are used, all of which are cooled by superfluid helium at 2 K to allow the use of superconducting magnets. They operate at magnetic fields above 8 T. The 2-in-1 design makes the magnet structure (especially in the dipoles) complicated as the fields for both beams are coupled together. However, it is also advantageous as it allows the use of just one cooling system for both lines [29]. A cross-section of the beam apparatus is shown in figure 3.2.

Overall, the LHC has 1232 main dipole magnets (15 m long each), 3800 single aperture[2] and 1000 twin aperture corrector magnets. Insertion magnets are used at each of the eight crossing points mentioned above. Four of these are dedicated to experiments. The others are used for major beam systems (e.g. beam cleaning and dump). Beam cleaning is very important to protect the magnets from being damaged by protons straying from the main beam. This is achieved by passing the beams through collimators which allow only the central portion of the beam past.

3.2 LHCb

The Large Hadron Collider Beauty experiment (LHCb) [35] is a single-arm spectrometer covering a forward angle from 10 mrad to 300 mrad. This corresponds to a pseudorapidity[3] range of $1.8 < \eta < 4.9$. The primary physics objective for LHCb is to make high precision measurements of $B-$hadron decays. The forward design is justified because b and $\bar{b}$ quarks are predominantly produced in the same forward (or backward) cone. This is illustrated in figure 3.3.

LHCb is shown in figure 3.4. The design makes full use of the available space in the cavern by sitting off centre. The LHC displaces the interaction point from the centre of the cavern by 11.25 m to the left.

Starting closest to the beam interaction the main components are: a vertex detector (VELO); the first ring imaging Cherenchov detector (RICH); the Tracker Turicensis (TT); a dipole magnet; three tracking stations (T1, T2 and T3) which each consist of a silicon inner tracker (IT) and gas straw tube outer tracker (OT); the second RICH (RICH-2); the first muon station (M1); the calorimeter system, made up of a scintillating pad detector (SPD), preshower detector (PS), an electromagnetic calorimeter (ECAL) and a hadronic calorimeter (HCAL); and finally the last four muon stations (M2-M5).

[2]An aperture in the magnet provides a space for the beam to travel through.

[3]Pseudorapidity $\eta = \frac{1}{2} \log \frac{|P|+P_z}{|P|-P_z}$.

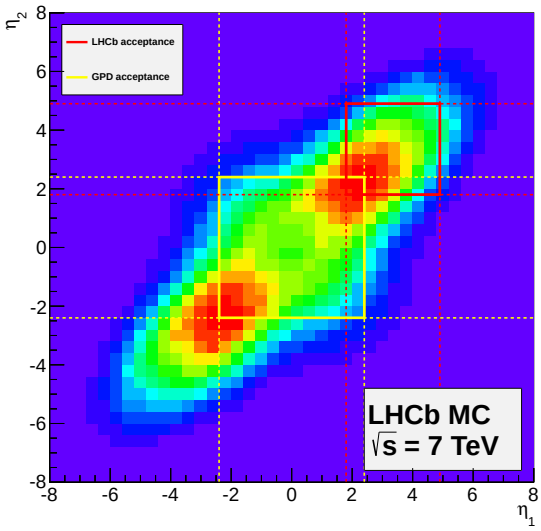

Figure 3.3: B hadron production with respect to η distribution (generated with PYTHIA8, CTEQ6 NLO). The LHCb coverage is within the red line and ATLAS/CMS coverage is within the yellow line. Red illustrates the area of highest rate of production. Each colour moving out indicates an increasingly lower rate, where purple is the lowest [36].

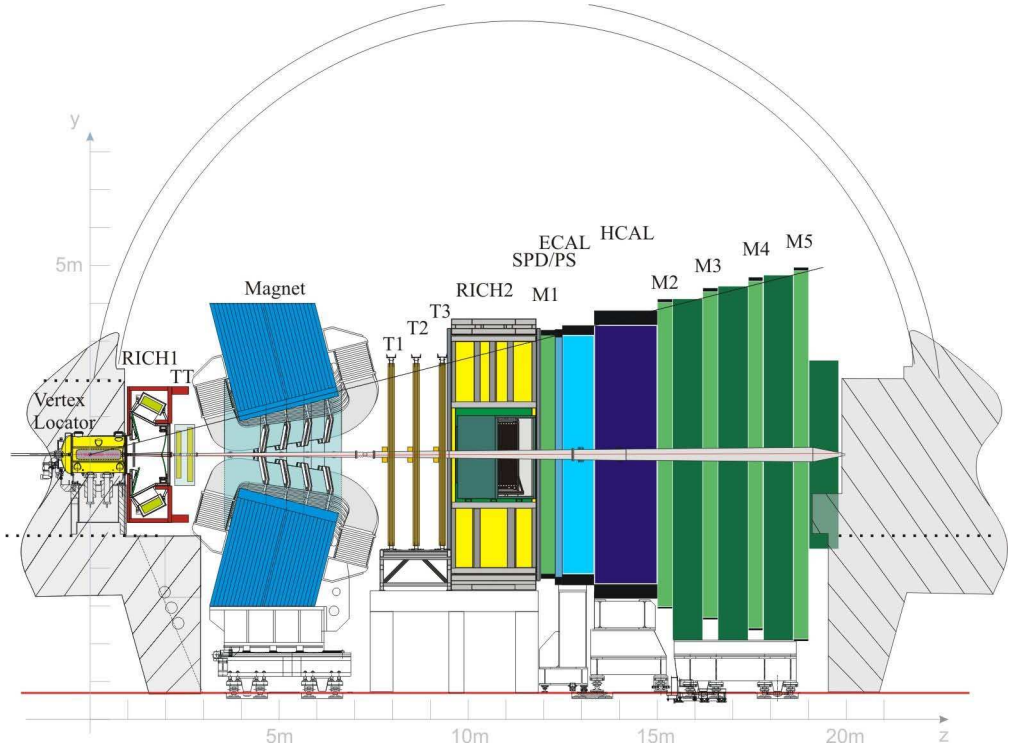

Figure 3.4: A schematic of the LHCb subdetector layout. The collisions take place in the far left in the VELO (Vertex Locator). Moving to the right there is the first RICH detector, Trigger Turicensis, the magnet, three tracking stations, the second RICH detector, the calorimetry system and lastly the muon chambers [35].

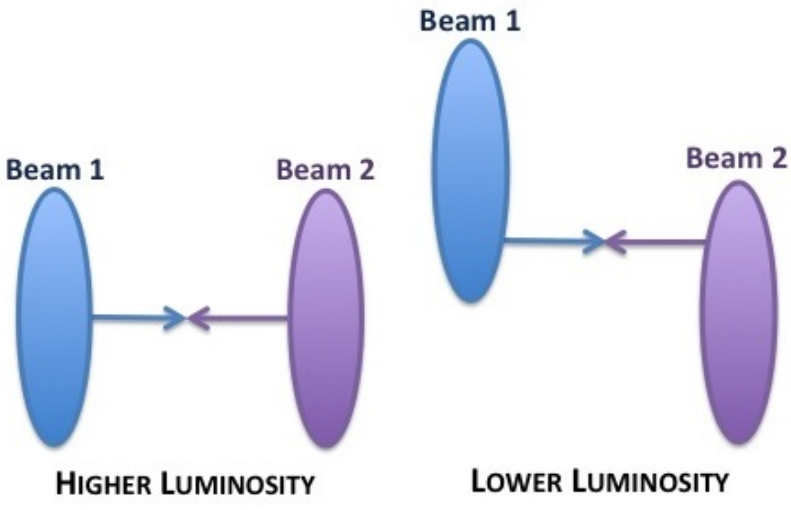

(a) Head on beam collision. (b) Offset beam collision.

Figure 3.5: Beams collide head on in ATLAS and CMS (a), whereas in (b) the beams are offset to reduce the number of interactions in LHCb.

3.2.1 Luminosity levelling

The nominal LHC luminosity is 10^{34} cm^{-2}s^{-1}. However, the LHCb detector is designed to run at a luminosity of 2×10^{32} cm^{-2}s^{-1}, a factor 50 reduction. This is to reduce the number of physics processes taking place in each collision and simplify the subsequent physics analyses. To achieve the lower instantaneous luminosity in LHCb while maintaining the higher value for other experiments, a process know as luminosity levelling is used. Here the beams no longer collide head on, but are shifted so only the edge of one beam collides with the edge of the other. This is shown in figure 3.5.

Figure 3.6 shows the progression of the instantaneous luminosity over a fill[4]. The LHCb has an almost constant instantaneous luminosity, whereas the luminosity drops exponentially for ATLAS and CMS while the beams are being collided. It may also be noted that LHCb has run above its design luminosity for most of the 2011 data collecting at a value around 3×10^{32} cm^{-2}s^{-1}.

[4]A fill is the name given to the time where the beams are colliding without being reinjected.

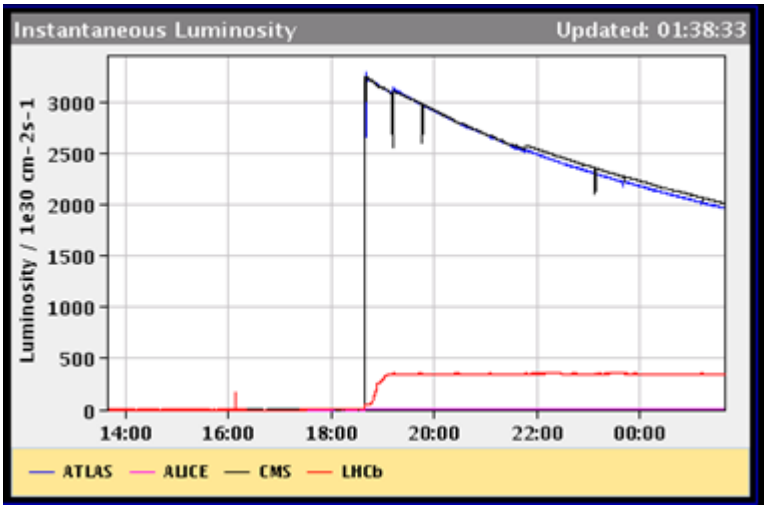

Figure 3.6: Instantaneous luminosity over a fill, ATLAS (blue), CMS (black) and LHCb (red). ATLAS and CMS instantaneous luminosity falls off exponentially after the beams start colliding, whereas the luminosity in LHCb remains constant [30].

3.2.2 Tracking

The tracking system at LHCb consists of the VELO, the magnet, and four tracking stations; the TT, T1, T2 and T3. The TT is located between the VELO and the magnet, while the other trackers are found downstream just in front of the RICH-2. The VELO and TT are both made completely out of silicon strips while the other tracking stations are a mixture of silicon and straw tubes. The IT is closest to the beam pipe, and therefore copes with the highest particle flux. It is also made of silicon strips, while the OT, further away from the beam pipe, is made of gas straw tubes.

The VELO

The closest detector to the interaction point is the VELO [37]. Its purpose is to give precise measurements of track coordinates close to the collision. In physics running conditions the active area is positioned 8 mm from the beam, shown in figure 3.7. However, being close to the beam during injection risks damaging the silicon with the unfocused beams. To prevent damage the

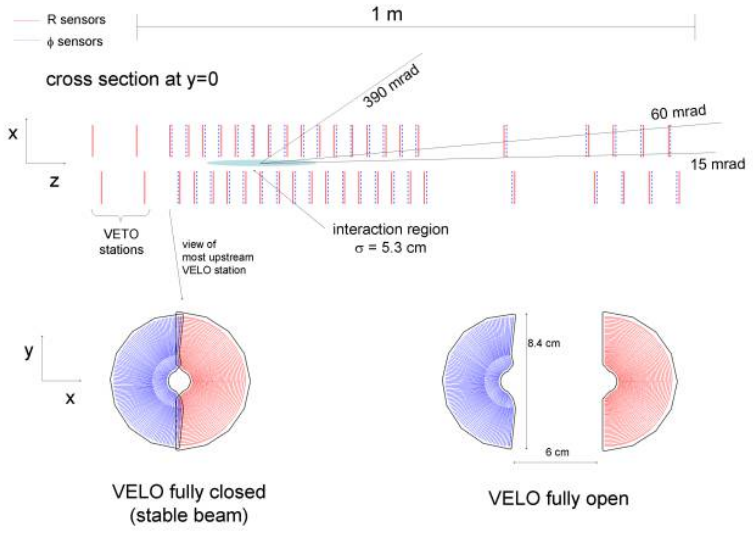

Figure 3.7: The setup of the VELO with R-sensors in red and ϕ-sensors in blue. The elongated blue oval in the central region shows the interaction point, and how differently angled tracks will travel through the sensors. The two lower figures illustrate how the two sides overlap when in the closed position [37].

VELO is retracted by 3 cm when the LHC is not in stable physics running conditions.

The VELO detector is made up of 42 semi-circular shaped modules, placed either side of the beam, and covers approximately 1 m along the z-axis. Each module is made up of two different silicon strip sensors. The first has the strips radially placed in semi-circular patterns to give a radial measurement (left side of figure 3.8) this is an "R-sensor". The second has the strips fanning out from the middle to give an angular measurement (right side of figure 3.8) this is a "ϕ-sensor". Pairs of these modules are fixed back-to-back to enable two-dimensional point reconstruction. The VELO layout is designed to minimise the amount of material a particle must travel through, while maximising the resolution of the measurement. All tracks within the pseudorapidity range of LHCb travel through at least three VELO modules.

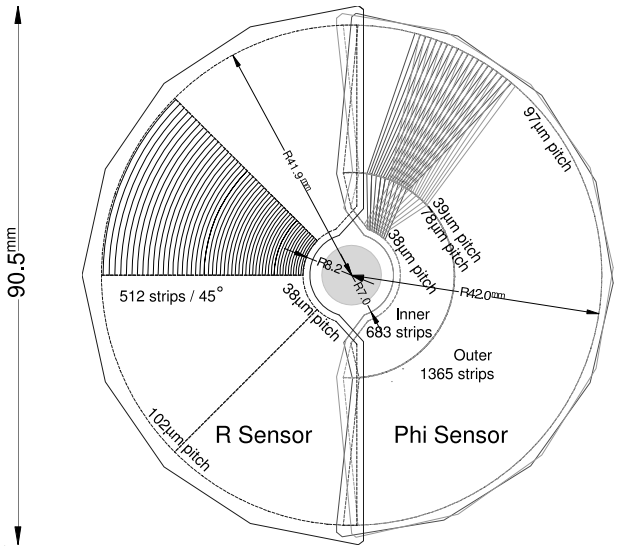

Figure 3.8: Radial strip formation on the ϕ-sensors (right sensor) and the circular structure on the R-sensors (left) [37].

The best hit resolution is approximately 5μm, taken directly from figure 3.9.

There are two additional stations of VELO sensors located upstream of the collision point. These are exactly the same as the VELO sensors already described but are used to determine the multiplicity of collisions. They are called "pile-up" sensors.

Tracker Turicensis

The TT [39] is sandwiched between the RICH-1 and the magnet. It consists of four layers of silicon micro-strip sensors arranged in two pairs, TTa and TTb, which are separated by 27 cm in the z-axis. To enable better three-

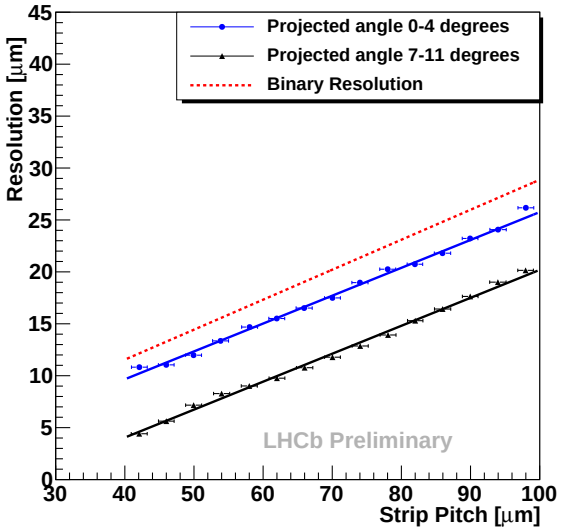

Figure 3.9: The track position resolution achieved with the VELO detector on long tracks with 2010 data shown as a function of strip pitch. The resolution is better for higher projected angle (so that the track travels across more than one strip) because more position information is gained from additional strips. Binary resolution is the resolution achieved with a binary 0/1 readout [38].

dimensional reconstruction the first and fourth layers are vertical, and the second (third) layers are rotated by $+5°$ ($-5°$). This scheme is named x-u-v-x for the differing vertical axis.

Each layer is made up of two modules joined together vertically to cover the region from 15 mrad to 250 mrad. Each module is structured in a 4-2-1 or 4-3 configuration, shown in figure 3.10. The 4-2-1 modules are situated around the beam pipe where the particle flux is highest, whereas those segments further away from the peak particle flux are in the 4-3 formation. This structure keeps the occupancy across the TT relatively constant.

The TT has two main functions. The first is to improve offline track reconstruction. Low momentum tracks which bend out of the acceptance of the other tracking stations can still be reconstructed if they leave hits in the TT. Secondly, the TT makes momentum measurements with an accuracy of about 20% as it is in the fringe of the magnetic field. This resolution does not compete with the full tracking system fit (VELO-TT-tracking stations) however, track reconstruction is a lot faster. Therefore the result can be used in the trigger.

Tracking stations

There are three other tracking stations, located between the magnet and RICH-2. These stations are split into two parts. The innermost part where the particle flux is highest is called the inner tracker. Further away from the beam pipe, where the track densities are much reduced, is the outer tracker.

Inner tracker

The IT [39] is a silicon micro-strip detector in the region closest to the beam pipe. Figure 3.11 shows the structure of the IT. Each station is made up of four separate silicon pieces. Like the TT, the detection layers are rotated in the x-u-v-x format.

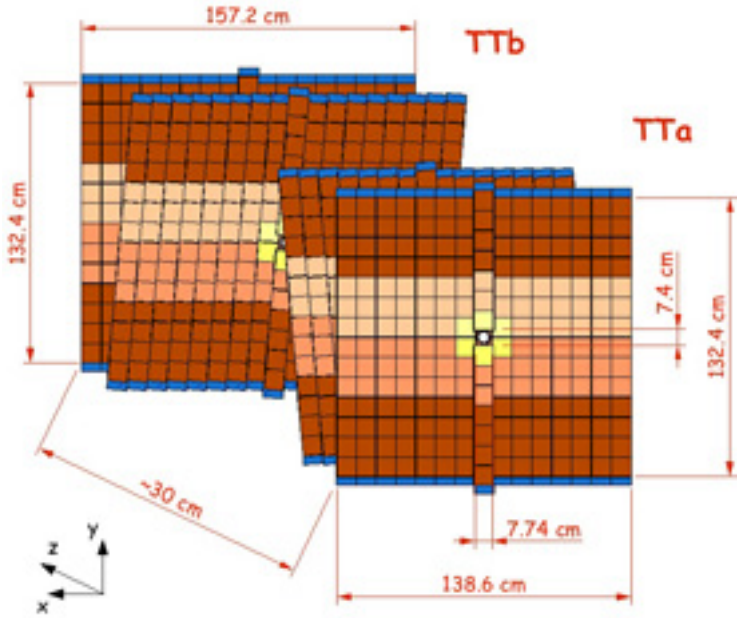

Figure 3.10: Schematic of the TT showing TTa at the front and TTb behind. Each layer is rotated slightly compared to its adjacent layer, known as x-u-v-x formation [40].

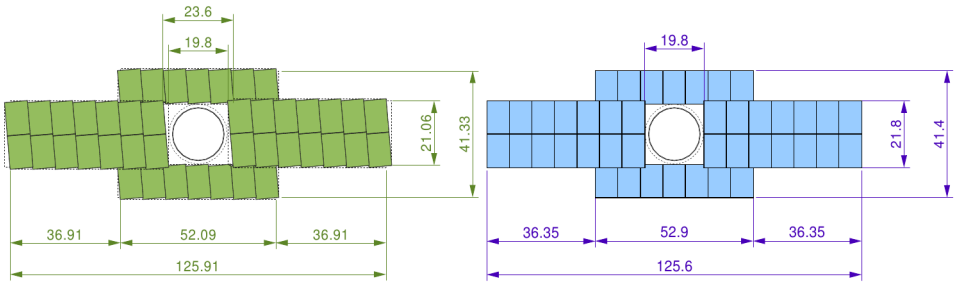

(a) The IT.

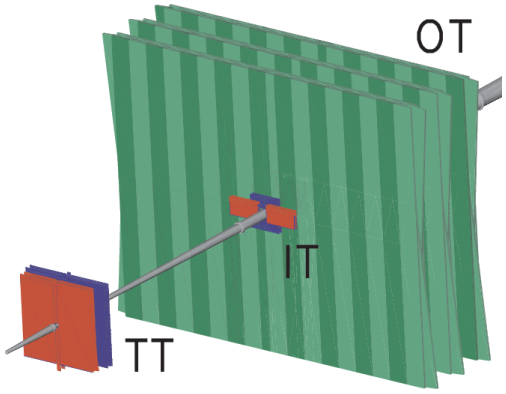

(b) The tracking system.

Figure 3.11: The Tracker setup, showing the shape of the IT (a). The OT is shown in (b) along with the position of the IT in the middle and the TT further upstream [40].

Outer tracker

The remaining area not covered by the silicon of the IT is instrumented by a straw-tube detector called the outer tracker [41]. Each module contains two staggered monolayers of drift-tubes and, like the TT and IT, follows the x-u-v-x structure.

The drift-tubes are filled with gas and operate with a bias voltage of 1.5kV. When a charged particle travels through a tube it ionises the gas. The newly free electrons move towards the anode and cause a signal pulse which can be recorded. The delay in such a signal is dominated by the drift time of the electrons ($\sim$50ns).

The magnet

The magnet [42] is required to allow precise measurement of particle momentum. The LHCb magnet is a warm dipole magnet with the main magnetic field in the y-direction. The overall integrated magnetic field is approximately 4 Tm, and is shown as a function of the z-axis in figure 3.12. Also illustrated are the different track definitions, which are described in section 3.2.6. The magnet polarity can also be changed (with configurations known as magnet-up and magnet-down) which is done regularly throughout the running of the LHC. This is important as it allows the investigation of any charge asymmetric responses from the detector.

3.2.3 Particle identification

The particle identification system uses input from three different sub-detectors. The RICH is designed to distinguish between kaons and pions. The calorimeters identify electromagnetically and hadronically interacting particles, and measure their energy. The muon system on the outer edge of the detector distinguishes muons from other particles.

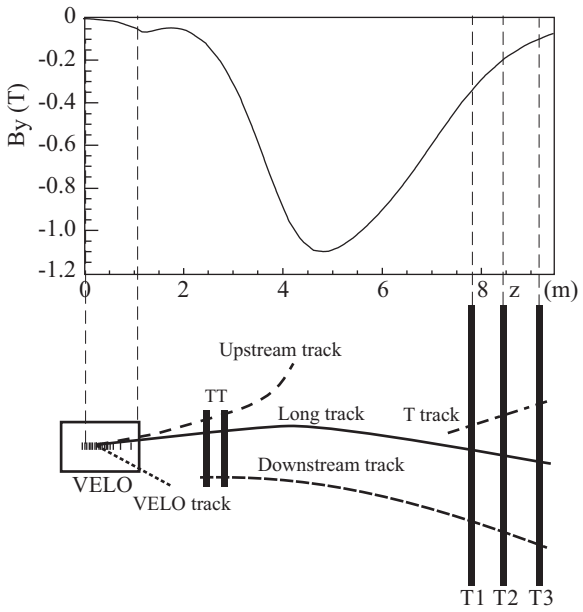

Figure 3.12: Mapping of the magnetic field along the z-axis. The different types of tracks defined in LHCb are illustrated underneath [42].

The RICH detector

The ability to distinguish between the hadron final states of B-decays is one of the most important requirements of a B-hadron experiment. Particularly being able to distinguish between kaons and pions. For example, the decays $B_d^0 \to \pi\pi$ and $B_d^0 \to K\pi$ are topologically identical. For LHCb to make precise measurements of such decays good identification of these particles is needed.

When a charged particle travels through a medium with a velocity, v, greater than the speed of light in that medium, it will emit photons in a cone at an angle to its direction of flight θ_c. The size of the angle is related to the velocity of the particle by the relation in equation 3.1, where c is the speed of light in a vacuum and n, the refractive index:

$$\cos\theta_c = \frac{c}{nv} \tag{3.1}$$

A velocity measurement along with a momentum measurement made by the tracking system can provide a mass measurement, and therefore identify the particle. LHCb has two such detectors, one positioned in between the VELO and magnet, the other after the last tracking station, these are called RICH-1 and RICH-2 respectively. RICH-1 measures low momentum particles between 1 GeV and 60 GeV and RICH-2 measures between 15 GeV and 100 GeV [43].

Calorimeters

The calorimeter system [44] has three main functions. Firstly, it selects photon, electron and hadron candidates for the level-0 trigger (more information on the triggering system is given in section 3.2.4). Secondly, it provides identification, energy and position information for photons, electrons and hadrons. Thirdly, it allows the reconstruction of π^0 and prompt photons for the study of B-decays. The calorimeter has four main parts: a scintillating pad detector (SPD); a pre-shower (PS); an electromagnetic calorimeter (ECAL); and a hadronic calorimeter (HCAL), placed in between the first two muon chambers.

Each calorimeter employs the same polystyrene scintillating tiles that are sensitive to the flight of charged particles. Scintillating layers are interleaved with an absorber such as iron. The scintillating light is then read-out using photomultiplier tubes.

The SPD/PS detector consists of a 15 mm lead converter, sandwiched between scintillating pads. It provides valuable information about the initial shower, which improves the identification abilities of the system. The SPD enables charged and neutral particles to be differentiated. It records the energy deposited in the initial scintillating pad. The lead wall is then enough to trigger an electromagnetic particle to shower but not enough to start a significant hadronic one. Hence, distinguishability between electrons and hadrons is achieved.

The ECAL records the rest of the electromagnetic shower. Layers of 4 mm thick scintillator and 2 mm lead are alternated over 42 cm so that an electromagnetic shower is contained within the ECAL. The HCAL utilises much thicker absorber layers (16 mm iron). The energy resolution given for each of the calorimeters is:

$$\frac{\sigma_E}{E}|_{ECAL} = \frac{10\%}{\sqrt{E}} \oplus 1\% \qquad \text{and} \qquad \frac{\sigma_E}{E}|_{HCAL} = \frac{80\%}{\sqrt{E}} \oplus 10\% \tag{3.2}$$

Muon system

Since muons do not produce hadronic showers and are less ionising than electrons, they are not absorbed by the calorimeter system, meaning they must be identified by other methods. The muon system is composed of five stations (M1 – M5) of rectangular shape, placed along the beam line. They cover an angular acceptance of 20 (16) mrad – 306 (258) mrad in the bending (non-bending) plane. M1 is placed in front of the calorimeter system to improve the transverse momentum, P_T, measurement in the trigger. The other stations are situated downstream of the calorimeters. Each station is interleaved with 80 cm of iron absorber as shown in figure 3.13. The minimum momentum a muon needs to traverse all five stations is approximately 6 GeV.

Each muon station is split into four regions (R1–R4). R1 is closest to the beam line and R4 is the furthest away, shown in figure 3.13. This allows the granularity to change with particle flux. For example, in R1 where most of the particles will travel the granularity is highest.

Primarily, the muon chambers are composed of Multi-Wire Proportional Chambers (MWPC). Each chamber is 5 mm across and filled with gas[5], with anode wires spaced along the centre (shown in figure 3.14). A muon travelling through the space will ionise the gas molecules, and due to a 3kV potential between the wires and the wall, electrons will move towards the wires. As

[5]A mixture of argon, CO_2 and CF_4.

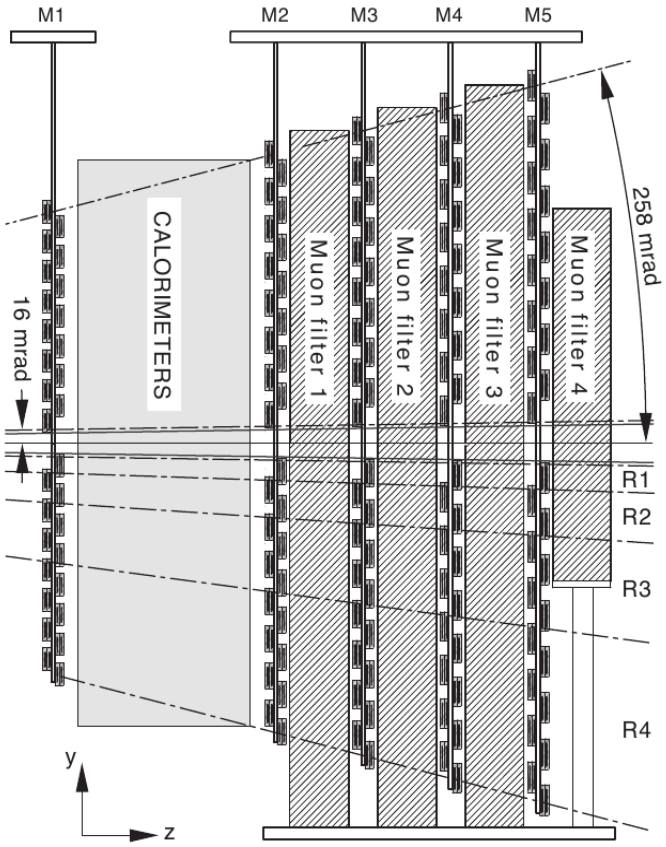

Figure 3.13: A schematic of the muon chamber setup, showing stations M1–M5 with the calorimeter and iron filters/absorbers interleaved between [45].

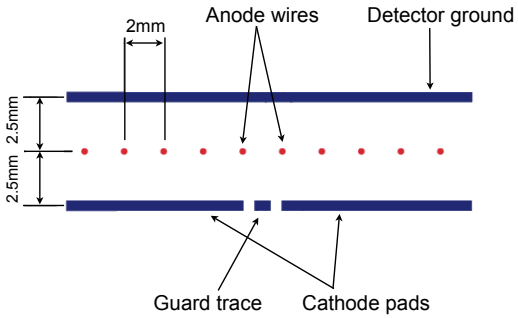

Figure 3.14: Schematic of the multi-wire proportional chambers.

the electrons move they ionise more gas, causing an electron avalanche that is detectable. This gives a time resolution of 5ns.

The central region of M1, however, utilises a different technology because it must cope with much higher particle flux than the other stations. It is formed of a triple Gas Electron Multiplier (GEM). The GEM is illustrated by figure 3.15. The strips across the cavity are kapton foils, which are sandwiched between a cathode and anode plane. The electric field across the gaps in the foil is much stronger than the drift space in-between the foils. When the particle travels through the first space it ionises the gas and causes electrons to drift along the field lines, ionising more gas as they travel. The electrons are then accelerated through the foils collecting more electrons, causing greater numbers to be collected at the readout.

3.2.4 Trigger system

Very few of the produced events in LHCb are of interest to physics analyses, and not all can be stored offline. To indicate which events should be stored, and which should not, a trigger system is used. Figure 3.16 shows the basic structure of the trigger. It is split into 3 parts, level-0 (L0), and the high level triggers (HLT1 and HLT2).

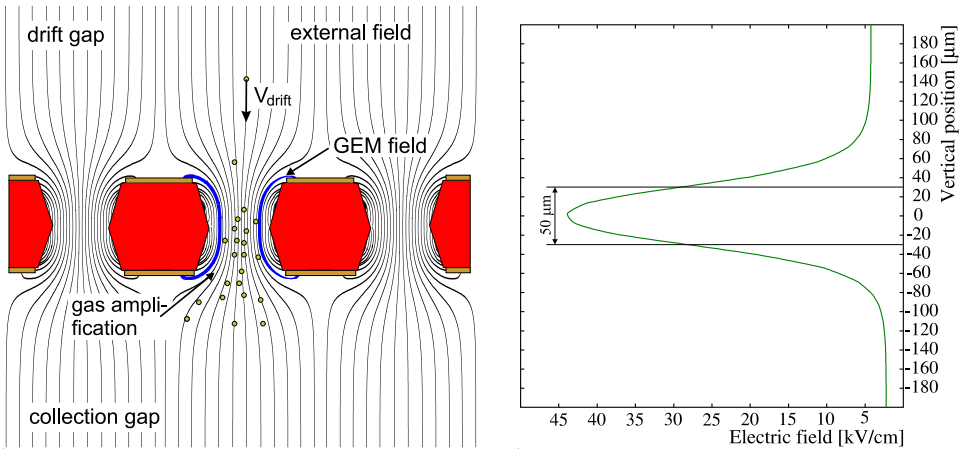

Figure 3.15: Single foil of a GEM detector showing the magnetic field changes and the movement of electrons this causes [46].

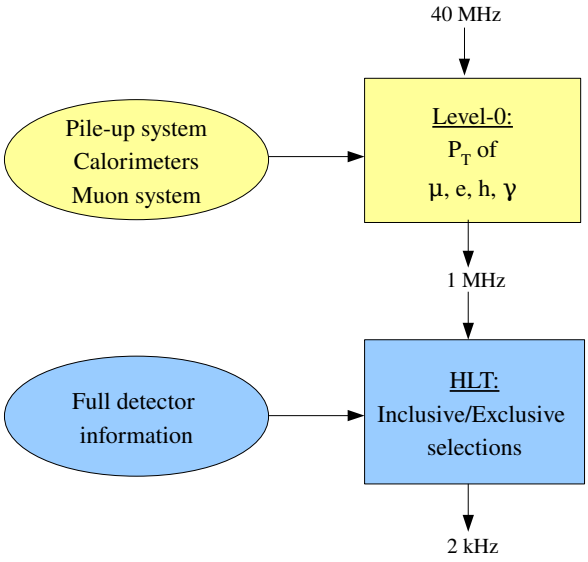

Figure 3.16: Flow diagram giving an overview of the LHCb trigger system [35].

Level-0 trigger

The L0 trigger is hardware based. It runs online with the detector to reduce the event rate by 90%, from 10 MHz to 1 MHz. A decision is reached with a fixed latency of 4 μs. Particle collection, cable delays and electronics account for 2 μs, thus the central L0 has 2 μs to come to a decision on each collision.

High level triggers

The HLT runs on the output of the L0. The HLT could theoretically run a full offline analysis because it has access to the full reconstruction, but this would be very CPU intensive. Instead, the first stage of the HLT (HLT1) aims to reject the bulk of uninteresting events using more information than the L0 has access to. This includes VELO and T-station hits for charged particles, and the absence of these for neutral particle candidates. This stage further reduces the event rate to ∼30kHz. In addition to this, global event cuts (GECs) are implemented. These selections ensure an event has VELO hits < 10000, IT hits < 3000 and an SPD multiplicity < 600. This reduces the multiplicity of the events stored, and therefore the processing time.

Finally, the high level trigger (HLT2), allows triggers to take into account the whole event which can then be accepted or rejected based on more than one high energy track. For example, it can place cuts on invariant mass, or whether a particle originates from the primary vertex. The final event rate written to disk is ∼2 kHz.

3.2.5 Stripping

After the data has passed through the HLT to reduce the dataset size further, the events are stripped. Each decay mode required for an analysis has a dedicated stripping line which tightens the selections made by the HLT. For $Z \to \mu\mu$ the stripping line requires a long track (defined in section 3.2.6) and two muons with $P_T > 15$ GeV and an invariant mass, $M_{\mu\mu} > 40$ GeV. This step is run by DaVinci which is described in the software chain in section 3.2.8.

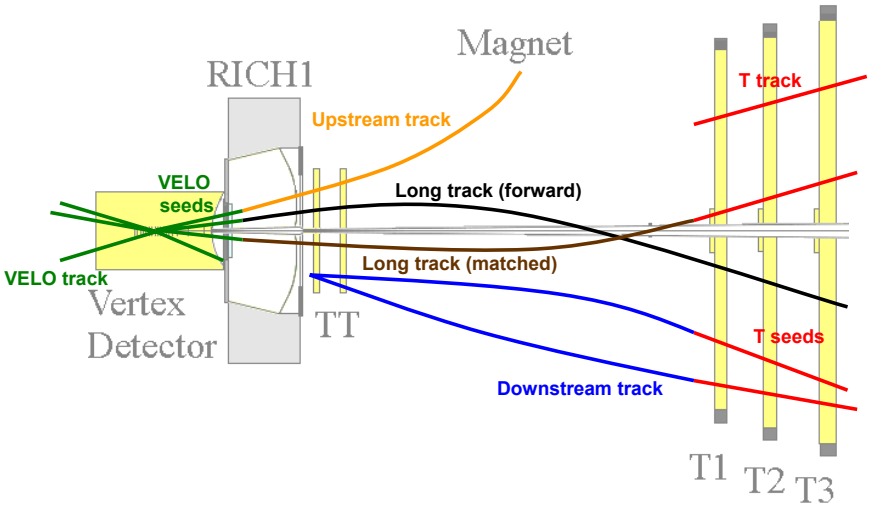

Figure 3.17: Subdetectors used when constructing the different definitions of track. VELO tracks are shown in green, T-tracks in red, upstream tracks show the original VELO track in green and the extrapolation to the TT hits in orange, downstream tracks are in blue with the attached T-track in red, the long tracks are shown in black for an unmatched track and brown when it is matched with a T-track [47].

3.2.6 Track identification

Tracks at LHCb are classified into five different categories. These are; VELO tracks, T-tracks, upstream, downstream and long tracks.

VELO tracks are tracks made from the hits in the VELO sensors, shown at the far left of figure 3.17. They are used for primary vertex reconstruction and have good IP resolution.

T-tracks are standalone tracks which use only hits in the tracking stations. The track is built by starting with a hit in one station and then adding hits in the surrounding stations to construct a track. This is shown in figure 3.17. These type of tracks are useful for RICH-2 performance monitoring, as the T stations surround it.

Upstream tracks take VELO tracks and add matching TT hits. These are also shown in figure 3.17. These tracks are lower momentum than downstream tracks, and are useful for RICH-1 performance monitoring.

Downstream tracks use T-tracks and match them with TT hits, and are shown in figure 3.17. These tracks have good momentum resolution and are used for K_{short} analyses.

Long tracks take VELO tracks and T tracks and match the two by extrapolating both sets towards each other to find TT hits. An example is shown in figure 3.17. Long tracks are the highest quality tracks for physics analyses, and have the best IP and momentum resolution.

The general tracking efficiency for VELO, T and long tracks from 2011 data are shown in figure 3.18.

3.2.7 Muon identification

Since the analysis in this thesis is based on the ability of the LHCb to accurately detect tracks and identify muon candidates, this section summarises the method of muon identification.

Online identification

The L0 muon trigger looks for tracks with high transverse momenta. Since the L0 doesn't have access to a reconstructed track, it performs an initial track finding sequence. As detailed in figure 3.19, for each hit in M3, a straight line is made through the interaction point and the seed hit. Fields of interest are opened to look for hits in M2, M4 and M5. If compatible hits are found a straight line is made through M2 and M3, and extrapolated to M1 to look for a hit there. M1, 2 and 3 are used to map back to the magnet. Then the p-kick method is used to make a momentum estimate. This technique relies on two assumptions; (1.) the particle originates from the primary vertex; (2.) that the magnetic field can be approximated to a

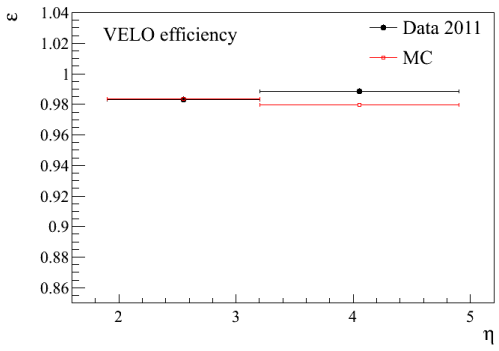

(a) VELO tracking efficiency 2011

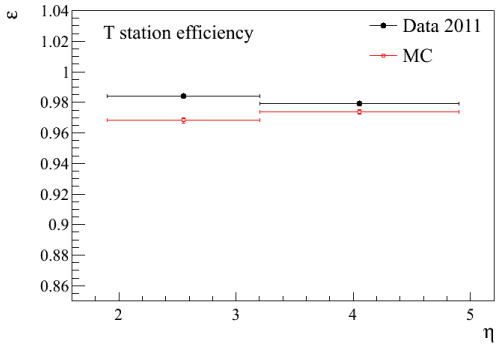

(b) T station tracking efficiency 2011

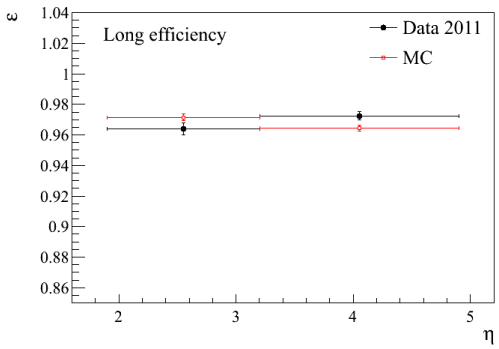

(c) Long track efficiency 2011

Figure 3.18: Efficiency for 2011 data and simulation with respect to η in (a) VELO tracks, (b) T station tracks and (c) long tracks. These are plotted in only two bins to keep the statistical uncertainty (shown) as low as possible [48].

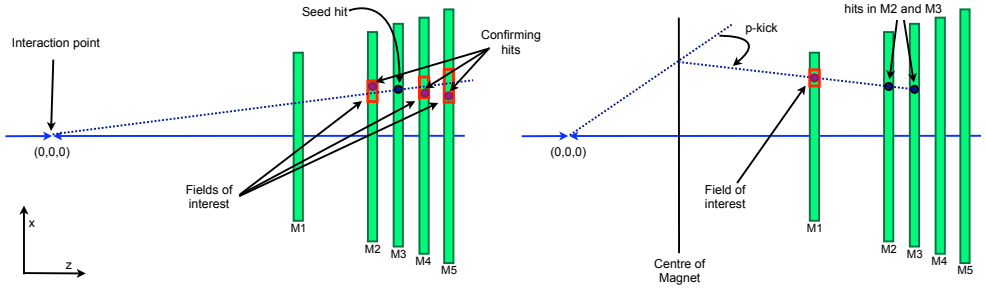

Figure 3.19: The basic principles of muon identification. Left: First stage of L0 track finding through M2–M5. Right: p-kick method used to estimate the muon momentum with accuracy of about 20% [45].

single instantaneous change in the particles trajectory (taken from the middle of the magnet in this case).

Offline identification

In the offline reconstruction long tracks are used to provide a muon track candidate. This track is then extrapolated through the muon system providing windows of interest in each of the stations to look for an associated hit. Tracks are only considered to be muons if they have a minimum number of hits across the stations. This number depends on the momentum of the track. For momentum, P between; 3 GeV $< P <$ 6 GeV, associated hits on M2 and M3 are needed; 6 GeV $< P <$ 10 GeV, hits are needed in M2 and M3 as well as one extra in M4 or M5; for $P >$ 10 GeV all muon chambers must have associated hits. Mis-identification is expected to be small, and is discussed in more detail in chapter 5.

3.2.8 LHCb software chain

There are many software packages utilised in LHCb for analysing Monte-Carlo or actual data. These are summarised briefly below.

Gauss

Gauss [49] is responsible for the generation of Monte-Carlo (MC). Firstly, the initial pp collision is modelled, and then the collision products are decayed. For $Z \to \mu\mu$ events this is carried out using PYTHIA 6.4 [50, 51], with the CTEQ6L PDF (leading order) set. Secondly, it simulates the decay products traversing the detector by using a modelled detector description, based on GEANT4 [52, 53].

Boole

Boole [54] digitises the output from the second stage of Gauss. It is responsible for making the MC look like data by including background from the LHC, giving a detector response and spillover events.

Brunel

Brunel [55] is responsible for the full event reconstruction. It can be used with real data or MC directly from Boole, and prepares events for full analysis.

Moore

Moore [56] is responsible for running the trigger described in section 3.2.4.

DaVinci

DaVinci [57] is the final stage of the software chain. It allows the user to place additional cuts on events, and decide what information is needed for the final analysis. DaVinci outputs a root file that can be used quickly and easily to get information.

Data

The average event size at LHCb is around 35kB. The dataset size for this $Z \to \mu\mu$ analysis is of the order 10GB.

Chapter 4

$Z \to \mu\mu$ and final state radiation

4.1 Introduction

Final state radiation (FSR) described in chapter 2, can make a big difference to the reconstruction of $Z \to \mu\mu$ events. In chapter 5 a correction factor is used to take into account muons which fail the selections because of the radiated photon. However, a reduced momentum also reduces the reconstructed Z mass and broadens the invariant mass distribution. By trying to detect FSR photons, and adding their momentum 4-vector into the reconstructed Z candidate, the smearing effect on the mass peak can be improved.

This chapter begins by surveying the result of studies performed by ATLAS in section 4.2. This is followed by a generator level study at LHCb in section 4.3. This continues onto a full simulation level study of FSR photon characteristics in 4.4. Then an initial FSR photon selection is discussed and performed in sections 4.4.5 and 4.5. Finally, concluding remarks are in section 4.6.

4.2 $Z + \gamma$ at ATLAS

Figure 4.1 shows the invariant mass peak of Z candidates with and without FSR photons included in the reconstruction. The data without FSR recon-

Quantity	Selection
Photon P_T	> 1 GeV
Cone distance	< 0.15
$E_{primary}/E_{cluster}$	> 0.15

Table 4.1: Selections made on the photon in an FSR event at ATLAS [58].

struction is in black and shows a long radiative tail where daughter muons have lost momentum. The red shows data with FSR included, which results in a narrower distribution, with the correct mean.

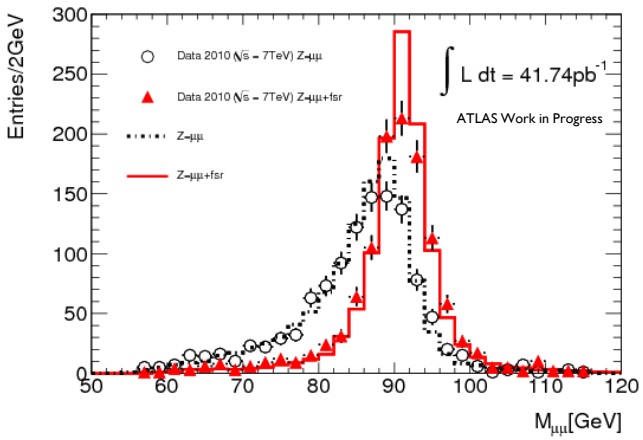

Figure 4.1: Invariant mass of the muons with and without the extra FSR photon reconstructed at ATLAS. The points are 2010 data and the dashed/full line is simulation [58].

There are three requirements made on FSR photons at ATLAS. The photon P_T must be greater than 1 GeV and the angle of flight (defined in section 4.4.2) between the photon and closest muon must be less than 0.15. The ratio of the primary energy deposit, in the ECAL, to the total cluster energy must be greater than 0.15. These requirements are tabulated in table 4.1.

4.3 FSR at LHCb

$Z \to \mu\mu$ events at LHCb are generated by PYTHIA [50]. By default FSR radiation is not included in this configuration. To enable the further analysis of FSR at LHCb, PHOTOS [59] is used alongside PYTHIA to simulate the additional radiative processes. PHOTOS includes contributions from single and double photon emission, both of these are shown in figure 4.2. Once PHOTOS is interfaced with the LHCb software the difference in event kinematics when FSR is included and when it is not are investigated.

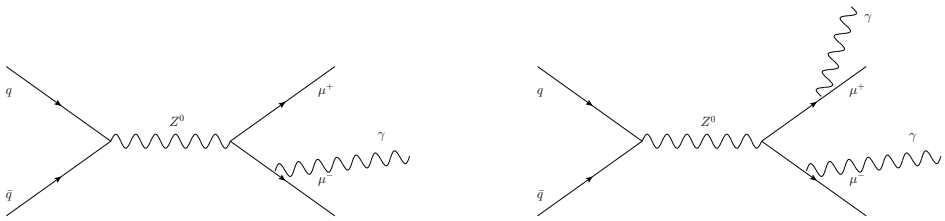

(a) Single photon emission - $Z \to \mu\mu\gamma$.

(b) Double photon emission - $Z \to \mu\mu\gamma\gamma$.

Figure 4.2: Radiative processes included in PHOTOS. One photon is radiated (a) and two (b).

4.3.1 Generator level

The generator level events can be analysed simultaneously and therefore the events can be compared. The momentum of the daughter muons, and hence the reconstructed Z mass are recorded before and after radiation. Figure 4.3 shows the dimuon invariant mass distribution of events at generator level. The FSR radiation causes events from the centre of the invariant mass distribution to shift to lower masses into the radiative tail. This effect is illustrated in table 4.2 which shows the difference in the mean and width of each distribution.

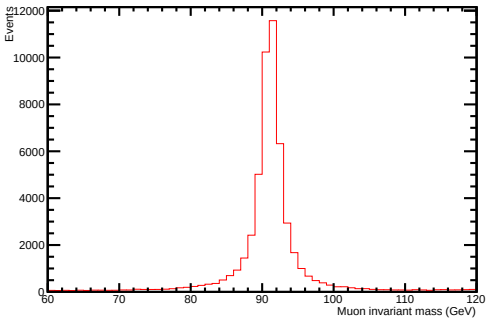

(a) Invariant mass with no FSR.

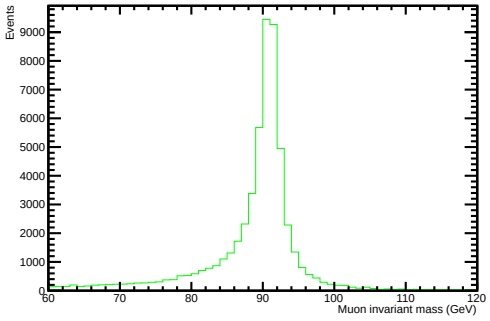

(b) Invariant mass with FSR included.

Figure 4.3: The muon invariant mass at generator level, (a) without FSR included and (b) with FSR included.

	Mean (GeV)	**Width (GeV)**
$Z \to \mu\mu\gamma$	88.8	6.9
$Z \to \mu\mu$	91.1	6.0

Table 4.2: The width and mean of the distributions shown in figures 4.3(a) and (b). The additional radiated photon has been modelled in the $Z \to \mu\mu\gamma$ sample. No photon radiation is modelled in the $Z \to \mu\mu$ sample.

The differing shapes are further illustrated by figures 4.4(a) and (b). The figure in (a) shows the dimuon invariant mass distribution. The red simulated data is Z events generated with no FSR modelling. The green simulated data shows Z events generated with FSR modelled. This demonstrates the slight shift in the Z mass peak. In figure (b) the difference between the two is also shown. This highlights the excess in the low energy tail.

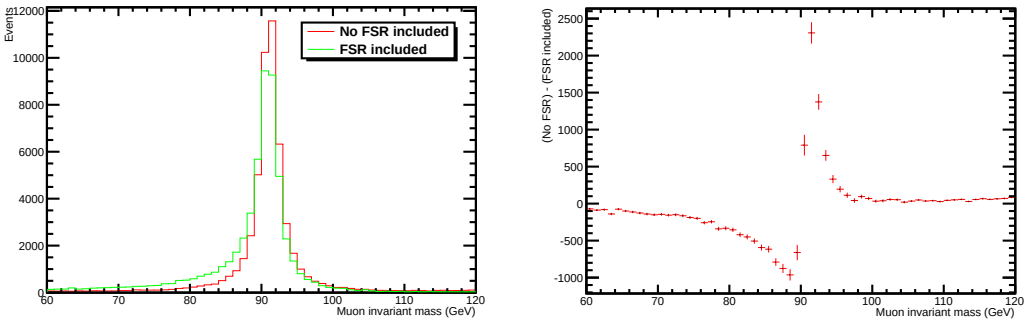

(a) Invariant mass distributions overlaid.

(b) Difference between FSR and no FSR.

Figure 4.4: (a) Invariant mass distribution at generator level, where FSR has (has not) been included in green (red). (b) The difference between the distributions shown in part (a), FSR not included - FSR included.

4.3.2 Full detector simulation level

The full detector simulation includes the generator phase and models the detector response as the particles pass through the detector (described in chapter 3). The simulation study presented here illustrates the difference between adding the photon momentum to the muon pair invariant mass and just using the two muons.

Figure 4.5(a) shows the non-reconstructed photon sample in green. There is a large spread in the peak width ($RMS = 8.1$ GeV) and the mean is 83.2 GeV. The red distribution illustrates the shape when the radiated photon momentum is added to the dimuon momentum. Here the width is narrower,

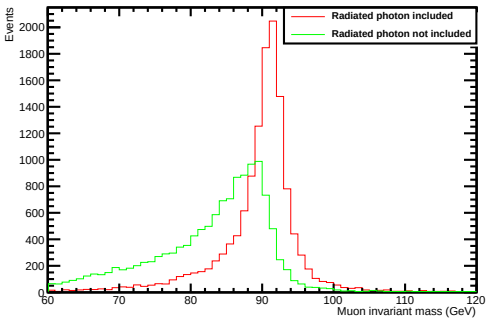

(a) Invariant mass distributions overlaid.

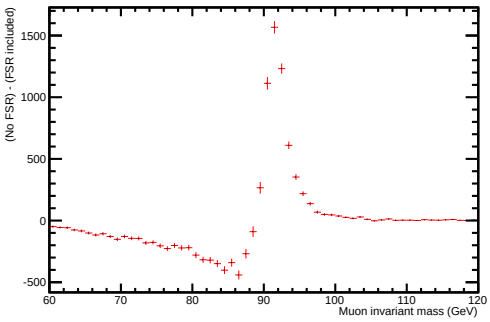

(b) Invariant mass difference between FSR and no FSR.

Figure 4.5: (a) The muon pair invariant mass at full simulation level with FSR (green) and without (red). (b) The difference between the two distributions shown in (a), FSR not included - FSR included.

6.1 GeV, and the mean is 89.5 GeV, which lies closer to the PDG expected value (91.19 GeV). Figure 4.5(b) highlights the low energy tail in the non-reconstructed photon sample with the curve showing a large excess just below the main peak (∼85 GeV).

4.4 Characterising FSR photons

To successfully identify FSR photons in data they must be separated from other sources of background photons. The main background processes to consider are non-associated photons coming from interactions in the beam pipe, which generally have lower P_T. True FSR photons have larger P_T and tend to fly close to the muon they originate from.

4.4.1 Photon P_T

True FSR photons originate from the muons in the decay, and therefore often have more P_T than a background photon. This is shown in figure 4.6. It can be seen that background photons (red) have less P_T than FSR photons (green). FSR photons also show a longer tail to higher P_T.

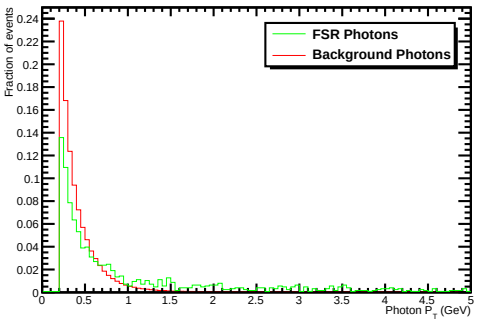

Figure 4.6: The P_T of true FSR photons (green) and background photons (red).

4.4.2 Angle of flight

The angle of flight, θ, between the photon and the muon is defined by:

$$cos\theta = \frac{P_\mu \cdot P_\gamma}{|P_\mu||P_\gamma|}. \tag{4.1}$$

Figure 4.7 shows this angle for FSR (green) and non-FSR (red) photons. In each case the smallest angle between the photon and the two muons is plotted. The distribution for FSR photons peaks at a low angle whereas the background photons have a distribution that extends to higher values. This is due to the random nature of their association with the muon.

4.4.3 Cone distance

The cone distance, $R_{\eta\phi}$, is similar to the angle defined above. It is the distance between the photon and muon, but is defined as:

$$R_{\eta\phi} = \sqrt{(\eta_\mu - \eta_\gamma)^2 + (\phi_\mu - \phi_\gamma)^2}. \tag{4.2}$$

Figure 4.8 shows the cone distance for FSR (green) and non-FSR (red) photons. There is a similar distribution to the angle of flight discussed before, but the background photons show a much broader spectrum than for the

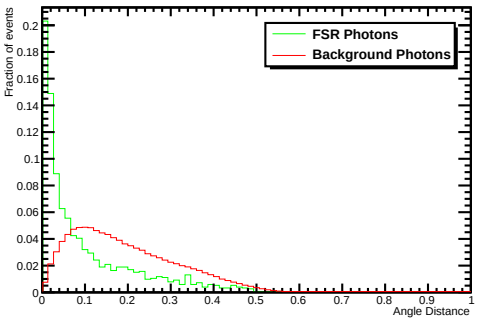

Figure 4.7: The angle in radians between FSR (non-FSR) photons and the closest muon in green (red).

angle of flight.

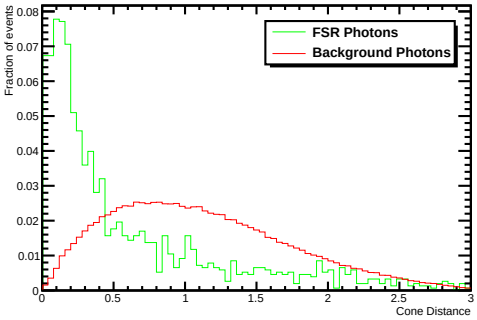

Figure 4.8: The cone distance between FSR (non-FSR) photons and the closest muon in green (red).

4.4.4 `isPhoton`

`isPhoton` is a multivariant analysis tool used to separate π^0 from photons. It takes into account the cluster size and shape of the cluster to decide whether it is a good photon candidate. Figure 4.9 illustrates the difference between true FSR photons on green and background cluster in red.

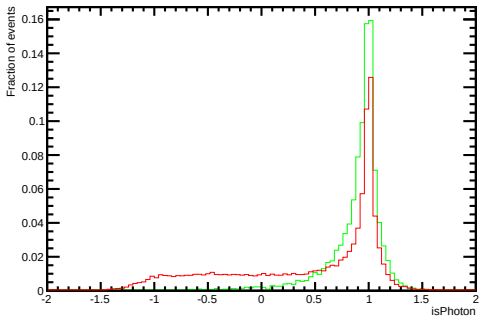

Figure 4.9: `isPhoton` distribution for true FSR photons (non-FSR background) in green (red). Values close to one or above indicate a good photon candidate.

Quantity	Selection
Photon P_T	> 1.5 GeV
Angle of flight	< 0.075
Cone distance	< 0.5
`isPhoton`	> 0.5

Table 4.3: Summary of requirements placed to select FSR photons.

4.4.5 Initial selection

Taking all of the characteristics discussed above, an initial selection is finalised. FSR candidates are selected by requiring P_T above 1.5 GeV. This is a relatively tight requirement, however, the higher energy photons will make the biggest difference to the reconstructed Z mass peak. The angle of flight and cone distance must be < 0.075 and < 0.5 respectively, and finally `isPhoton` > 0.5. These requirements are tabulated in table 4.3.

4.5 Performance

First the selections detailed in chapter 5 are applied to simulated data to select $Z \to \mu\mu$ events. This defines the selected sample. The original simulated data is then also reconstructed as $Z \to \mu\mu\gamma$ and matched to the

selected sample. This results in the same events being reconstructed both with and without an additional photon, and hence comparison between them is possible.

4.5.1 Fitting

The simulation datasets are fitted using a Crystal Ball function added to a Voigtian function from the ROOFIT [60] package, plus a low mass exponential to model the heavy flavour contribution and the $\gamma^* \to \mu\mu$ process (discussed in detail in chapter 5). The Crystal Ball and Voigtian shapes are discussed briefly below.

Crystal Ball shape

A Crystal Ball function is Gaussian in its main shape, with the addition of an exponential tail on the low side. This is used traditionally to model radiative losses. The general function of a Crystal Ball is of the form:

$$\left.\frac{\left(\frac{n}{|\alpha|}\right)^n e^{-\frac{1}{2}\alpha^2}}{\left(\frac{n}{|\alpha|} - |\alpha| - x\right)^n}\right|_{x<-|\alpha|}, \exp\left(-\frac{1}{2}\left(\frac{x-m}{\sigma}\right)^2\right)\Bigg|_{x>-|\alpha|} \tag{4.3}$$

where the first term before the comma is the exponential tail, and the second is a simple Gaussian. n is the exponential slope, α is the direction of the slope. The shape is shown on the right of figure 4.10.

Voigtian shape

A Voigtian function is a convolved Gaussian typically used to model resonances in the presence of finite detector resolution. A Voigtian has the general form:

$$\frac{1}{(x-m)^2 + \frac{1}{4}g^2} \bigotimes \exp\left(-\frac{1}{2}\left(\frac{x}{\sigma}\right)^2\right) \tag{4.4}$$

where m is the mean, g is the width, and the second expression is again a simple Gaussian. The general shape is shown in figure 4.10.

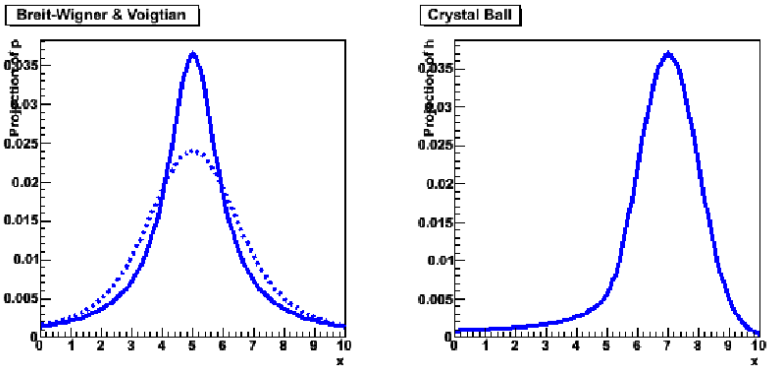

Figure 4.10: The general shape of a Voigtian (left - blue dashed) and Crystal Ball (right - blue) [61].

Quantity		No correction	Correction
Mean		91.047 ± 0.005	91.054 ± 0.005
Width	Voigtian	4.07 ± 0.05	3.76 ± 0.06
	Crystal Ball	1.92 ± 0.01	1.51 ± 0.01

Table 4.4: Summary of results from reconstructing FSR photons in simulation. Both the mean and width are in GeV.

4.5.2 Results

Both simulation samples are fitted with the shapes described above. Figure 4.11(a) shows the simulation with no photon reconstructed, and (b) shows the same sample but with the FSR events corrected. From this fit the reconstructed Z mass is found to increase from 91.047 GeV to 91.054 GeV. However, these are consistent within the fit uncertainty. The width of the distributions are split in two to describe both fitting shapes used. In the sample with no FSR correction the Voigtian width is fitted to be 4.07 GeV, and the Crystal Ball width, 1.92 GeV. This is reduced in the FSR corrected sample, the Voigtian and Crystal Ball are 3.76 GeV and 1.51 GeV respectively. These results are presented in table 4.4.

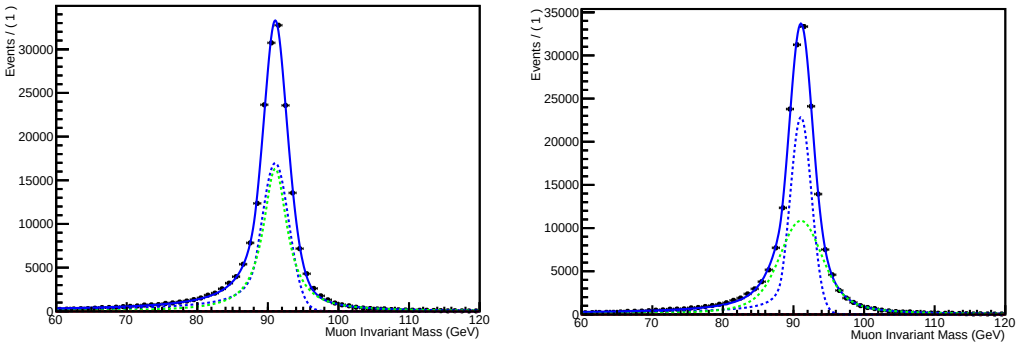

(a) Fitted simulation with no photon reconstruction.

(b) Fitted simulation with photon reconstruction.

Figure 4.11: Simulation fitted with combination of Crystal Ball (green dashed), Voigtian (blue dashed) and exponential (red dashed). Simulation with no photon reconstruction is shown in (a), the same sample but with photon reconstruction is shown in (b).

4.6 Conclusion

Final state radiation has been successfully added into the simulation phase at LHCb. Using an initial selection in simulation has shown a small increase in the reconstructed mass of the Z towards the correct PDG value (91.19 GeV). The resolution of the mass peak narrows, on average, by 0.36 GeV in both shapes. It is possible this result could be improved by reconstructing additional photons when double photon emission occurs. The selection could also be evolved and the possible use of a neural network could be investigated.

Chapter 5

$Z \to \mu\mu$ cross-section measurement

5.1 Introduction

Measuring the production cross-section of Z bosons at the LHC provides a valuable test of the electroweak sector of the Standard Model. In this thesis a measurement is made using $Z \to \mu\mu$ events in the muon pseudorapidity range between $2.0 \leq \eta_\mu \leq 4.5$ and muon $P_T > 20$ GeV. This provides a unique measurement in the forward region, some of which is complementary to ATLAS and CMS, who make measurements in the region $\eta_\mu \leq 2.5$. Measuring the cross-section for $\eta_\mu > 2.5$ is important because the understanding of the underlying proton behaviour is poor compared to other regions. This is shown in chapter 3 figure 2.7 where the percentage theoretical uncertainty on cross-section predictions with respect to the boson rapidity is illustrated. At the low end of the LHCb acceptance the uncertainty is $\sim$1%. Measurements here enable a precise comparison of theory to data, and are therefore a good test of the Standard Model. Towards the high end of the acceptance, the knowledge of the cross-section is less well known ($\sim$3%). This allows any measurement made at LHCb to constrain the underlying PDFs in this region.

Polarity	Amount
Magnet Up	439.48 pb^{-1}
Magnet Down	587.89 pb^{-1}
Total	1027.37 pb^{-1}

Table 5.1: The total amount of data used and the distribution between magnet up and magnet down configurations.

Using the dimuon final state, this thesis presents a cross-section measurement of Z production between pseudorapidities of 2 and 4.5. Additionally to this, a differential cross-section measurement as a function of Z boson rapidity, $\frac{d\sigma}{dy}$, between the same range is also presented.

This chapter begins with information on the data and simulation samples used for this analysis in section 5.2. This is followed by a discussion of signal event characteristics in section 5.3 and the event selection in section 5.4. Background contamination, efficiencies and systematic uncertainties are covered in sections 5.5, 5.7 and 5.8, respectively. Finally the results and comparison to theory are presented in section 5.10.

5.2 Datasets used

5.2.1 Data

This analysis is based on approximately 1 fb^{-1} of data collected by LHCb in 2011 at $\sqrt{s} = 7$ TeV. These data were taken with both magnet polarities. A breakdown of how much data was collected with each magnet polarity is shown in table 5.1.

Measuring the absolute luminosity

The luminosity at LHCb is measured by a central group to ensure consistent measurements across all analyses. This is done by combining two methods,

firstly the Van der Meer technique [62], and secondly the beam-gas interaction technique [63].

The Van der Meer scan method provides a direct measurement of the visible cross-section. The colliding beams are moved transversely across one another to determine the beam profile. The beam-gas interaction method uses reconstructed beam-gas interactions near the beam crossing point to determine the beam profile.

The methods mentioned here lead to an uncertainty of 3.5% on the absolute luminosity measurement for this dataset [64].

5.2.2 Simulated event samples

Most of this analysis is data driven, to reduce systematic error effects between real data and simulation. This is because simulation may not model real data correctly. Monte Carlo simulation has been used for background studies of the $Z \to \tau\tau$, $t\bar{t} \to \mu\mu$ and $WW \to \mu\mu$ contributions. It has also been used to provide confidence in the $Z \to \mu\mu$ selections placed on the data.

Where possible, the simulation used for this analysis was generated with MC11[1]. This is to ensure the simulated running conditions are as close to real running as possible. The details of the simulation samples used are shown in table 5.2.

[1]MC11 is the name for simulated data made in 2011. This means the reconstruction used are as close to the data running conditions as possible. For these samples the beam energy = 3.5 TeV, number of interactions per crossing, $\nu = 2$. Reconstruction version 12a and stripping version 17 were used to process the simulation, which is the same as were used on data.

Decay	Number of Events	Luminosity
$Z \to \mu\mu$	1033494	13 fb^{-1}
$Z \to \tau\tau$	1026989	13 fb^{-1}
Inclusive B	1970181	281 pb^{-1}
Inclusive C	959993	0.8 pb^{-1}
$t + \bar{t} \to \mu\mu$	101000	0.6 fb^{-1}
$W + W \to \mu\mu$	8600	26.2 fb^{-1}

Table 5.2: Simulation samples used.

5.3 Signal and background studies

5.3.1 Backgrounds

There are a number of processes which form backgrounds to the dimuon channel. These are heavy flavour decays, $Z \to \tau\tau$, pairs of hadrons misidentified as muons, $t\bar{t} \to \mu\mu$ and lastly $WW \to \mu\mu$. Each is described briefly below.

Heavy flavour

Heavy flavour backgrounds arise from semileptonic decays of beauty (b) and charm (c) hadrons. These events can be distinguished from signal by two main characteristics. Firstly, $b-$ and $c-$hadrons have a finite lifetime, therefore they travel much further than a Z does before decaying. This means the muons will come from a secondary vertex away from where the collision took place. Secondly, because these decays are often semileptonic the muons are produced alongside jets of other particles. This means they tend to be less isolated than muons from a Z event, where very little else is produced. The branching fractions for $B \to X\mu\nu$ and $D \to X\mu\nu$ are $10.95 \pm 0.27\%$ and $12.2 \pm 1.6\%$, respectively [65].

$Z \to \tau\tau$

One background arises from $Z \to \tau\tau$ decays. The Z decays to a pair of τ leptons which then decay into two muons and neutrinos ($Z \to \tau\tau \to \mu\mu\nu_\tau\bar{\nu_\tau}\nu_\mu\bar{\nu_\mu}$), where both muons are within the acceptance of LHCb. The branching fraction for τ production is the same as for the production of muons [21] and the fraction of τ's which decay to muons is 0.174. A dimuon decay will occur in approximately 3% ($= 0.174^2$) of the total $\tau\tau$ events. The invariant mass distribution of muons from $Z \to \tau\tau$ are different to those from $Z \to \mu\mu$. This is due to the unreconstructed neutrinos taking a portion of the energy away. The P_T of the muons is also lower than for signal because they are not produced back-to-back in the Z rest frame. This is shown in figure 5.1.

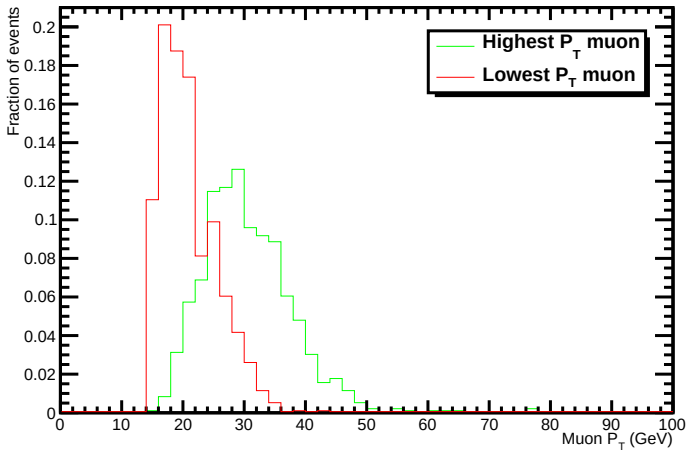

Figure 5.1: The P_T of muons from $Z \to \tau\tau$ production in simulation, where both muons are within the LHCb acceptance ($2 \leq \eta_{\mu\mu} \leq 4.5$). The muon with highest P_T is shown in green, and the lowest in red.

$t + \bar{t} \to \mu\mu$

Double top quark production becomes a background when both tops decay to muons within the LHCb acceptance. An example is shown in figure 5.2(a).

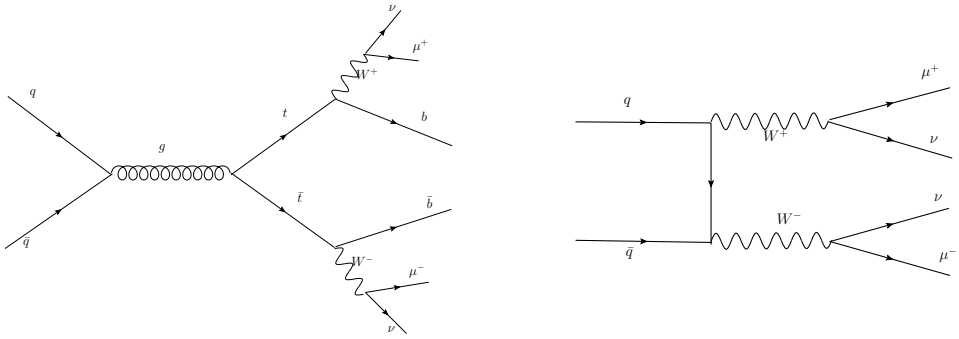

(a) $t\bar{t} \to \mu\mu$

(b) $W + W \to \mu\mu$

Figure 5.2: Feynman diagrams to describe $t\bar{t}$ and WW decay to muons.

The total cross-section for this process is 161 pb. The muon P_T can be used to discriminate this source of background from signal. In signal Z events the muons often have similar transverse momentum to each other ($\sim$45 GeV). However, in top events, both muons peak at around 2 GeV, with one having a small tail to greater P_T's. This is shown in figure 5.3, where the muons are required to lie within LHCb. The muon with highest P_T is shown in green, the muon with the lowest in red.

$W + W \to \mu\mu$

This source of background arises when two W bosons are produced in the event, and both decay to muons within LHCb. An example of how this can proceed is shown in figure 5.2(b). The overall cross-section for this decay is 0.329 pb. Double W production can be differentiated from signal using the dimuon invariant mass. The invariant mass arising from W bosons will not peak at $\sim$91 GeV because they are not produced by the Z resonance. The muon P_T distribution is shown in figure 5.4.

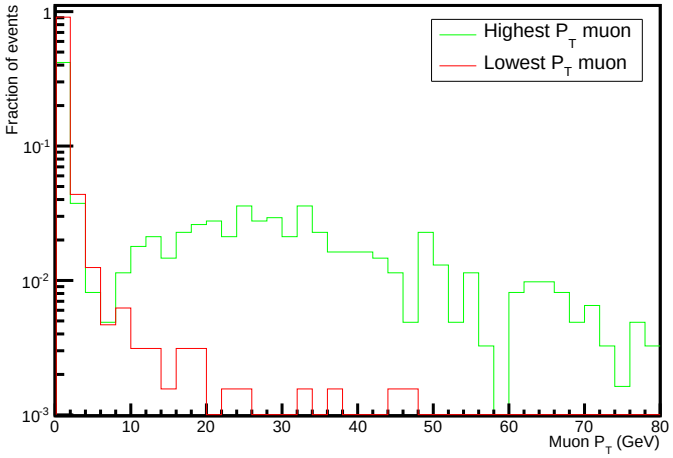

Figure 5.3: The P_T of muons arising from $t\bar{t} \to \mu\mu$ in simulation. Both muons must lie within the LHCb acceptance, $2.0 \leq \eta_{\mu\mu} \leq 4.5$. The muon with highest P_T is in green and the muon with lowest P_T is in red.

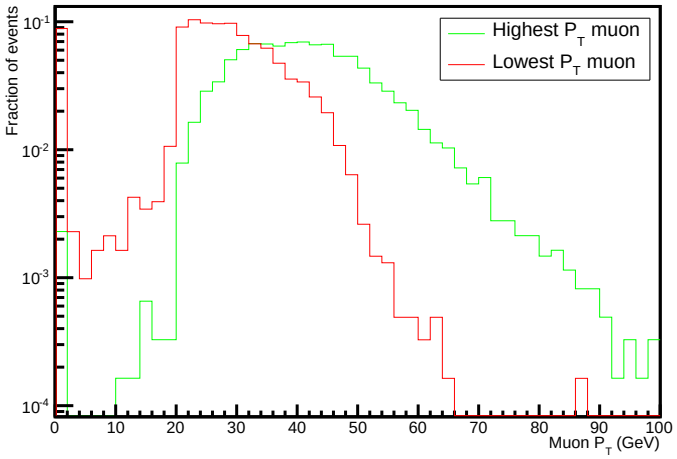

Figure 5.4: The P_T of muons from $WW \to \mu\mu$ simulation. Both muons are within the LHCb acceptance ($2 \leq \eta_{\mu\mu} \leq 4.5$). The highest P_T muon is in green, and the lowest is in red.

Hadron mis-identification

Hadron mis-identification is caused when high momentum pions and kaons are mis-identified as muons. This occurs in two distinct processes; one is punchthrough and the other is decay in flight. Punchthrough occurs when a hadron has enough energy to penetrate the entire detector to the muon stations, and is subsequently identified as a muon. Decay-in-flight occurs when a hadron decays to a muon somewhere before the calorimetry system, and the resulting low deposition mimics a muon signal.

Same-sign contribution

Same-sign contributions arise from processes that can give rise to $\mu^+\mu^-$, $\mu^+\mu^+$ and $\mu^-\mu^-$. An example is the production of $W \to \mu\nu$ and one mis-identified muon, or a semileptonic decay of a heavy flavour hadron with a mis-id muon. As there is no link between the two muons there is no charge correlation as to whether they should be opposite-sign or same-sign. It is possible to estimate the contribution of these sources by checking the rate of same-sign muons in data.

5.3.2 Characteristics of Z signal events

The Z boson has a mass of ~ 91 GeV and a short decay length $\simeq 0.1$ fm. Signal events have a distinct and simple topology. Two high P_T muons of opposite signed charge which have a low impact parameter with respect to the primary vertex are sought. The invariant mass of these two muons should also be close to the PDG mass value of the Z ($\sim$91.19 GeV). A $Z \to \mu\mu$ event is shown in figure 5.5 where two well defined muon tracks with high transverse momentum coming from the primary vertex can be seen.

Next, kinematic variables which can be used to distinguish between signal and background processes are discussed.

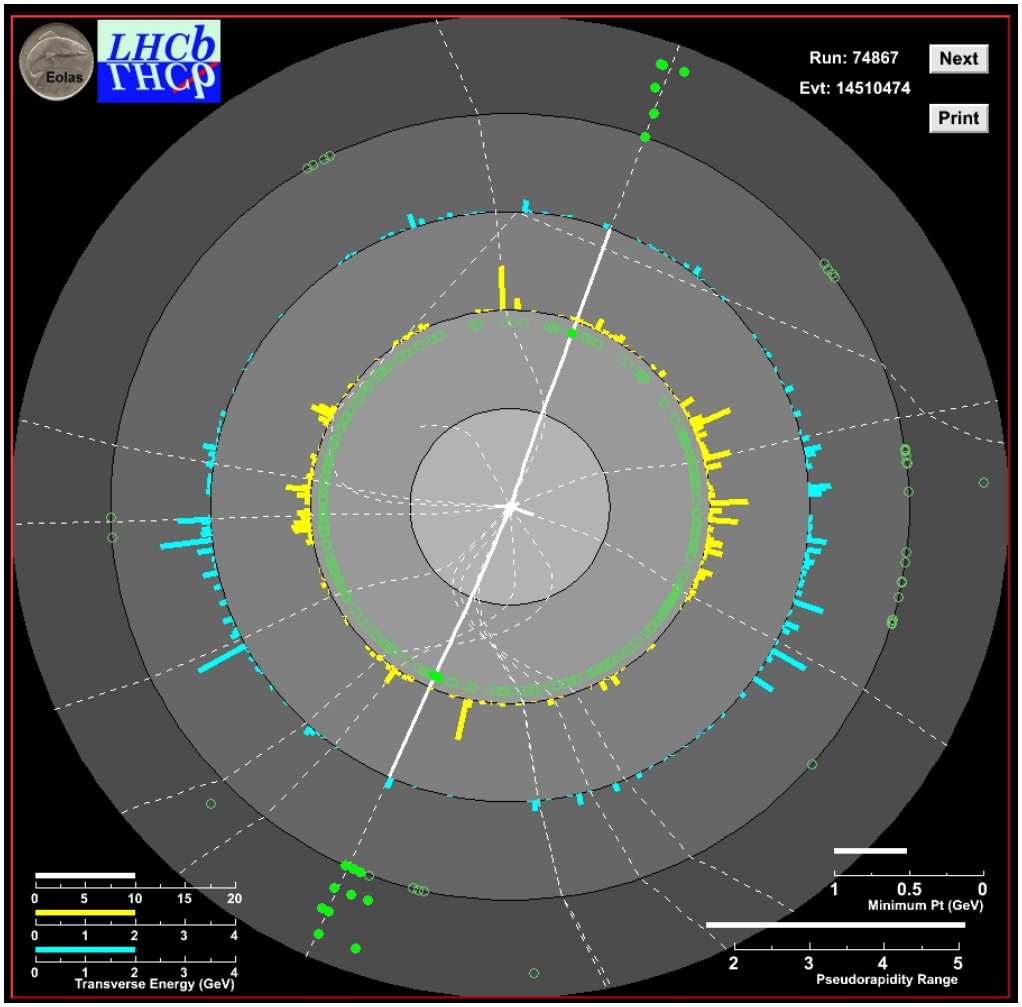

Figure 5.5: $Z \rightarrow \mu\mu$ event using the EOLAS event display. EOLAS is a graphical representation of the LHCb detector in the transmogrified $z - \phi$ projection. The dotted lines represent tracks, solid white lines imposed on the top illustrate the P_T of that track, the yellow (blue) bars represent the energy deposited in the ECAL (HCAL), green empty dots on the outer circle are hits in the muon chambers (M1 closest to the centre, then M2, etc), the filled in green dots represent a muon chamber hit that is associated with a track.

Muon invariant mass

The invariant mass of the daughter muons can be used to calculate the mass, $M_{\mu\mu}$, of the mother Z candidate. This is defined by:

$$\Big(\mathrm{M}_{\mu\mu}\Big)^2 =$$
$$\Big(E^{\mu-} + E^{\mu+}\Big)^2 - \Big((P_x^{\mu-} + P_x^{\mu+})^2 + (P_y^{\mu-} + P_y^{\mu+})^2 + (P_z^{\mu-} + P_z^{\mu+})^2\Big)$$

where, E is the total energy and $P_{x,y,z}$ are momentum components, $\mu^{\pm}$ refers to the positively and negatively charged daughter muons respectively. In signal events the invariant mass is distributed in a peak around the mass of the Z. Background events will typically have lower invariant mass, and no peaking structure is seen, as the muons do not arise from a resonant decay.

Figure 5.6 shows the distributions of dimuon invariant mass for simulated signal, $Z \to \tau\tau$, heavy flavour, $t\bar{t}$ and double-W events. The differences shown here illustrate that the invariant mass cut detailed in section 5.4 is important for reducing background processes.

Muon transverse momentum

The transverse momentum of a particle, P_T, is defined by:

$$P_T = \sqrt{P_x^2 + P_y^2}. \tag{5.1}$$

Muons in $Z \to \mu\mu$ events typically have very high P_T because they originate from the high mass Z. In the rest frame of the Z, the muons are produced back to back, and hence take approximately half of the Z rest mass each. LHCb is able to detect both muons because in the lab frame the Z is also boosted forwards, meaning the muons also fly forward along the Z flight direction.

Figure 5.7 shows signal and background muon transverse momentum. It can be seen that imposing a high P_T requirement is efficient at reducing

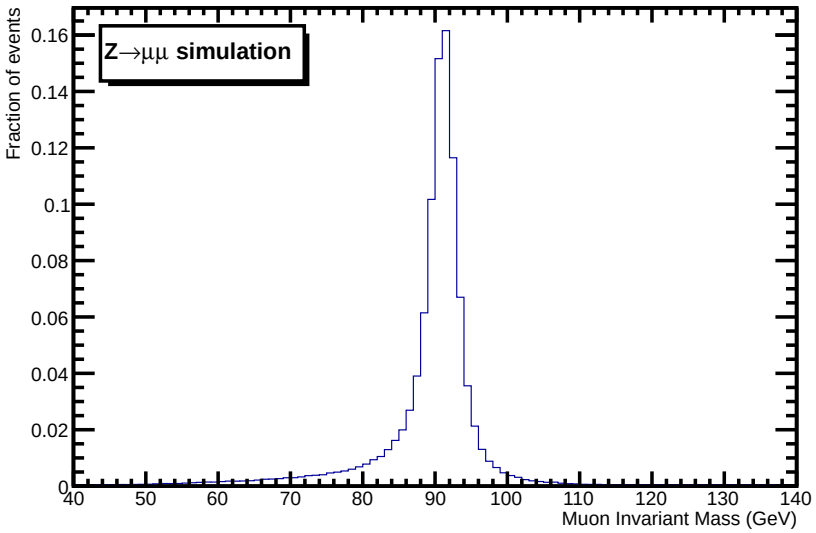

(a) $Z \to \mu\mu$ signal simulation.

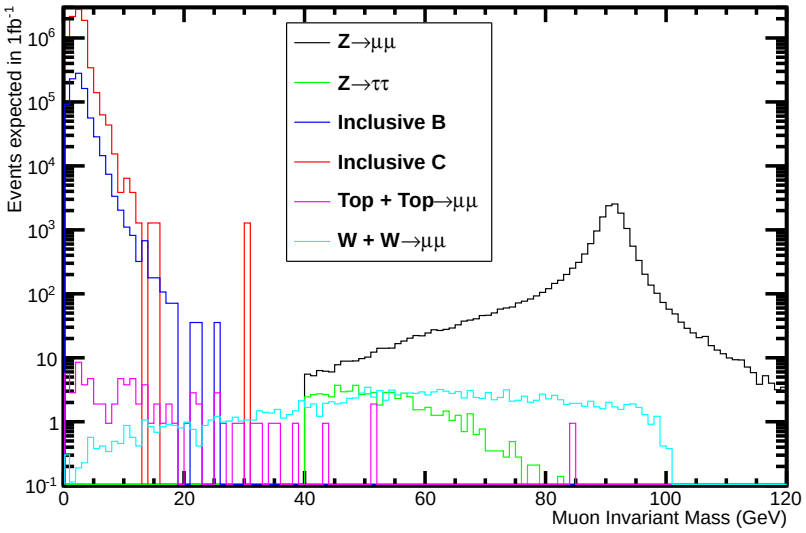

(b) Simulated background processes.

Figure 5.6: (a) Shows the invariant mass distribution expected for signal events, and (b) shows the invariant mass distribution expected for backgrounds in 1 fb^{-1} of data. In all cases the muon $P_T \geq 1$ GeV and must lie within the LHCb acceptance, $2 \leq \eta_{\mu\mu} \leq 4.5$. $Z \to \mu\mu$ and $Z \to \tau\tau$ both have a selection, $M_{\mu\mu} > 40$ GeV in the stripping.

background.

Muon isolation

Muon isolation is an important characteristic to distinguish signal events. Muons originating from a Z tend to be isolated because little else occurs in the event. In background events involving heavy quarks, muons tend to be produced in association with jets of other particles, hence they are less isolated. To evaluate the isolation firstly a cone is drawn around the muon in $\eta - \phi$ of radius:

$$\mathrm{R} = \sqrt{(\delta\eta_{\mu-edge})^2 + (\delta\phi_{\mu-edge})^2}. \tag{5.2}$$

Where $\delta\eta_{\mu-edge}$ is the difference in η between the muon and cone edge, $\eta_\mu - \eta_{edge}$, and $\delta\phi_{\mu-edge}$ is the difference in ϕ between the muon and cone edge, $\phi_\mu - \phi_{edge}$. Here only a cone radius, $R = 0.5$ has been investigated to show the difference in Z events and heavy flavour events (figure 5.8).

5.4 Event selection

Selections placed on events fall into two categories. Firstly, track quality cuts that are applied as a preselection. Secondly, offline selections which are applied to select the fiducial region of the measurement.

5.4.1 Track quality preselection

Track quality cuts are used to ensure that tracks within the event are well reconstructed. "Ghost" tracks are tracks which do not arise form real particles. Formed from a combination of random detector hits joined together to make a track, they must be suppressed. As they are made up of random hits they are generally characterised by a bad track fit quality. By investigating the χ^2 probability and the relative momentum error, $\frac{\sigma P}{P}$ of the tracks, ghosts can be reduced.

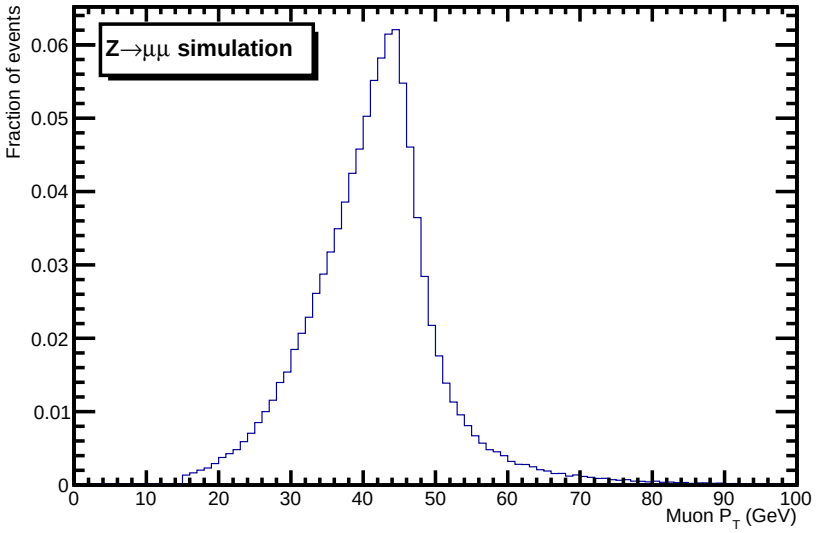

(a) $Z \to \mu\mu$ signal simulation.

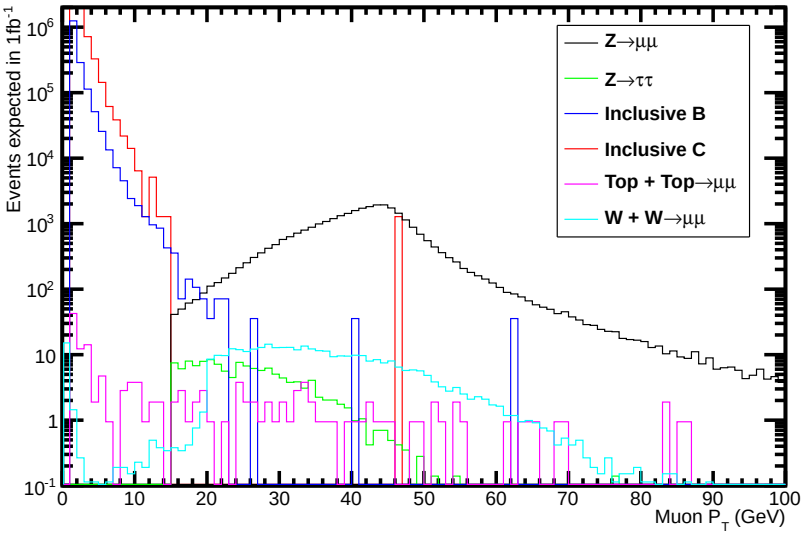

(b) Simulated background processes.

Figure 5.7: (a) Shows the muon P_T distribution expected for signal events, and (b) shows the muon P_T distribution expected for backgrounds in 1 fb^{-1}. In both cases the muons must lie within the LHCb acceptance, $2 \leq \eta_{\mu\mu} \leq 4.5$. $Z \to \mu\mu$ and $Z \to \tau\tau$ have a selection, $P_T > 15$ GeV in the stripping.

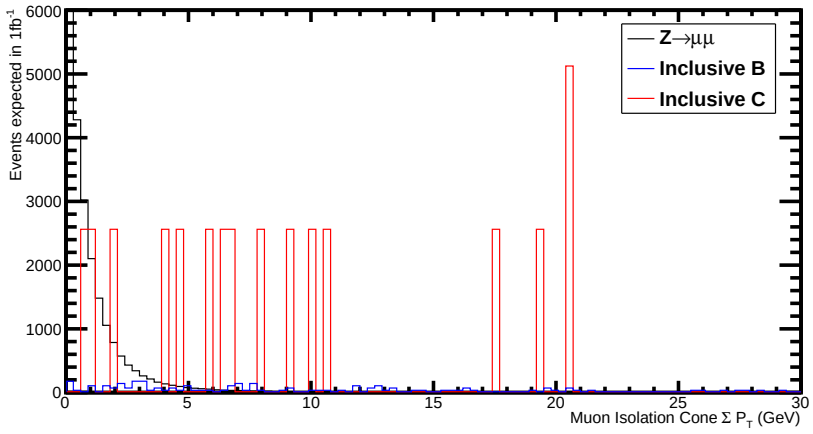

Figure 5.8: Muon isolation, defined as the summed P_T in a cone of 0.5 around the muon for signal and heavy flavour processes. All muons must have $P_T \geq 1$ GeV and lie within the LHCb acceptance, $2 \leq \eta_{\mu\mu} \leq 4.5$.

Figure 5.9 shows the χ^2 probability of long tracks satisfying `isMuon`[2] and having $P_T > 20$ GeV in both simulation and data. A peak is seen at very low probabilities. These low probability tracks are not used because there is a high possibility that they are not well reconstructed. There is a positive gradient in the simulation because the errors on hits are poorly simulated. Tracks must have a χ^2 probability of greater than 0.1%.

Figure 5.10 shows the fractional error on the track momentum where tracks satisfy the same requirements as above for the χ^2 probability. High $\frac{\sigma P}{P}$ is a sign that a track is poorly reconstructed. Figure 5.11 shows simulation flagged as ghosts, these are distributed at higher relative $\frac{\sigma P}{P}$ than those tracks which are not ghosts. A selection of $\frac{\sigma P}{P} < 0.1$ is placed to reduce badly reconstructed ghost tracks.

[2] `isMuon` is a boolean variable used in the discrimination between fake muon candidates and real muons. More information is available in section 5.4.2.

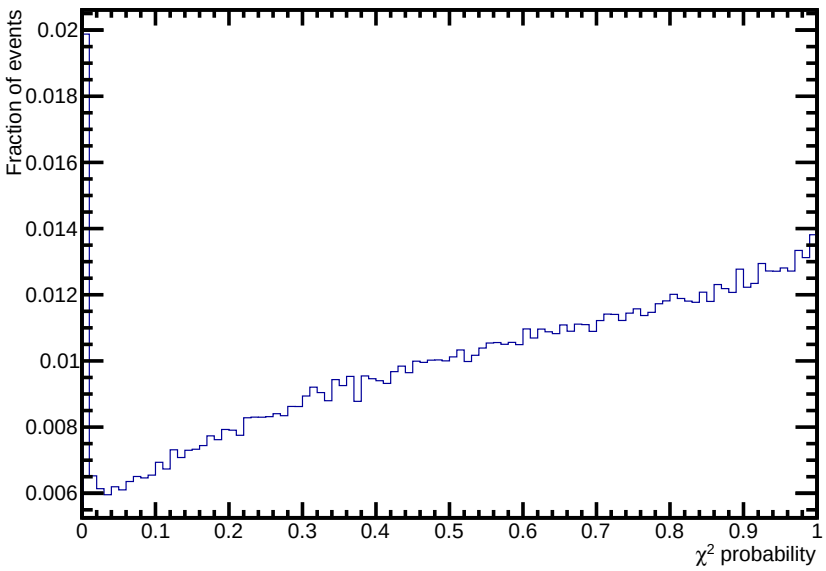

(a) Simulation

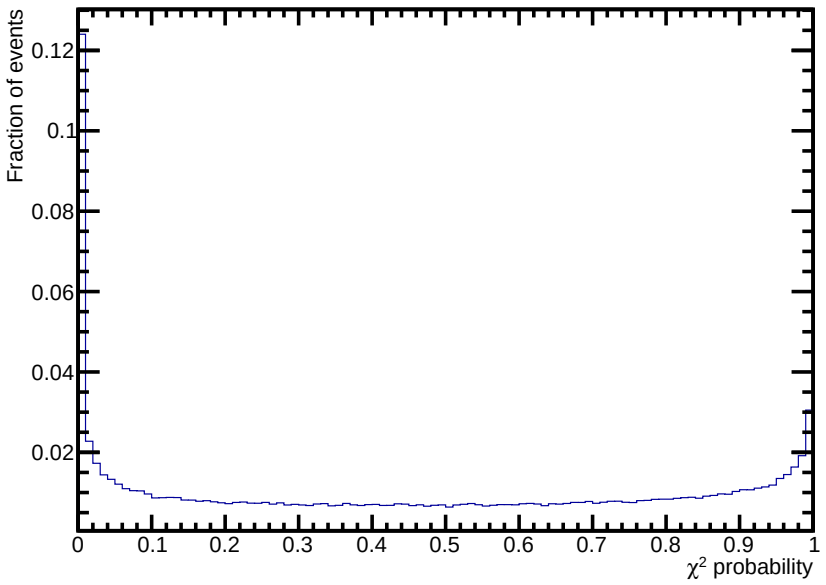

(b) Data

Figure 5.9: χ^2 probability of tracks in (a) simulation and (b) data.

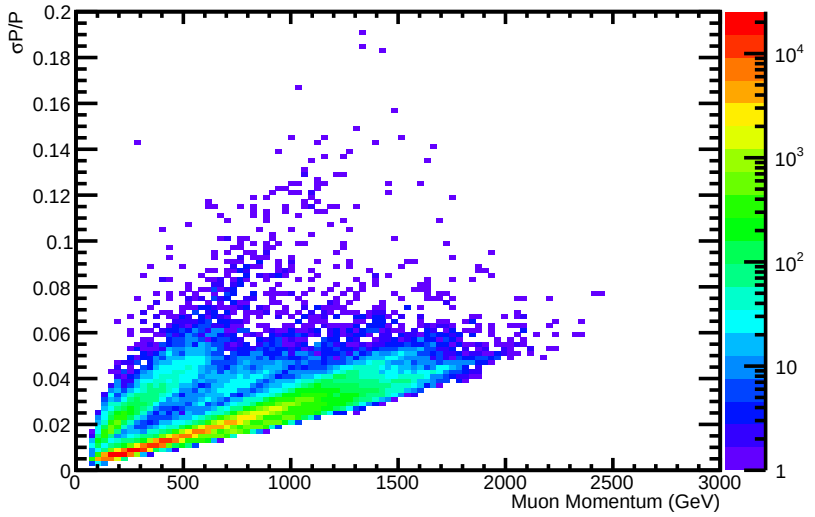

(a) Simulation

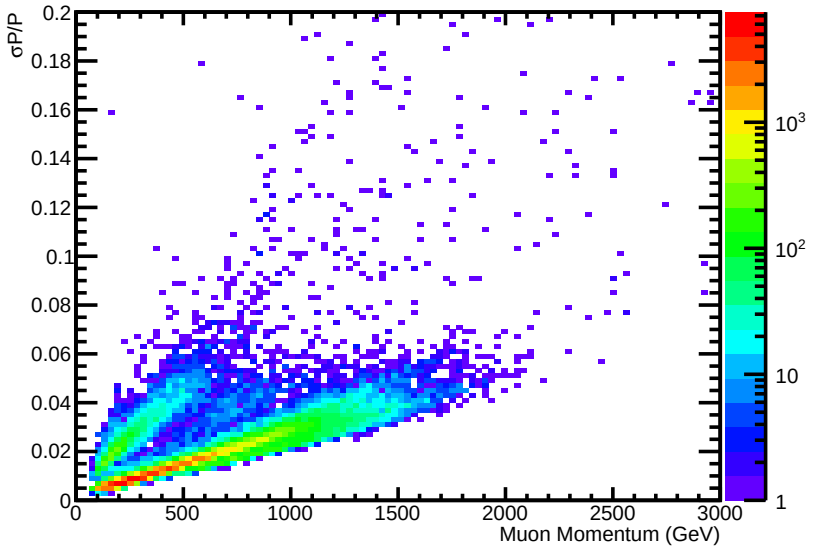

(b) Data

Figure 5.10: $\frac{\sigma P}{P}$ vs momentum of tracks in (a) simulation and (b) data.

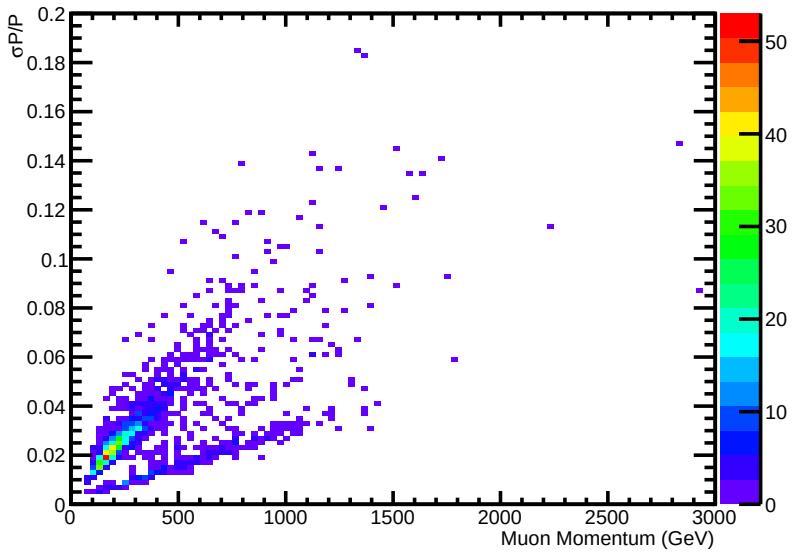

Figure 5.11: $\frac{\sigma P}{P}$ vs momentum of simulated tracks that are flagged as ghosts.

5.4.2 Offline selections

HLT2 trigger selection

Additionally to the kinematic cuts detailed below, there is also a trigger selection. One of the muons must pass a high transverse momentum muon trigger called `Hlt2SingleMuonHighPT`. This requires that there is at least one well identified muon in the event with $P_T > 10$ GeV.

Global event cuts

The need for global event cuts is first discussed in chapter 2. They are placed on every event and are based upon which HLT1 trigger is fired.

There are two distinctly different paths an event may take through HLT1. The first is where one muon of the two from the Z event fires a single muon HLT1 trigger. The second is both muons pass a HLT1 dimuon trigger. If only a single muon triggers the event (the first instance above), it is subject to

	Single Muon	Dimuon
VELO hits	$\leq$ 10000	$\leq$10000
IT hits	$\leq$3000	$\leq$3000
SPD hits	$\leq$600	$\leq$900

Table 5.3: Global event cut selections placed on the single muon HLT1 and the dimuon HLT1.

Momentum range (GeV)	Hits required for positive `isMuon`
$3 < P < 6$	M2 + M3
$6 < P < 10$	M2 + M3 + (M4 or M5)
$P > 10$	M2 + M3 + M4 + M5

Table 5.4: `isMuon` definition with respect to the momentum of the muon candidate.

different global event cuts than if the event is triggered by a dimuon trigger (the second case). These cuts are summarised in table 5.3.

Stripping selection

The $Z \rightarrow \mu\mu$ stripping line reconstructs the entire decay and places tighter selections than are imposed in the trigger. At this point the muons must have $P_T > 15$ GeV and invariant mass, $M_{\mu\mu} > 40$ GeV.

The `isMuon` boolean

At LHCb, muon identification is performed by the `isMuon` algorithm, which returns a boolean yes/no on muon candidates. This decision is based on the momentum of the track, and the number of muon stations which have correlated hits in them. Figure 5.12 shows the probability of a muon reaching each of the muon chambers, as a function of momentum.

The `isMuon` definition varies with momentum, to take into account that a muon with lower momentum has little chance of reaching the outer stations. This variation is tabulated in table 5.4.

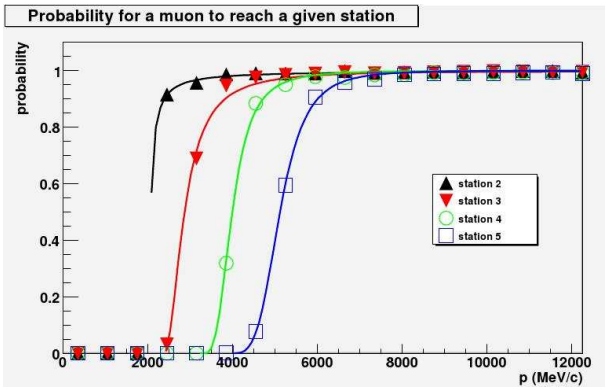

Figure 5.12: The probability of muons reaching a given muon chamber with respect to their momentum [66].

Signal muons must be accepted as a well identified muon by `isMuon`.

Kinematic selections

The kinematic cuts are used to make sure as many signal events as possible are selected, whilst keeping the background levels low. Both muons must have $P_T^\mu > 20$ GeV, and the invariant mass, $60 < M_{\mu\mu} < 120$ GeV. It is also stipulated that both muons must be inside the fully instrumented region of LHCb ($2.0 < \eta_\mu < 4.5$), to reduce detector effects from partially reconstructed tracks. Table 5.5 tabulates all of the selections made on events. Justification for these cuts has been given in section 5.3. These selections also define the fiducial region for the measurement.

5.4.3 Signal yield

The selections described in section 5.4 are now applied to 1.03 ± 0.04 fb^{-1} of proton collision data collected with LHCb in 2011.

There are 56449 $Z \to \mu\mu$ events selected in total. The next section discusses the methods used to estimate how many of these candidates arise from background contamination.

Quantity		Cuts
Track quality	χ^2 Probability	$\geq$0.1%
	$\frac{\sigma P}{P}$	$\leq$ 10%
Kinematic	Track η	$2.0 \leq 4.5$
	`isMuon`	1
	P_T^μ	$\geq$ 20 GeV
	$\text{Mass}_{\mu\mu}$	$60 \rightarrow 120$ GeV
Trigger	`Hlt2SingleMuonHighPT`	Must pass

Table 5.5: Summary of selections used to identify $Z \rightarrow \mu\mu$ events.

5.5 Backgrounds

Each of the backgrounds described in section 5.3 has been analysed to evaluate the level of contamination in the signal region.

5.5.1 $Z \rightarrow \tau\tau$

For the $Z \rightarrow \tau\tau$ contribution, events are generated with PYTHIA 6.4 [50], with a LO PDF set CTEQ6LL [67] and passed through the detector simulation (details in table 5.2). From the full simulated sample of about 13 fb^{-1}, 182 events pass the signal selections. The distribution of events as a function of muon invariant mass is shown in figure 5.13, where a peak is seen at lower invariant mass values than for $Z \rightarrow \mu\mu$. Once the luminosity is taken into account the total events estimated to arise from $Z \rightarrow \tau\tau$ is:

$$Z \rightarrow \tau\tau \text{ events} = 14 \pm 1. \tag{5.3}$$

5.5.2 $t\bar{t} \rightarrow \mu\mu$

For the $t\bar{t} \rightarrow \mu\mu$ contribution, events are generated with PYTHIA 6.4, with a LO PDF set, CTEQ6LL and have been passed through the detector simulation. From the full sample of 0.6 fb^{-1}, 3 events pass the signal cuts. The distribution of events as a function of muon invariant mass is shown in figure

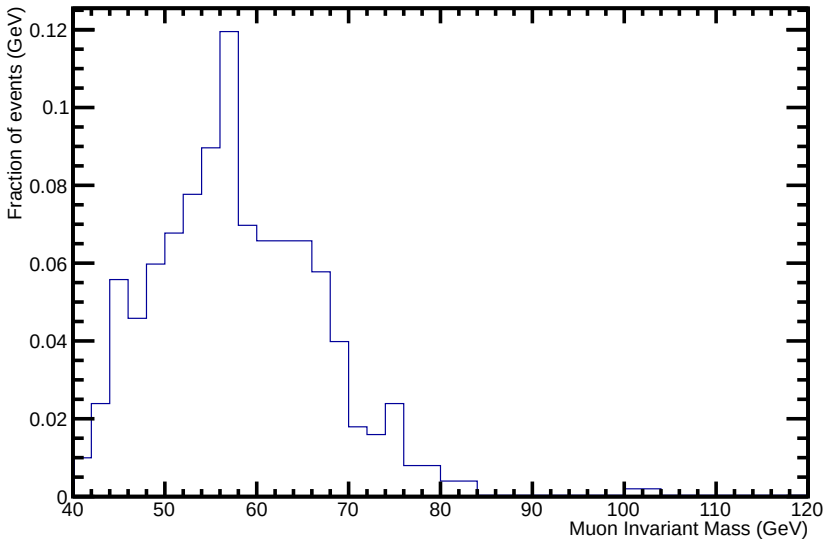

Figure 5.13: Invariant shape mass of dimuons in simulated $Z \to \tau\tau$ decays passing signal selection cuts.

5.14. Once the luminosity is corrected for the LHCb region the total number of events from $t\bar{t} \to \mu\mu$ is estimated to be:

$$t\bar{t} \to \mu\mu \text{ events} = 0.12 \pm 0.11. \tag{5.4}$$

5.5.3 $WW \to \mu\mu$

For the $WW \to \mu\mu$ contribution, events are generated with PYTHIA 6.4, with a LO PDF set, CTEQ6LL with full detector simulation. From the full sample of about 26 fb^{-1}, 2278 events pass the signal cuts. The distribution of events as a function of muon invariant mass is shown in figure 5.15. With the luminosity taken into account the total number of events arising from $WW \to \mu\mu$ is estimated to be:

$$WW \to \mu\mu \text{ events} = 4.1 \pm 0.1. \tag{5.5}$$

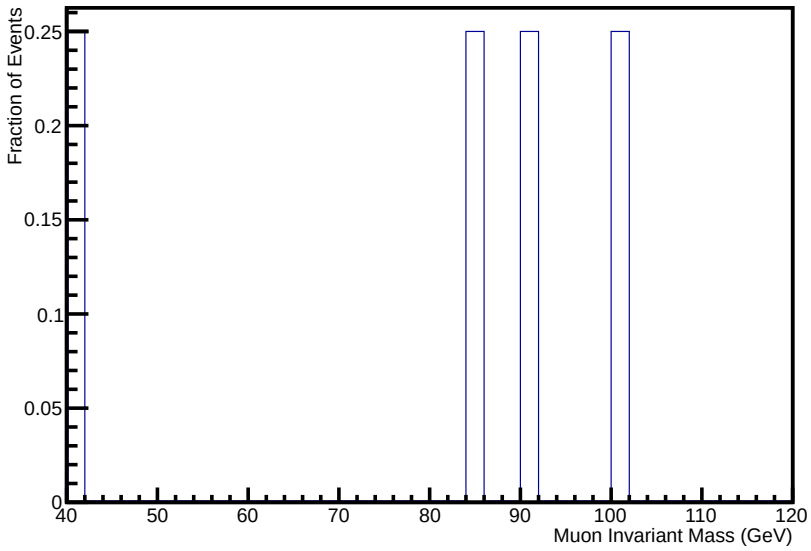

Figure 5.14: Invariant mass shape of dimuons in simulated $t\bar{t} \to \mu\mu$ decays passing signal selection cuts.

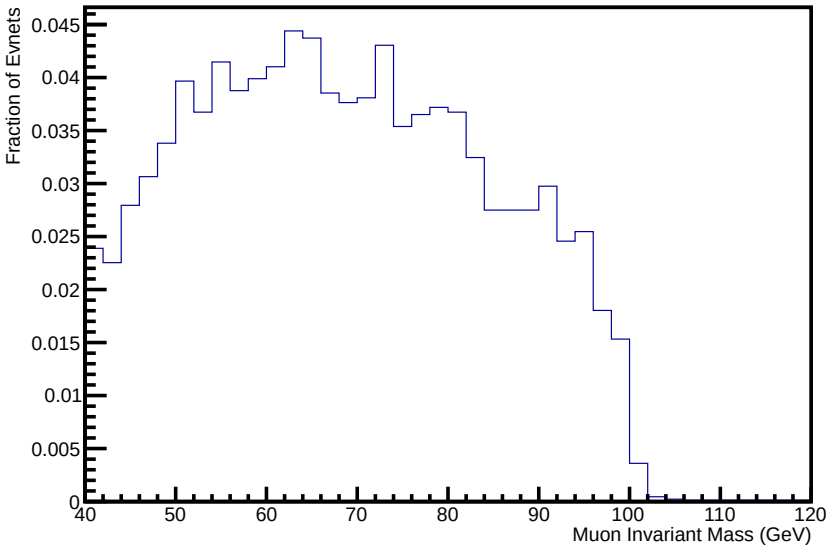

Figure 5.15: Invariant mass shape of dimuons in simulated $WW \to \mu\mu$ decays passing signal selection cuts.

5.5.4 Heavy flavour quarks

The heavy flavour contamination can't be estimated solely with simulation due to limited sample sizes. Figures 5.6 and 5.7 show that there is a difficulty in simulating events with high enough P_T or invariant mass to mimic a Z event. Therefore, this study must be done using data.

The muons from heavy quark decays are usually non-isolated (e.g. in a jet), whereas signal events are more isolated (see section 5.3). Figure 5.16 shows the mass distribution of simulated Z events versus the summed transverse momentum in a cone around the muon as described in section 5.3. The signal region, around a mass of 91 GeV, shows signal muons are mostly isolated, with little momentum found in the tracks around them. To estimate the heavy flavour contribution to the signal peak, events are selected by anti-cutting on muon isolation. This is done by taking muons with reasonably high summed transverse momentum around them, cone[3] $\Sigma P_T > 4$ GeV, and an invariant mass, $M_{\mu\mu} < 60$ GeV. This distribution is fitted with an exponential, which is then extrapolated into the higher mass regime to give an estimate of the overall heavy flavour contamination. Figure 5.17 shows the fitted exponential over the whole mass range. The number of events estimated by this as being heavy flavour is:

$$\text{Heavy flavour events before correction} = 159.8 \pm 3.4. \tag{5.6}$$

A correction is needed to account for the number of heavy flavour events lost by imposing the cut on isolation. This is calculated with the inclusive B and C simulation. Both muons must have $P_T > 1$ GeV and the invariant mass, $\mathrm{M}_{\mu\mu} > 60$ GeV. The correction factor is determined by the fraction of these events which fail the isolation cut (cone $\Sigma P_T > 4$ GeV) compared to those which pass. This is found to be 0.77. Using this and the above events passing the anti-cut, the total amount of heavy flavour events contributing to the Z peak is estimated to be:

[3]The cone around the muon is defined in section 5.3.

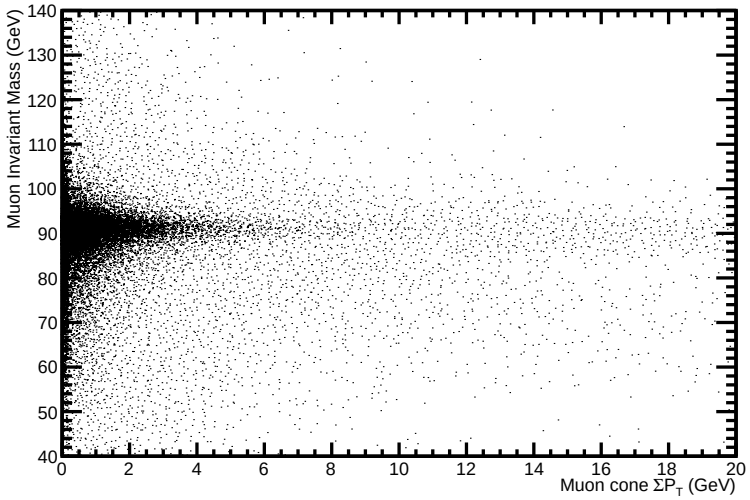

Figure 5.16: Summed transverse momentum, ΣP_T, around the muon vs the invariant mass of the muon pair. $Z \to \mu\mu$ events in data selected without an invariant mass constraint.

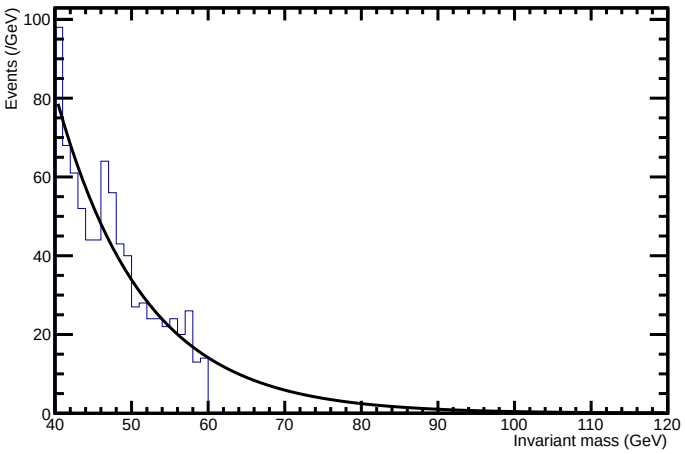

Figure 5.17: Invariant mass of heavy flavour events estimated in data by anti-cutting on the muon isolation (blue). The distribution is fitted by an exponential extrapolated into the Z signal region (black).

$$\text{Total heavy flavour events} = 207.5 \pm 4.4. \tag{5.7}$$

5.5.5 Hadron mis-identification

As described in section 5.3, hadron mis-id both punchthrough and decay-in-flight must be taken into account. The two contributions can be modelled with a parameterisation, which depends on the momentum of the muon candidate [68].

Mis-id through the decay-in-flight mechanism occurs when a pion or kaon is produced at the primary vertex, and subsequently decays to a muon. The processes $K \to \mu\nu$ and $\pi \to \mu\nu$, have branching fractions of 63.55% and 99.98% respectively. The probabilities of a Kaon (P(K)) or Pion (P(π)) decaying to muons within LHCb is expected to be of the form:

$$\begin{aligned} P(K) &= 1 - e^{\frac{-1.994}{P_K}} \\ P(\pi) &= 1 - e^{\frac{-0.268}{P_\pi}} \end{aligned} \tag{5.8}$$

where, P_K, P_π is the particle momentum in each case.

Punchthrough occurs when the hadron has enough energy to traverse the entire detector to the muon chambers, and hence be identified as a muon. This can also be parameterised as a function of the muon candidate momentum ($P_{K/\pi}$) as [69]:

$$\text{Probability} = 0.00063 + 3.6 \times 10^{-5} P_{K/\pi}. \tag{5.9}$$

Using the above parameterisations from equations 5.8 and 5.9, the mis-id contamination can be found directly from data.

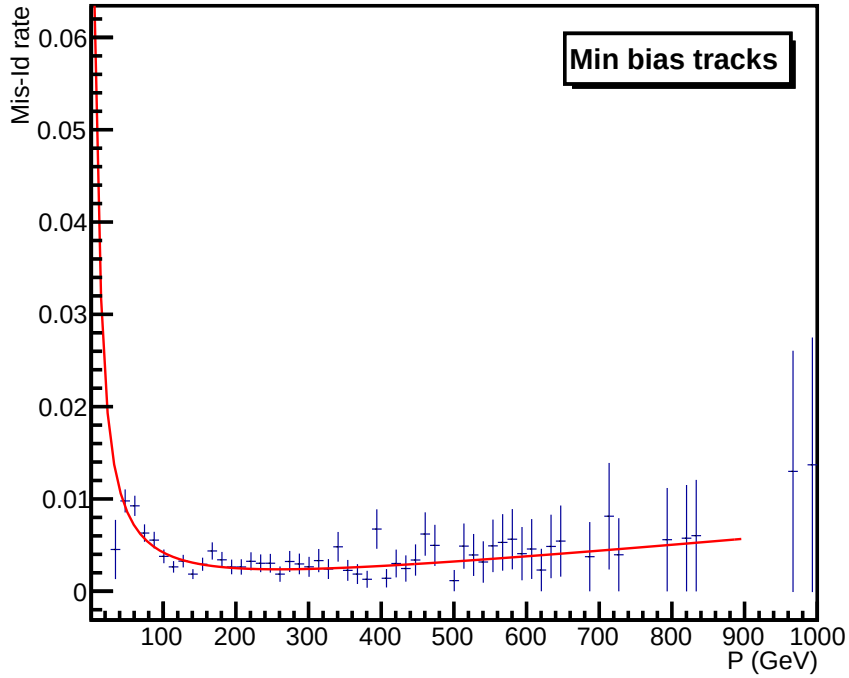

Figure 5.18: Rate of non-muon tracks satisfying `isMuon` vs the momentum of the track (blue points). The distribution is fitted with the function detailed in equation 5.10 (red line). The results are tabulated in table 5.6.

Parameter	Result
$\chi^2/NDOF$	46.95/49
a	0.49
b	7.3×10^{-6}
c	-0.0014

Table 5.6: Values of parameters determined using a fit parameterisation from equation 5.10 to fit the data shown in fig. 5.18. Each fit parameter (a,b and c) corresponds to the label given in the equation.

Mis-identified muons are found by using a data sample of randomly triggered events. It is assumed that this dataset does not contain true muons. Therefore any candidate which satisfies `isMuon` is considered misidentified. Figure 5.18 shows the rate of mis-id versus the hadron momentum. It is fitted with a function:

$$\text{Rate} = (1 - e^{\frac{-a}{P}}) + (b \cdot P + c) \tag{5.10}$$

to represent each of the contributions described above. The fit parameters are shown in table 5.6. This gives a rate:

$$\text{Rate} = (1 - e^{\frac{-0.49}{P}}) + (7.3 \times 10^{-6} \cdot P - 0.0014). \tag{5.11}$$

By finding the average of this function, the overall mis-id rate can be found. For a hadron with momentum in the range between 0 and 900 GeV the mis-id rate is 0.0062 ± 0.0025. This corresponds to an estimated number of mis-id events of:

$$\text{Number of mis} - \text{id events } = 2.2 \pm 1.3. \tag{5.12}$$

5.5.6 Same-sign contribution

The background contribution arising from muons of the same sign is evaluated using data. The same selections are placed on the same-sign data

sample as are placed on the opposite sign data sample. The result of the selections is shown in figure 5.19, and no evidence of a peak at the Z mass is seen. The same-sign contribution is estimated to be:

$$\text{Same} - \text{sign events} = 27 \pm 5.2. \tag{5.13}$$

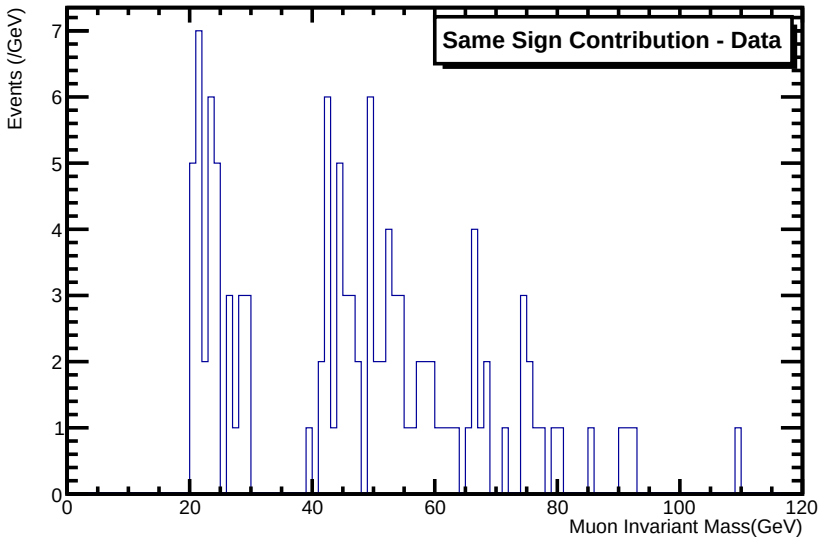

Figure 5.19: Invariant mass distribution in data of same sign muons which satisfy all of the signal event cuts detailed in section 5.4 and table 5.5.

The same sign sample accounts for contributions which arise from many different sources. The main sources for consideration are: hadron mis-identification; semileptonic b or c decays with one mis-identified muon; a W decay with one mis-identified muon; a top decay with a mis-identified muon. The contribution from hadron mis-identification is estimated in section 5.5.5. The other instances where one muon is real and one is fake is estimated by this same sign analysis.

Each of the background contributions has been summarised in table 5.7. The total number of background events is estimated to be 254.9 $\pm$ 7.0.

Background	Events
$Z \to \tau\tau$	14.0 ± 1.0
$t\bar{t} \to \mu\mu$	0.12 ± 0.11
$WW \to \mu\mu$	4.1 ± 0.1
Heavy flavour	207.5 ± 4.4
Mis-id	2.2 ± 1.3
Same-sign	27 ± 5.2
Total	254.9 ± 7.0

Table 5.7: Number of events which arise from each source of considered background.

5.6 Measuring σ_Z

Experimentally, the cross-section, σ_Z is given by:

$$\sigma_Z \times Br(Z \to \mu\mu) = \frac{N^{obs} - N^{bkg}}{\epsilon^{total} \times \int \mathcal{L} dt}. \tag{5.14}$$

Here, Br is the branching fraction of the dimuon decay. N^{obs} and N^{bkg} are the observed number of $Z \to \mu\mu$ candidates and the estimated number of background events respectively. ϵ^{total} is the overall efficiency for recording $Z \to \mu\mu$ events and $\int \mathcal{L} dt$ is the integrated luminosity of the dataset used. The total efficiency can be expressed as the product of the individual parts taken into account:

$$\epsilon^{total} = A^{geom} \times \epsilon^{trig} \times \epsilon^{track} \times \epsilon^{ID} \times \epsilon^{FSR}. \tag{5.15}$$

Where A^{geom} is the acceptance due to the detectable region, ϵ^{trig}, ϵ^{track} and ϵ^{ID} are the overall trigger, reconstruction and muon identification efficiencies respectively. The ϵ^{FSR} is the efficiency due to not reconstructing final state radiated photons. It is used to correct the measurement to Born level in QED so that it can be directly compared to generator level predictions.

5.7 Efficiencies

As stated in section 5.6, the efficiency for the cross section measurement is found by calculating the product of the individual efficiencies. The details of the individual efficiency measurements are discussed in the following subsections. Firstly the tag and probe technique is discussed in section 5.7.1. Next each efficiency is detailed in order, the muon identification efficiency in 5.7.2 and the trigger efficiency in 5.7.3. The efficiency due to final state radiation in 5.7.4. The muon tracking efficiency in 5.7.5 and finally the acceptance in 5.7.6.

5.7.1 Tag and probe technique

The tag and probe technique for measuring efficiency is a data driven method used for resonant decays with two-body final states. Firstly, very tight requirements are made on the reconstruction of one muon (the "tag"). The other muon candidate (the "probe"), has looser requirements applied. Depending on the efficiency being measured, different reconstruction criteria are applied to the probe.

In this regime the efficiencies can be calculated by determining the fraction of probes passing a selection.

5.7.2 Muon identification efficiency

It is important to measure the identification efficiency for Z muons independently so that the measurement made is appropriate for the P_T and η range used in this analysis.

Following the method set out in 5.7.1, the tags are required to pass all of the track quality cuts set out in section 5.4, and pass the muon identification (isMuon). The probe muon must pass the track quality cuts, and form with the tag an invariant mass of $86 \leq M_{\mu\mu} \leq 96$ GeV. With these cuts it is

Quantity		Cuts
Tag	χ^2 Probability	$\geq$0.1%
	$\frac{\sigma P}{P}$	$\leq$10%
	Track η	$2.0 \leq 4.5$
	`isMuon`	1
	P_T^{TAG}	$\geq$ 20 GeV
Probe	χ^2 Probability	$\geq$0.1%
	$\frac{\sigma P}{P}$	$\leq$10%
	Track η	$2.0 \leq 4.5$
	P_T^{PROBE}	$\geq$ 20 GeV
	$\text{Mass}_{TAG,PROBE}$	$Z^0_{Mass} \leq 5$ GeV

Table 5.8: All requirements placed on tag and probe tracks to find the muon ID efficiency.

assumed that everything selected will be a true $Z \to \mu\mu$ event. This is justified in figure 5.20 where the tag is identified as a positive (a) or negative (b) muon. There is little difference between these and where both are identified as muons (c). Full details of the selection used are shown in table 5.8.

The tracks are separated into positive and negative charges, allowing for the ID efficiency to be calculated with respect to each charge. Each of these combinations are shown in figure 5.20 versus the invariant mass. From these and the results in table 5.9, no charge bias is seen in the muon identification.

A similar method is also used on simulated MC11 data to measure the identification efficiency in simulation and compare with data. The results are quoted in table 5.9. The efficiency determined from simulation is slightly higher than in data. However, the data measurement is used for the measurement of the cross-section.

In addition to looking at the difference between charge, the identification efficiency is also shown as a function of muon P_T, η, ϕ, Z P_T and number

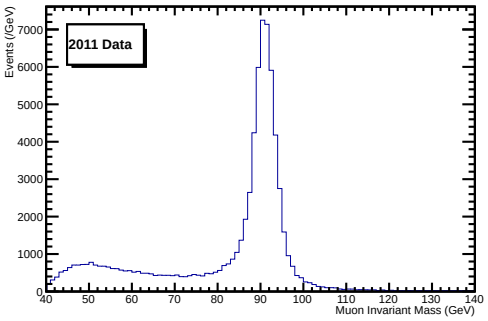

(a) μ^+ as the tag, μ^- as the probe.

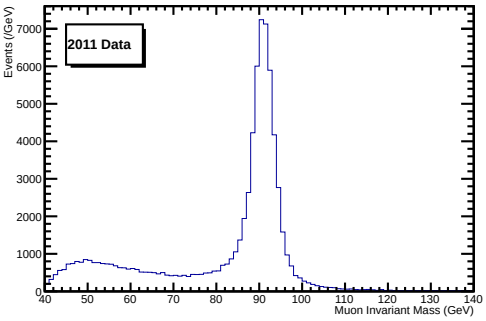

(b) μ^- as the tag, μ^+ as the probe.

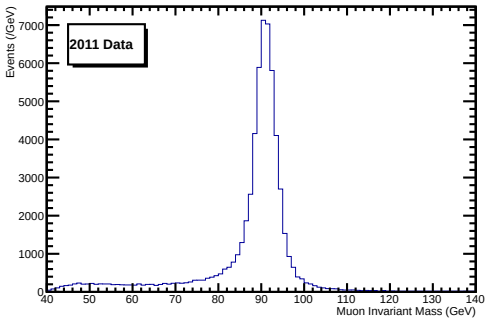

(c) Both μ^+ and μ^- are identified as muons.

Figure 5.20: The muon candidate invariant mass distributions where the positive (negative) muon candidate is the tag in figure a (b). The distributions show a slightly reduced resolution when only the tag is used in comparison to (c) where both muon candidates are identified as muons.

	Data	**Simulation**
μ^+	0.981 ± 0.007	0.989 ± 0.004
μ^-	0.981 ± 0.007	0.989 ± 0.004

Table 5.9: Muon identification efficiency numbers for data and simulation.

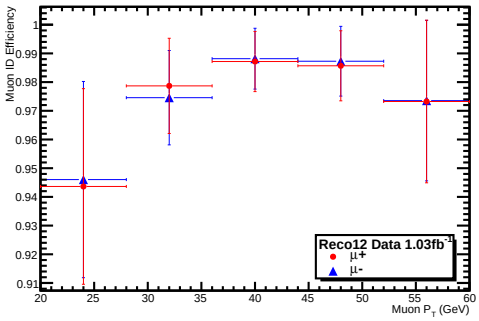

(a) Muon P_T.

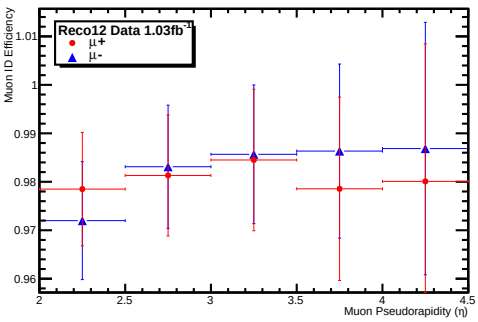

(b) Muon η.

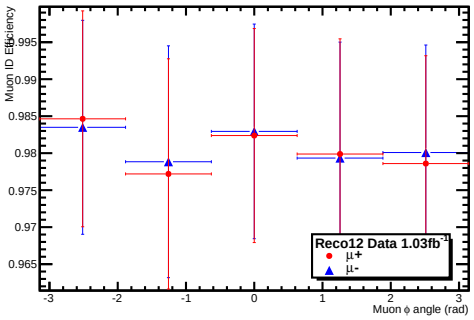

(c) Muon ϕ.

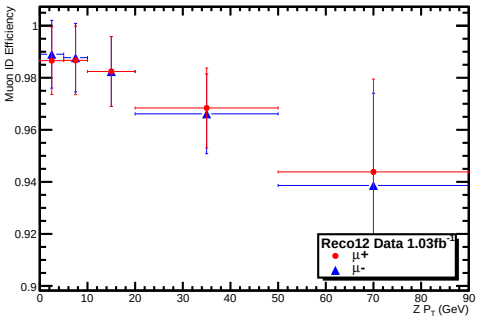

(d) Z P_T.

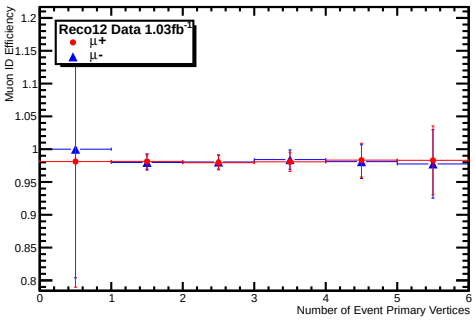

(e) No: of primary vertices.

Figure 5.21: Muon ID efficiency with respect to (a) muon P_T, (b) muon η, (c) muon ϕ, (d) Z P_T, and (e) number of primary vertices. In each case the result for the positive (negative) muon is shown in red (blue).

of primary vertices in figure 5.21 (the same distributions for magnet up and magnet down data and simulation can be found in appendix 7). For a $Z \rightarrow \mu\mu$ event both muons must be identified as a muon. The average identification efficiency is calculated by taking the product of the results quoted in table 5.9, which is:

$$\epsilon^{ID}_{Z\rightarrow\mu\mu} = 0.962 \pm 0.009. \tag{5.16}$$

There is some evidence of dependence on muon P_T and on ZP_T. These are not taken into consideration in the overall or differential measurement with respect to rapidity as there is no net rapidity dependence.

5.7.3 Trigger efficiency

The trigger efficiency can be broken down into two separate parts; the muon trigger efficiency, ϵ^{trig}, and the global event cut efficiency, ϵ^{GEC}. The muon trigger efficiency arises from the HLT2 requirement used in the selections shown in table 5.5. The HLT1 and L0 efficiency are assumed to be 100% because the thresholds are much lower than for the HLT2 trigger. The global event cut efficiency arises from the detector multiplicity selections placed on triggered events.

Muon trigger efficiency

To calculate the muon trigger efficiency the tag-probe method is utilised. The selections on the tag and probe muons are exactly the same as set out in table 5.8, but instead of being identified with `isMuon` the tag muon must pass the HLT2 trigger line, `Hlt2SingleMuonHighPT`. This allows the efficiency to be calculated from the fraction of events in which both the tag and probe pass the trigger and the number in which just the tag does. As for the identification efficiency the muon trigger efficiency has been determined for both data and simulation, and for positive and negative charges as shown separately in table 5.10.

	Data	Simulation
μ^+	0.951 ± 0.007	0.965 ± 0.003
μ^-	0.953 ± 0.007	0.964 ± 0.003

Table 5.10: Muon trigger efficiency numbers for data and simulation.

The efficiency distributions have also been determined as a function of muon P_T, η, ϕ, Z P_T and the number of primary vertices. These distributions are shown in figure 5.22. There is no evidence of a dependence on η, ϕ or number of primary vertices, but a slight dependence is observed against muon P_T and Z P_T. Neither of these are considered in the overall measurement or the differential measurement with respect to rapidity.

The efficiencies for the differently charged muons are combined to find the overall trigger efficiency in the following way:

$$\epsilon^{trig} = \epsilon^{trig}_{\mu+} + \epsilon^{trig}_{\mu-} - \left(\epsilon^{trig}_{\mu+} \times \epsilon^{trig}_{\mu-}\right) \tag{5.17}$$

this takes into account the instances when a trigger fires on a single muon and where it fires on both muons in the event. This gives the overall result for the data sample as:

$$\epsilon^{trig} = 0.998 \pm 0.013. \tag{5.18}$$

Global event cut efficiency

The global event cuts (GECs) are more difficult to analyse as the cuts are applied to the data before offline analysis. Each of the distributions described in section 5.4.2 are investigated. In figures 5.23, 5.24 and 5.25, each is shown with respect to different numbers of primary vertices. The SPD multiplicity has the biggest effect. For this reason only the SPD multiplicity selection is considered in this efficiency analysis.

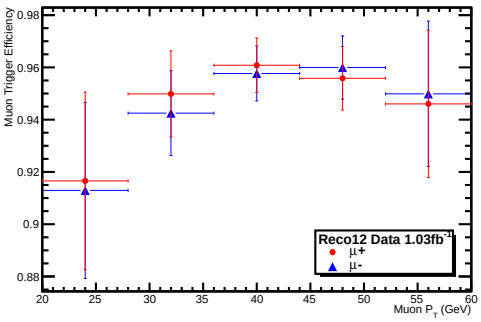

(a) Muon P_T.

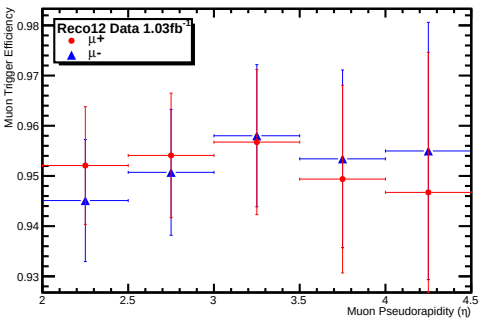

(b) Muon η.

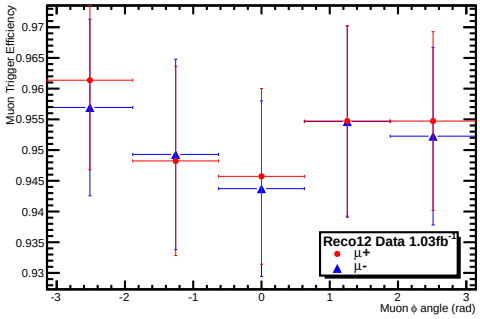

(c) Muon ϕ.

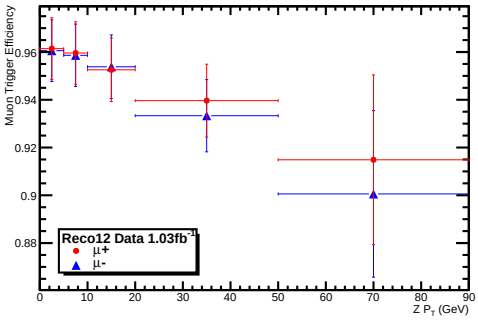

(d) Z P_T.

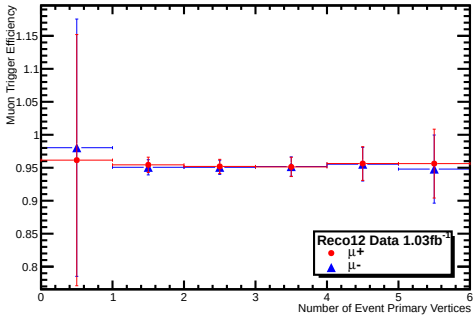

(e) No: of primary vertices.

Figure 5.22: Muon HLT2 trigger efficiency with respect to (a) muon P_T, (b) muon η, (c) muon ϕ, (d) Z P_T, and (e) number of primary vertices. In each case the result for the positive (negative) muon is shown in red (blue).

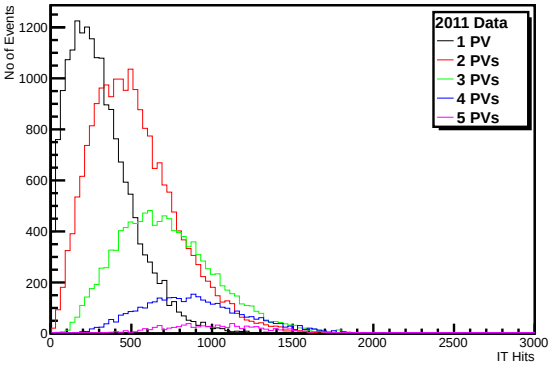

Figure 5.23: Distribution of IT hits in events with at least one primary vertices (1 PV), 2 primary vertices (2 PVs), 3 primary vertices (3 PVs), 4 primary vertices (4 PVs) and lastly 5 or more primary vertices (5 PVs); the selection is at 3000.

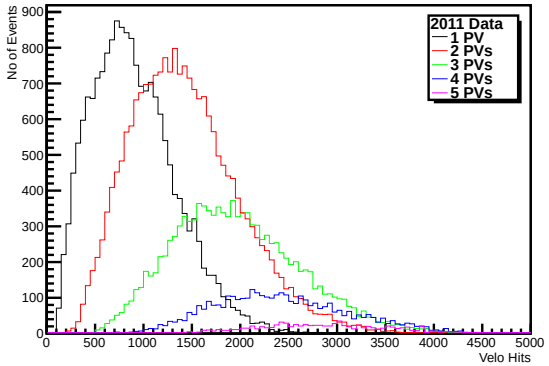

Figure 5.24: Distribution of VELO hits in events with, at least one primary vertices (1 PV), 2 primary vertices (2 PVs), 3 primary vertices (3 PVs), 4 primary vertices (4 PVs) and lastly 5 or more primary vertices (5 PVs); the selection is at 10000.

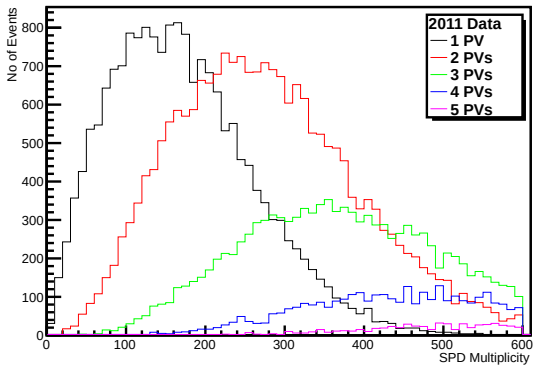

Figure 5.25: Distribution of SPD hits in events with, at least one primary vertices (1 PV), 2 primary vertices (2 PVs), 3 primary vertices (3 PVs), 4 primary vertices (4 PVs) and lastly 5 or more primary vertices (5 PVs); the selection is at 600.

GECs are applied to the event rather than the particles in it so the tag-probe technique can not be used to determine the efficiency. Different SPD selections are placed on the event depending on whether the event has fired a single muon trigger or a dimuon one. Hence, the efficiency is evaluated separately for both cases.

Single muon HLT1 trigger

For the single muon trigger events must have an SPD multiplicity < 600. Figure 5.25 shows that the efficiency of this cut is very dependent on the number of primary vertices (PVs) in the event.

Events with one PV (black) are considered fully measured, as the curve is all below the SPD threshold. To determine the efficiency in data with 2 or more PVs the following method has been used. The data sample with 2 PVs (red) does not lie completely under the threshold, therefore it is not possible to use it to calculate the efficiency. Instead, a sample of 1 PV events is taken, and extra tracks are added to them to increase the SPD multiplicity. The extra tracks come from a calibration stream of events which have no GECs

placed on them and so can be used to increase the SPD multiplicity. This shifts the 1 PV distribution to higher SPD multiplicities to mimic the shape of the 2 PV distribution. In figure 5.26 the 2 PV shapes are shown in the top left. The red curve is the actual data with 2 PVs and the black is the 1 PV data mixed with the extra tracks to simulate the same function.

This same technique is repeated for each sample. For 3 PVs slightly more tracks are added to simulate the higher SPD multiplicity mean, and again for 4 PVs and 5+ PVs. Each of the distributions are shown in figure 5.26. Top right shows 3 PVs, bottom left shows 4 PVs and bottom right shows 5 or more PVs, in each case the black is the data that has been constructed and in red the real data.

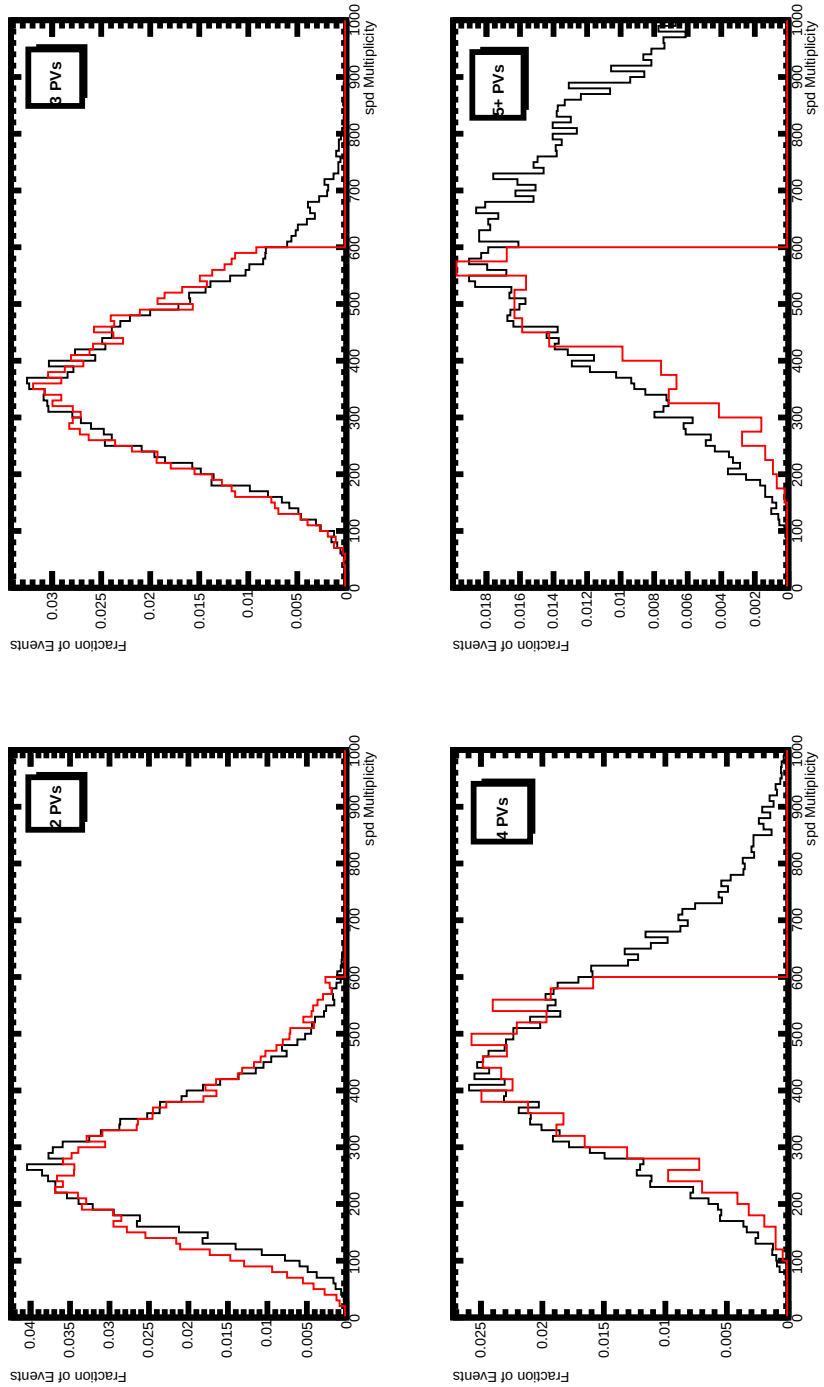

Figure 5.26: From top left clockwise 2 PVs, 3 PVs, 5+ PVs and 4 PVs, in each case the data is shown in red and the mixed no-bias events are in black.

	Mean
2 PV data	275.5 ± 1.9
1 PV + extra tracks	280.32 ± 2.0

Table 5.11: Results of a Gaussian fit to the real data and to the sample made to mimic it to estimate the systematic uncertainty.

To assess the systematic uncertainty on the described method, both the 2 PV data distribution and the constructed data (the red and black curves in figure 5.26) are fitted with the same shape (Gaussian with exponential for the tail). The difference in the mean found between the two shapes is used as a measure of the systematic uncertainty of the method. Table 5.11 shows the values found from the fit. The difference between them, 4.82, equates to a 1.72% shift. Using this as the systematic shift between the real data and the data made to mimic it, the systematic uncertainty is calculated to be 0.05% and is found to be negligible when compared to statistical effects.

Dimuon HLT1 trigger

Events which travel through the dimuon stream must have an SPD multiplicity < 900. The majority of dimuon events have an SPD multiplicity of between 600 and 900 hits (events below this will have triggered the single muon HLT1). To calculate the efficiency here the distribution was fitted with a Gaussian tail to extrapolate in the regime where the events are cut out. This Gaussian tail shape is validated by first using it to fit the 1 PV data sample used in the single muon stream analysis as shown in figure 5.27. The fit clearly matches the shape well in the region that would be cut off in the dimuon stream. The same shape is then fitted to the dimuon events and the distribution is shown in figure 5.28.

To find the systematic uncertainty on this method the number of events under the fitted shape are compared to the actual number found in the distribution. The difference is found to be 1.1% which is comparable with the statistical effect and therefore included. The efficiency calculated for just

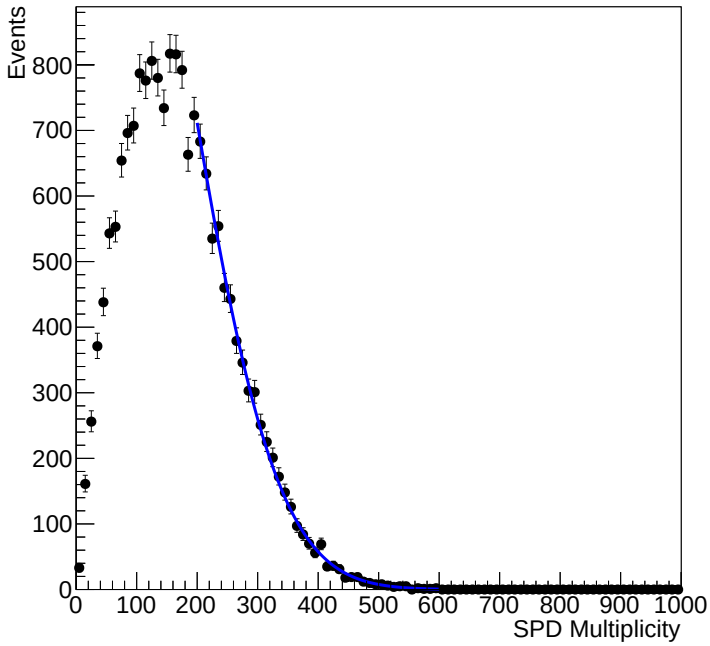

Figure 5.27: SPD multiplicity of the one PV data sample (black), with a fitted Gaussian tail overlaid in blue.

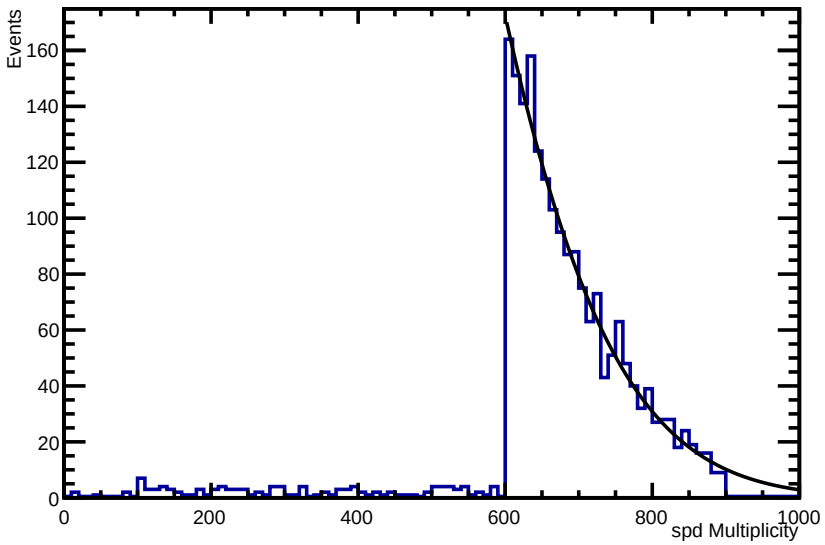

Figure 5.28: SPD multiplicity of events passing through the HLT1 dimuon stream in blue. Overlaid, is the Gaussian tail fitted in the region, 600 < SPD multiplicity < 1200 in black.

	Applicable region	Efficiency	Total uncertainty
Single Muons	1 PV	1	0
	2 PVs	0.995	0.010
	3 PVs	0.945	0.010
	4 PVs	0.787	0.009
	5+ PVs	0.427	0.006
Dimuon	All	0.962	0.034

Table 5.12: GEC efficiencies for each trigger path, as a function of primary vertex multiplicity.

the dimuon stream events is:

$$\epsilon^{GEC}(\text{dimuon only}) = 0.962 \pm 0.031 \pm 0.011. \tag{5.19}$$

Where the first error is the uncertainty due to statistical effects and the second is directly from the method used to estimate the efficiency. These are added in quadrature to find the overall systematic in the table 5.12

The efficiency of the GEC is then calculated on an event by event basis, according to the percentage of total events with each PV multiplicity. This is shown in table 5.12. The overall GEC efficiency is found to be:

$$\epsilon^{GEC} = 0.915 \pm 0.001. \tag{5.20}$$

This result combined with the HLT2 trigger result gives an overall trigger efficiency, $\epsilon^{trig}_{Z\to\mu\mu}$ of:

$$\epsilon^{trig}_{Z\to\mu\mu} = 0.913 \pm 0.013. \tag{5.21}$$

5.7.4 Final state radiation efficiency

The effect of FSR is analysed in simulation. The unreconstructed photon reduces the dimuon invariant mass. This means that events close to the selection threshold of 60 GeV can be lost. This is taken into consideration

with an efficiency measurement. Events are generated with and without FSR included. The efficiency is defined as the number of events which pass the mass selection in the FSR sample compared to those which pass in the non-FSR sample. The FSR efficiency is:

$$\epsilon^{FSR} = 0.993 \pm 0.007. \tag{5.22}$$

5.7.5 Muon tracking efficiency

The muon tracking efficiency is measured using the tag-probe technique. In this case the tag is a long track with $P_T > 20$ GeV, which is an identified muon (as before for the identification efficiency). This muon must have triggered the event. The probe is constructed by taking a standalone track in the muon system. The momentum is found by extrapolating back to the primary vertex. Using this extrapolated track, at least 2 hits must be found in the TT-detector. This allows the entire track to be refitted (a "muonTT" track). The efficiency is calculated by taking the fraction of the number of muonTT track probe events that also have a standard LHCb track identified with them.

For the Z mass region a special study was carried out using the requirements set out in table 5.13. The tracking efficiency distributions can be seen in figure 5.29 as a function of η, ϕ and P_T [70]. It is assumed that there is no dependence arising from charge, η, ϕ and P_T.

The results are shown in table 5.14. Both charges are examined in simulation and in data. The efficiency determined in simulation is higher than that found in data. For the cross-section measurement the data result will be used. Each of the individual results are combined to give an overall efficiency, which is:

$$\epsilon^{track} = 0.846 \pm 0.026. \tag{5.23}$$

Quantity		Cuts
Tag	χ^2 Probability	>0.1%
	$\frac{\sigma P}{P}$	<10%
	Track η	$2.0 \leq 4.5$
	`isMuon`	1
	P_T^{TAG}	≥ 20 GeV
	PID-μ	≥ 4
Probe	χ^2 Probability	0.1%
	$\frac{\sigma P}{P}$	10%
	Track η	$2.0 \leq 4.5$
	P_T^{PROBE}	≥ 20 GeV
	$\text{Mass}_{TAG,PROBE}$	$\lvert Mass_Z^0 - Mass_{Reco}\rvert \leq 25$ GeV
	Z-Vertex χ^2	≤ 5

Table 5.13: All requirements placed on tag and probe tracks to find the muon tracking efficiency [70].

	Data	Simulation
μ^+	0.91 ± 0.02	0.977 ± 0.003
μ^-	0.94 ± 0.02	0.970 ± 0.004

Table 5.14: Muon tracking efficiency numbers for data and simulation [70].

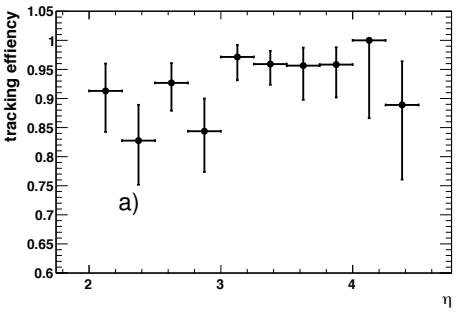

(a) Muon η.

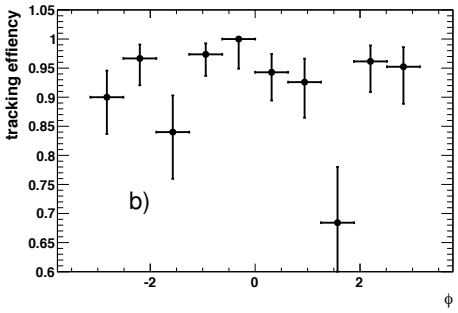

(b) Muon ϕ.

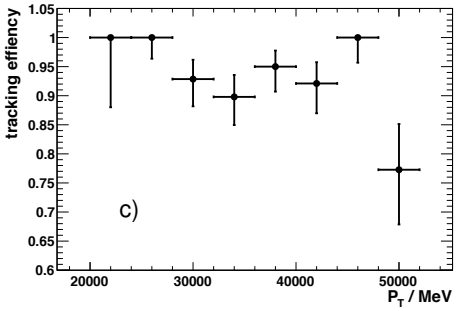

(e) Muon P_T.

Figure 5.29: Muon tracking efficiency with respect to (a) muon η, (b) muon ϕ, (c) muon P_T. The negative and positive muons are combined [70].

Source	Efficiency
Muon ID (ϵ^{ID})	0.962 ± 0.009
Trigger (ϵ^{trig})	0.913 ± 0.013
FSR (ϵ^{FSR})	0.993 ± 0.007
Tracking (ϵ^{track})	0.846 ± 0.026
Acceptance (A^{geom})	0.999 ± 0.003
Total efficiency	0.737 ± 0.021

Table 5.15: Summary of efficiency results. Each individual efficiency is quoted for a $Z \to \mu\mu$ event, not an individual muon. The total efficiency is the overall efficiency for measuring a $Z \to \mu\mu$ event.

5.7.6 Acceptance

The acceptance, A^{geom}, takes into account inefficiencies in the detector response, i.e., under measuring the muon P_T so the event is cut by the selections. This effect is measured by taking the ratio of events in simulation which pass the selection requirements at the simulated level compared to the number which pass at the truth level. This gives a result of:

$$A^{geom} = 0.999 \pm 0.003. \tag{5.24}$$

For this measurement no correction to expand the measurement to 4π is done. We measure only in the fiducial volume. Therefore, there is no further acceptance inefficiency.

The different sources of inefficiency are summarised in table 5.15. The overall efficiency for recording a $Z \to \mu\mu$ event is calculated to be:

$$\epsilon^{total} = 0.737 \pm 0.021. \tag{5.25}$$

5.8 Systematic uncertainty

The systematic uncertainties arising on the total cross section measurement originate from the number of background events, the efficiencies, and from the integrated luminosity.

Systematic uncertainties arising from background contributions

The systematic error arising from the number of background events in the $Z \to \tau\tau$, $W + W \to \mu\mu$, and the same-sign samples is calculated statistically from the number of events passing the selections. These are 7.1%, 2.4%, 19% respectively. The systematic uncertainty from $t\bar{t}$ is 92% because it is statistically limited with only three events successfully passing the selections. However, since the background simulation samples are at leading order the number of events may be underestimated. Any uncertainty due to higher order effects is not included.

The systematic error on the heavy flavour contribution is not found statistically. It is found by calculating the difference between the fitted exponential, and the data. The systematic error is 2.1%.

The hadron mis-identification error is evaluated by propagating the errors found on each of the fit parameters set out in table 5.6. It is calculated to be 59%. This high percentage is due to the high uncertainty on the second parameter, b (from the table 5.6 and equation 5.10).

Systematic uncertainties arising from efficiency calculations

The systematic uncertainty on the identification, HLT2 trigger efficiency, tracking efficiency and acceptance are calculated from the statistical uncertainty on the data. These values are calculated as 0.9%, 1.3%, 3.1% and 0.3% respectively. The uncertainty arising from FSR is 0.7%, this does not take into account any uncertainty due to the theoretical knowledge of FSR production.

Source of error	Percentage uncertainty
Muon ID efficiency	0.9
Trigger efficiency	1.3
Tracking efficiency	3.1
FSR	0.7
Acceptance	0.3
Backgrounds	2.7
Luminosity	3.5

Table 5.16: Each source of systematic uncertainty and its percentage error.

The total systematic uncertainty arising from the GEC efficiency is calculated to be 0.1%. The main contribution to this comes from the dimuon HLT1 analysis. This is due to the difference between the fitted shape and the data, and because there are lower statistics compared to the single muon stream.

The tracking and integrated luminosity errors come directly from the tracking [47] and luminosity [71] groups. These are 3.1% and 3.5% respectively.

5.9 Fitting the data

Figure 5.30 shows all of the candidates passing the selection criteria. These are fitted with the same combination of shapes detailed in chapter 4.

Figure 5.31 shows the fit of a Voigtian with a Crystal Ball in simulation. The width of the Crystal Ball is 1.48 GeV and the width of the Voigtian is 3.14 GeV. The mean is kept constant between the two shapes (91.15 GeV), and all other parameters are left free. This shape fits the simulation well. The same combination is used on data, shown in figure 5.32, where the widths of the Crystal Ball and Voigtian are 1.99 GeV and 4.09 GeV, respectively. The mean is fitted at 91.01 GeV.

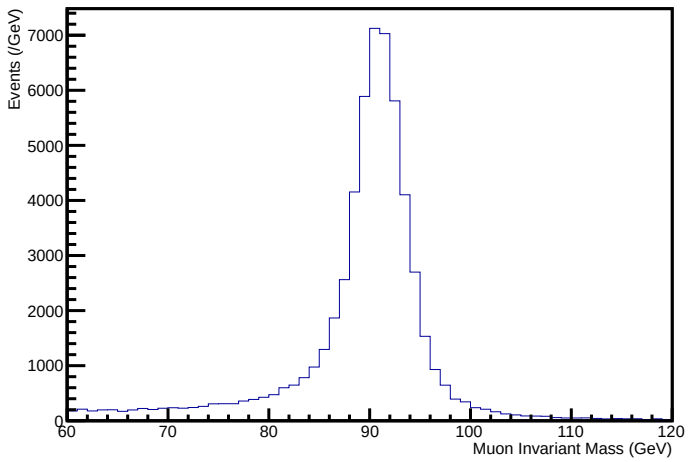

Figure 5.30: The muon invariant mass of selected signal events.

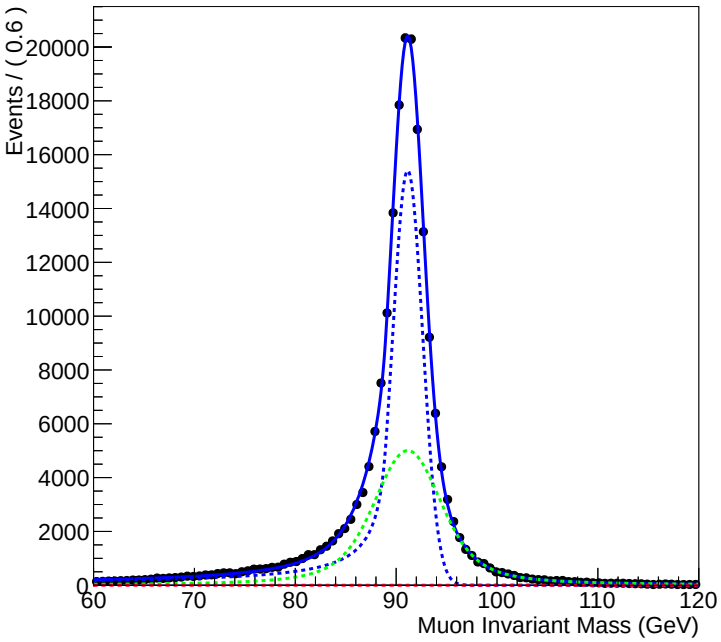

Figure 5.31: Fitted MC - a Crystal Ball (blue) with a Voigtian (green) on an exponential background (red).

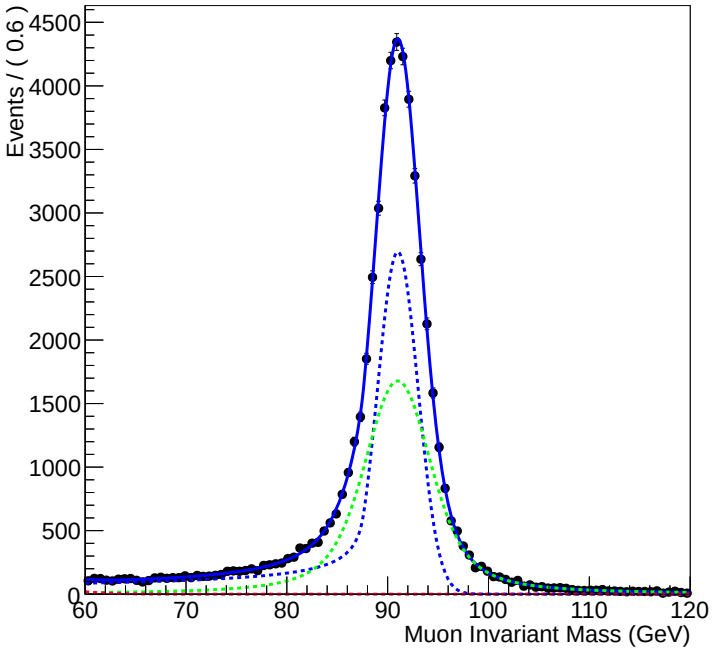

Figure 5.32: Fitted data - a Crystal Ball (blue) with a Voigtian (green) on an exponential background (red).

N($Z \to \mu\mu$)		56449 ± 238
N(Backgrounds)	$Z \to \tau\tau$	14.0 ± 1.0
	$t\bar{t} \to \mu\mu$	0.12 ± 0.11
	$WW \to \mu\mu$	4.1 ± 0.1
	Heavy flavour	207.5 ± 4.4
	Mis-id	2.2 ± 1.3
	Same-sign	27 ± 5.2
Efficiencies	ID	0.962 ± 0.009
	Trigger	0.913 ± 0.013
	Tracking	0.846 ± 0.031
	FSR	0.993 ± 0.007
	Acceptance	0.999 ± 0.003
Integrated Luminosity (pb^{-1})		1028 ± 36

Table 5.17: A summary of all of the numbers used in the cross-section measurement. Firstly, the number of Z candidates found and statistical error. All of the background contributions are summarised and their respective systematic errors. Each efficiency and its uncertainty, followed by the total integrated luminosity analysed and uncertainty from the LHCb luminosity group.

5.10 Cross-section measurement

Using equations 5.14 and 5.15, the cross-section can now be calculated. Table 5.17 summarises all the individual components.

$$\begin{aligned}\sigma_{Z\to\mu\mu}\,(2 < \eta_\mu < 4.5,\ P_T^\mu > 20\ \text{GeV},\ 60 < M_{\mu\mu} < 120\ \text{GeV}) = \\ (74.2\ \pm 0.4\ (\text{stat})\ \pm 2.0\ (\text{sys})\ \pm 2.6\ (\text{lumi}))\ \text{pb}\end{aligned} \tag{5.26}$$

5.11 Comparison to theory

Using this data, comparisons can be made to theory predictions. As discussed in chapter 2, this measurement can be used to provide information to con-

strain PDFs. Theoretical kinematic distributions have been produced at the NLO level to compare with the data. RESBOS [22, 72, 73] and POWHEG [74, 23, 75, 76] are used with the CTEQ6.6 PDF set and FEWZ [24, 77] is used with the MSTW2008 PDF set.

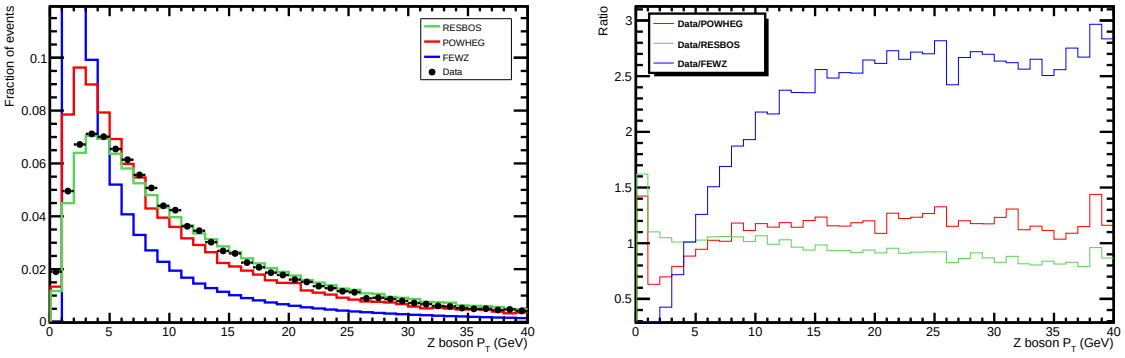

(a) Z P_T. (b) Z P_T ratio.

Figure 5.33: (a) Z P_T comparison between RESBOS (green), POWHEG (red), FEWZ (blue) and data (black points). (b) The ratio of data/POWHEG (red), data/RESBOS (green) and data/FEWZ (blue) vs Z P_T.

The Z P_T distribution is shown in figure 5.33(a), where data is in black, RESBOS in green, POWHEG in red and FEWZ in blue. POWHEG matches the data well at high P_T's where NLO contributions enter but describes it poorly at the peak where resummation effects (contained in RESBOS) are important. FEWZ overestimates the peak, and describes the tail poorly. In (b) the ratio of data to each of the generators is shown. Here it can be seen that over the entire P_T range RESBOS describes the distribution more accurately than POWHEG. This is because it specialises in the resummation of the transverse momentum of the Z.

In figure 5.34(a) the Z rapidity, Z_y, is shown, where data is in black, RESBOS in green, POWHEG in red and FEWZ in blue. FEWZ and POWHEG

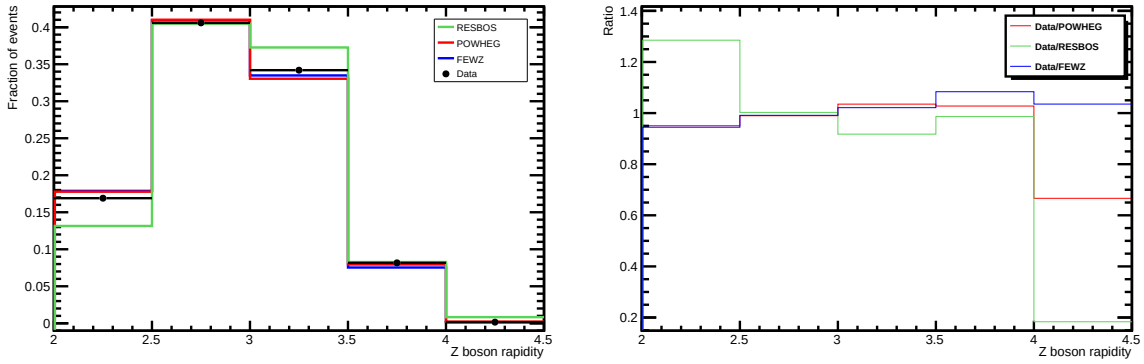

(a) Z rapidity. (b) Z rapidity ratio.

Figure 5.34: (a) Z rapidity comparison between RESBOS (green), POWHEG (red), FEWZ (blue) and data (black points). (b) The ratio of data/POWHEG (red), data/RESBOS (green) and data/FEWZ (blue) vs Z rapidity.

describe the data well, and RESBOS matches reasonably well in the central three bins. Using the ratios illustrated in (b) the very forward region, $4 < Z_y < 4.5$, is not described particularly well by RESBOS or POWHEG. However, the POWHEG result is still consistent with the data within uncertainties. FEWZ describes the whole rapidity range well.

The muon P_T is shown in figure 5.35(a) and the ratio between data and the generators in (b). POWHEG describes the data here better than RESBOS and FEWZ. POWHEG shows a slight underestimate of the muon P_T in both the lower momentum tail and above $\sim$ 50 GeV. All three generators overestimate the peak ($\sim$ 43 GeV), which is probably due to not modelling FSR.

Muon pseudorapidity is shown in figure 5.36(a) with the ratio of data to each generator in (b). POWHEG and FEWZ describe the data excellently. Though POWHEG is more accurate in the highest bin. RESBOS describes the data reasonably in the region between $3.5 < \eta < 4.5$.

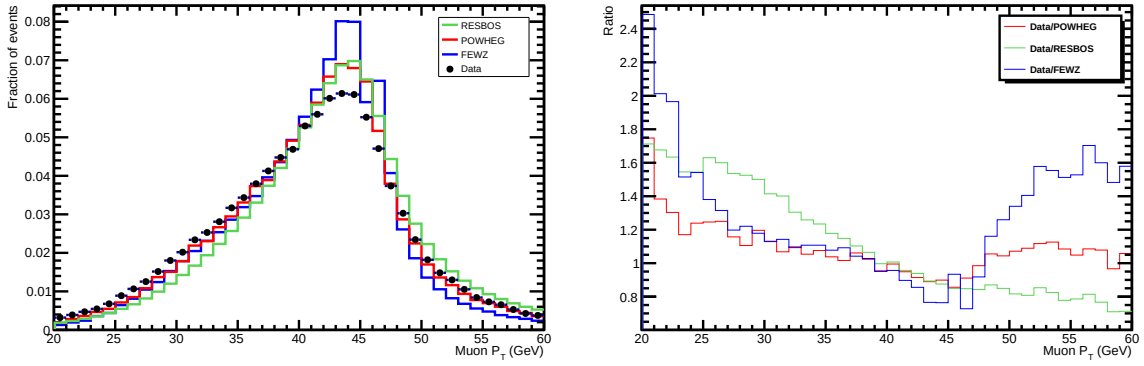

(a) Muon P_T. (b) Muon P_T ratio.

Figure 5.35: (a) Muon P_T comparison between RESBOS (green), POWHEG (red), FEWZ (blue) and data (black points). (b) The ratio of data/POWHEG (red), data/RESBOS (green) and data/FEWZ (blue) vs muon P_T.

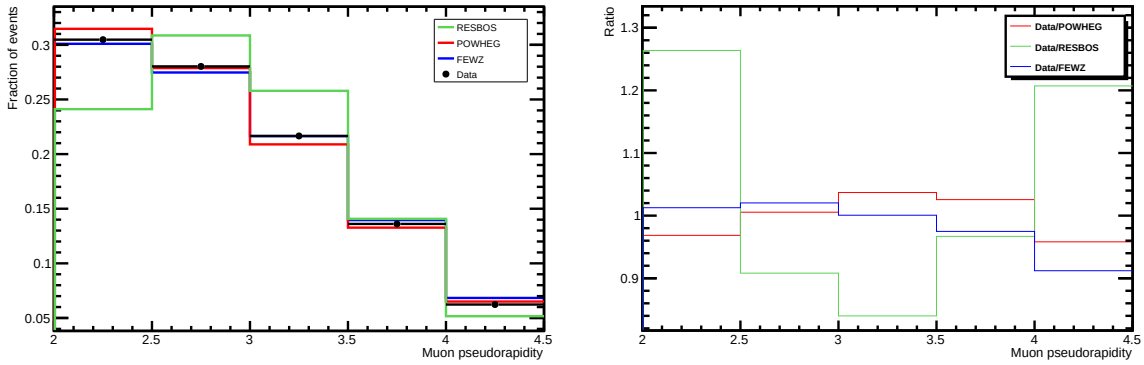

(a) Muon pseudorapidity. (b) Muon pseudorapidity ratio.

Figure 5.36: (a) Muon η comparison between RESBOS (green), POWHEG (red), FEWZ (blue) and data (black points). (b) The ratio of data/POWHEG (red), data/RESBOS (green) and data/FEWZ (blue) vs muon η.

Source	Result
Data	74.2 ± 3.3
POWHEG	72.2 ± 5.5
RESBOS	70.1 ± 5.3
FEWZ	74.8 ± 2.8

Table 5.18: Cross-section measurements over the pseudorapidity range, $2.0 < \eta_\mu < 4.5$. Data is shown at the top followed by three different generator results (POWHEG, RESBOS and FEWZ).

5.12 Cross-section comparison

In addition to comparing the kinematic variable discussed above, the cross-sections can be compared directly.

5.12.1 Overall cross-section comparison

Using the cross-section calculated in section 5.10, the data can be compared to different theoretical results. Table 5.18 summarises the overall result from data and three generators.

Overall the best agreement is seen between data and FEWZ. All of the theory results are consistent with data within the stated errors.

5.12.2 Differential cross-section comparison

The differential cross section with respect to the Z rapidity is shown in figure 5.37. Also illustrated is RESBOS and POWHEG with the CTEQ6.6 PDF set, and FEWZ with the MSTW2008 PDF set. RESBOS underestimates the cross-section at boson rapidities < 3, but describes the high rapidity bins well. POWHEG and FEWZ both describe the data result well over the whole rapidity range.

The results from each generator and data are tabulated in table 5.19.

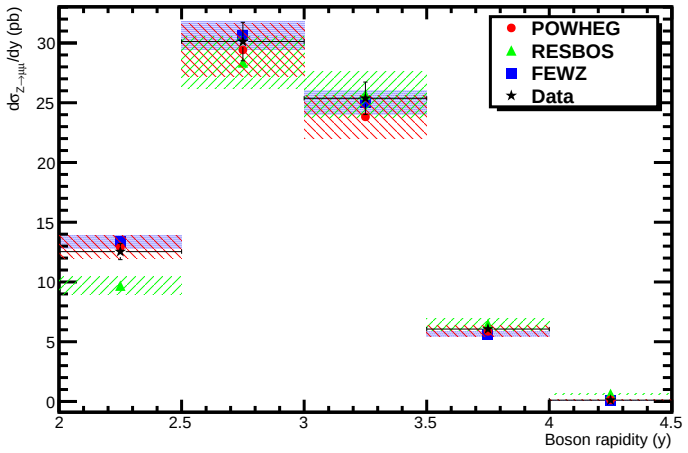

Figure 5.37: The differential cross section, $\frac{d\sigma}{dy}$. Data is shown in black, RESBOS in green, POWHEG in red and FEWZ in blue. The total uncertainty is shown on the data points, and the PDF uncertainty is shown on the generator predictions (coloured bands).

Rapidity	**Data**	**POWHEG**	**RESBOS**	**FEWZ**
2.0 - 2.5	12.54 ± 0.67	12.91 ± 0.98	9.69 ± 0.73	13.37 ± 0.55
2.5 - 3.0	30.12 ± 1.61	29.42 ± 2.23	28.37 ± 2.15	30.61 ± 1.18
3.0 - 3.5	25.37 ± 1.36	23.82 ± 1.81	25.69 ± 1.95	25.03 ± 0.98
3.5 - 4.0	6.06 ± 0.32	5.87 ± 0.45	6.48 ± 0.50	5.63 ± 0.23
4.0 - 4.5	0.11 ± 0.006	0.13 ± 0.01	0.64 ± 0.05	0.11 ± 0.007

Table 5.19: Results of a differential cross-section measurement in data and different generators (POWHEG, RESBOS and FEWZ) with respect to Z boson rapidity.

5.13 Conclusion

The $Z \rightarrow \mu\mu$ cross-section between the pseudorapidities of 2 and 4.5 is measured to be 74.2 $\pm$ 0.4 (stat) $\pm$ 2.0 (sys) $\pm$ 2.6 (lumi) pb. This result is consistent with NLO predictions. A differential measurement with respect to the rapidity of the Z boson is shown in figure 5.37. Each bin is consistent with the predictions of both POWHEG and FEWZ. RESBOS describes the Z boson P_T distribution well over the full range considered. Both POWHEG and FEWZ describe the Z rapidity and muon pseudorapidity well. This analysis would benefit from more data in the high Z rapidity range. This would provide a more precise constraint of PDFs. The result between muon pseudorapidities of 2 and 2.5 does not directly compare with ATLAS and CMS because the result presented here is defined by the muon pseudorapidity, not the Z boson rapidity.

Chapter 6

Summary

This thesis has detailed an analysis of the $Z \to \mu\mu$ decay. An individual cross-section measurement and differential cross-section with respect to Z boson rapidity have been presented. Final state radiation has been implemented in the LHCb simulation chain for the first time. This sample has been used to analyse the effect of FSR on the reconstructed Z mass.

Final state radiation causes the dimuon invariant mass distribution to shift to a lower mean and the peak becomes wider. The primary motivations for reconstructing radiated photons are to improve the invariant mass resolution, and to correct for the mass shift. With an initial photon selection a slight improvement was found in simulation. The resulting mass distribution was fitted with a Voigtian and Crystal Ball shape. This results in a Z mass peak shift from 91.047 GeV to 91.054 GeV. The width of the distribution is also found to be reduced by 12% (the Voigtian reduces from 4.07 to 3.76, and Crystal Ball from 1.92 to 1.51).

The most important motivations for measuring the $Z \to \mu\mu$ cross-section are to probe the Standard Model, and to constrain PDFs in poorly understood regions. Signal event characteristics are discussed in detail. The kinematic selections are: muon $P_T > 20$ GeV; $60 < M_{\mu\mu} < 120$ GeV; and $2 < \eta_\mu < 4.5$. These are justified using simulation. Additionally, simulated background processes have illustrated how these requirements reduce back-

ground contamination. This selection yields 56449 signal candidates from 1.03 fb^{-1} of data. The number of background events is estimated to be 254.9 ± 7.0.

The overall efficiency has been calculated from data driven techniques where possible. The muon identification, HLT2 and tracking efficiencies are all measured using the tag and probe method. The efficiency due to the global event cuts was also measured from data. The final state radiation correction was calculated from simulation. The individual results are combined, and the overall efficiency is 0.74 ± 0.02.

The overall cross-section is measured to be:

$$\sigma_{Z\to\mu\mu}\,(2 < \eta_\mu < 4.5,\ P_T^\mu > 20\ \text{GeV},\ 60 < M_{\mu\mu} < 120\ \text{GeV}) =$$
$$(74.2\ \pm 0.4\ (\text{stat})\ \pm 2.0\ (\text{sys})\ \pm 2.6\ (\text{lumi}))\ \text{pb}.$$

This result has been compared to three generators: RESBOS; POWHEG; and FEWZ with PDF sets CTEQ6.6 and MSTW2008. The cross-section measurement was consistent with each NLO prediction. The differential measurement with respect to the Z boson rapidity agreed well in each bin with both POWHEG and FEWZ.

Direct comparisons with the ATLAS and CMS results are difficult because the bin boundaries are different. However, the measurements quoted from both experiments are consistent with NLO predictions. This indicates that the above results would also be consistent with other experimental results.

The systematic uncertainty on the overall measurement has large contributions from statistically limited sources. This could be reduced with more data. More accuracy in the forward region ($\eta_\mu > 4$) would also lead to better understanding of proton behaviour, and allow further PDF development.

Chapter 7

Appendix A

7.1 Additional efficiency figures

In this appendix there are additional efficiency figures for simulation and for different polarities not included in the main body of this thesis. For the method please refer to the techniques described in chapter 5. These figures are placed here for additional information and cross-checking the results already discussed.

The following figures are set out as follows. The muon identification efficiency with respect to muon P_T, muon η, muon ϕ, number of primary vertices and Z P_T. Followed by the muon HLT2 trigger efficiency with respect to muon P_T, muon η, muon ϕ, number of primary vertices and Z P_T. Each set of figures shows the top left, mag up data; top right, mag down data; bottom left, mag up simulation and lastly bottom right, mag down simulation.

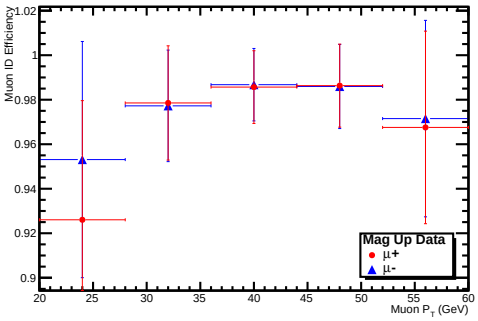

(a) Data: Magnet up

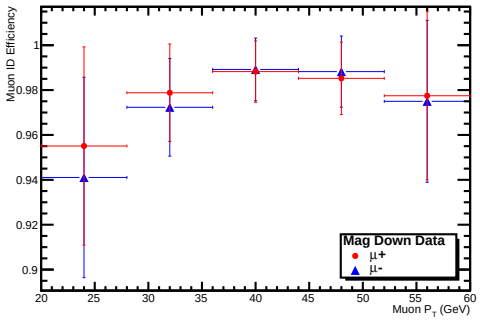

(b) Data: Magnet down

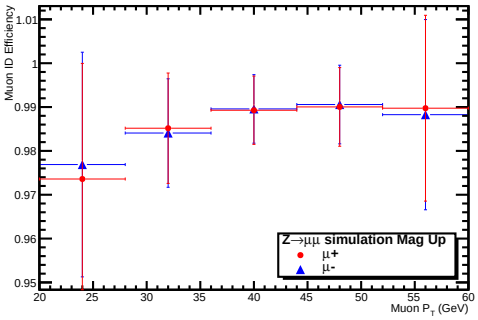

(c) Simulation: Magnet up

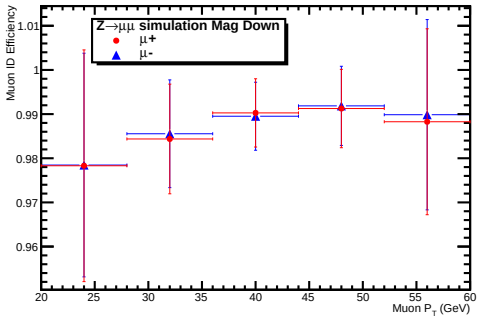

(d) Simulation: Magnet down

Figure 7.1: Muon ID efficiency with respect to muon P_T in (a) Magnet up data, (b) Magnet down data, (c) Magnet up simulation and (d) Magnet down simulation, in each case the result for the positive (negative) muon is shown in red (blue).

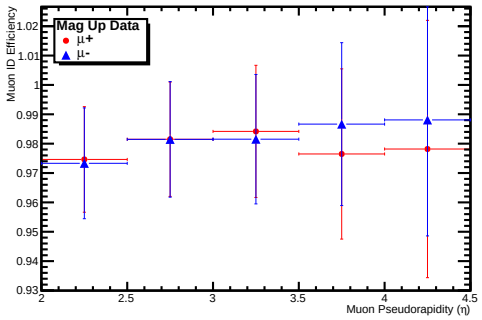

(a) Data: Magnet up

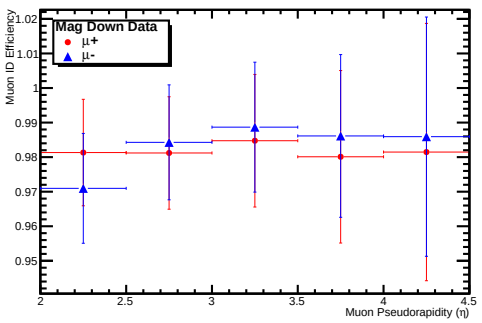

(b) Data: Magnet down

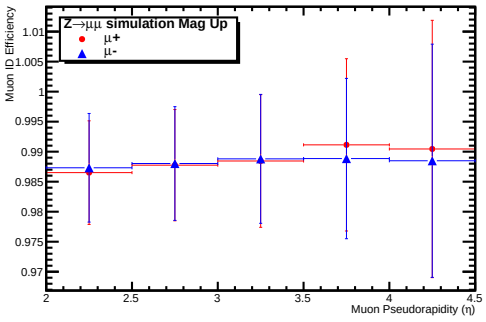

(c) Simulation: Magnet up

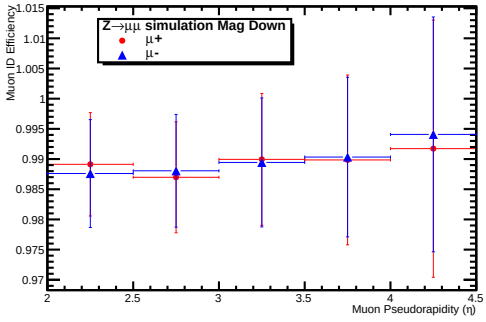

(d) Simulation: Magnet down

Figure 7.2: Muon ID efficiency with respect to muon η in (a) Magnet up data, (b) Magnet down data, (c) Magnet up simulation and (d) Magnet down simulation, in each case the result for the positive (negative) muon is shown in red (blue).

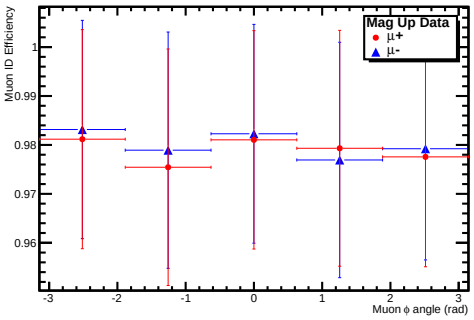

(a) Data: Magnet up

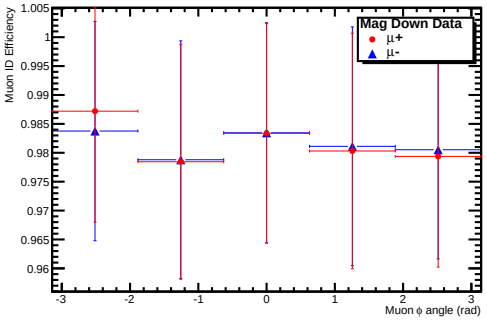

(b) Data: Magnet down

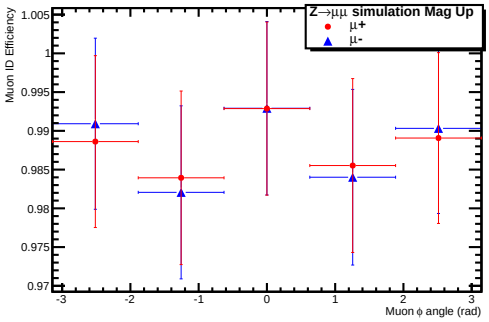

(c) Simulation: Magnet up

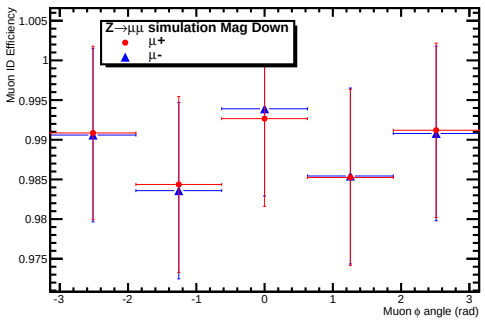

(d) Simulation: Magnet down

Figure 7.3: Muon ID efficiency with respect to muon ϕ in (a) Magnet up data, (b) Magnet down data, (c) Magnet up simulation and (d) Magnet down simulation, in each case the result for the positive (negative) muon is shown in red (blue).

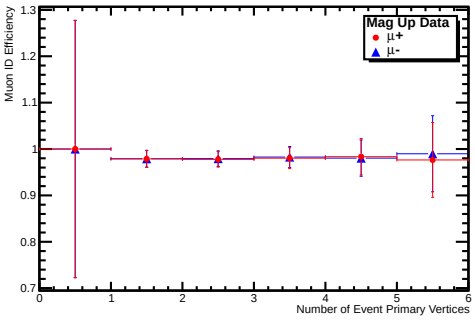

(a) Data: Magnet up

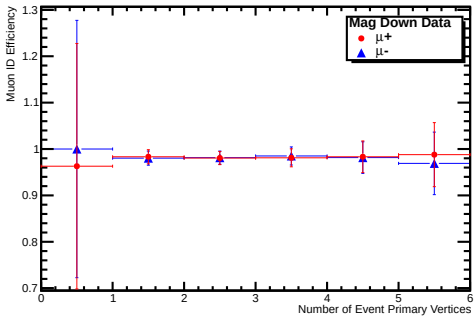

(b) Data: Magnet down

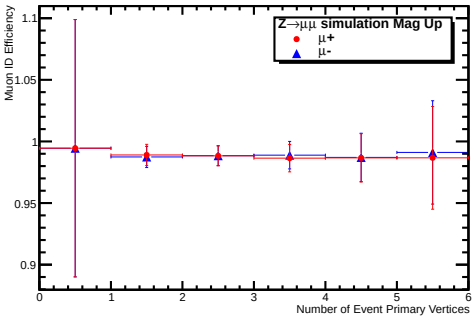

(c) Simulation: Magnet up

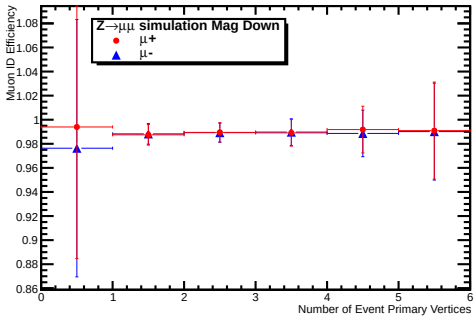

(d) Simulation: Magnet down

Figure 7.4: Muon ID efficiency with respect to the number of primary vertices in (a) Magnet up data, (b) Magnet down data, (c) Magnet up simulation and (d) Magnet down simulation, in each case the result for the positive (negative) muon is shown in red (blue).

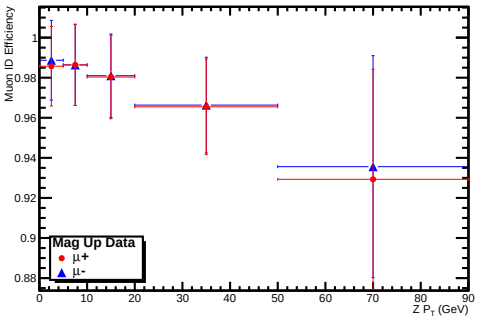

(a) Data: Magnet up

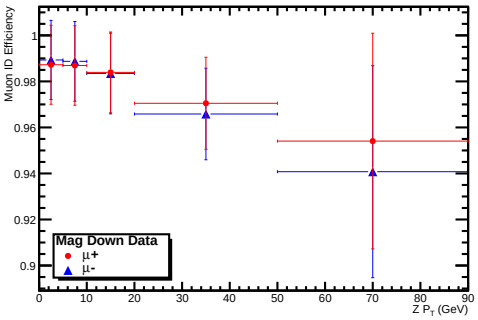

(b) Data: Magnet down

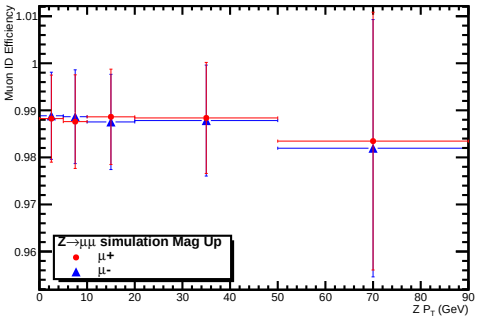

(c) Simulation: Magnet up

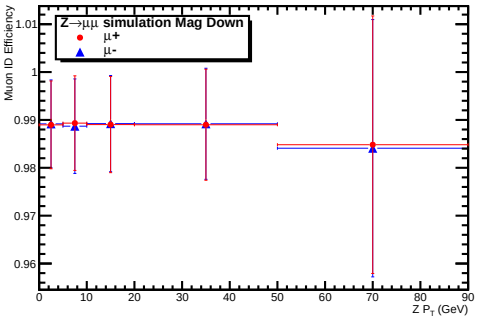

(d) Simulation: Magnet down

Figure 7.5: Muon ID efficiency with respect to the Z P_T in (a) Magnet up data, (b) Magnet down data, (c) Magnet up simulation and (d) Magnet down simulation, in each case the result for the positive (negative) muon is shown in red (blue).

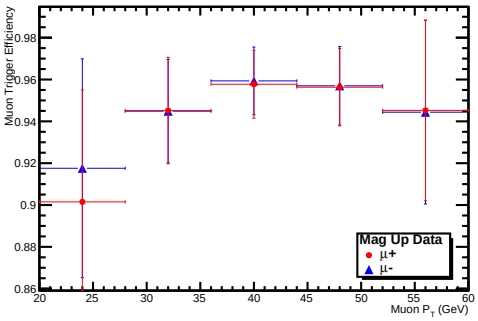

(a) Data: Magnet up

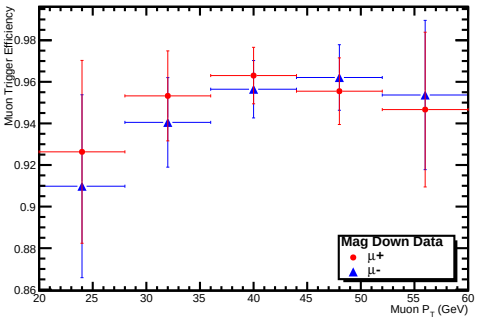

(b) Data: Magnet down

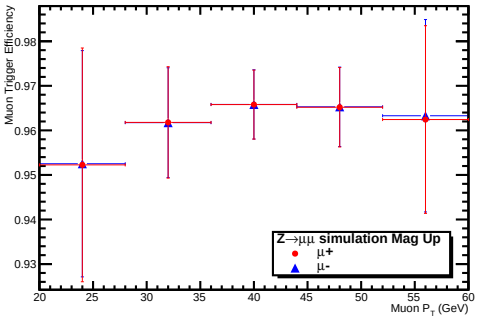

(c) Simulation: Magnet up

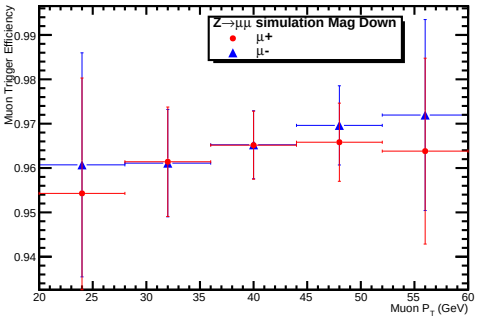

(d) Simulation: Magnet down

Figure 7.6: Muon HLT2 trigger efficiency with respect to muon P_T in (a) Magnet up data, (b) Magnet down data, (c) Magnet up simulation and (d) Magnet down simulation, in each case the result for the positive (negative) muon is shown in red (blue).

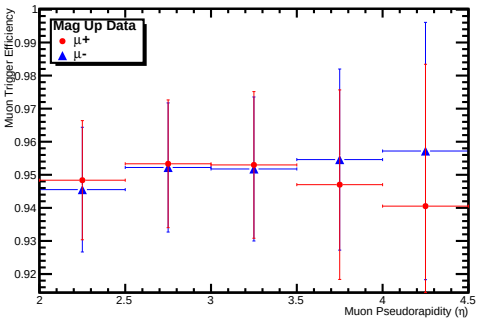

(a) Data: Magnet up

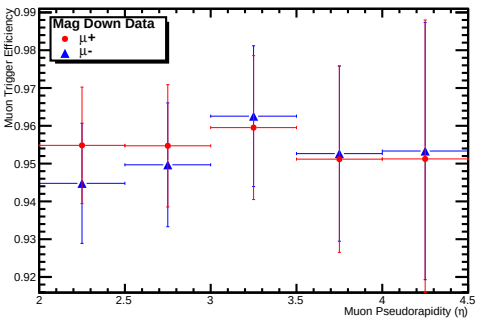

(b) Data: Magnet down

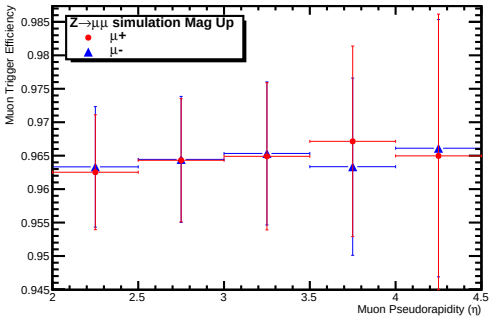

(c) Simulation: Magnet up

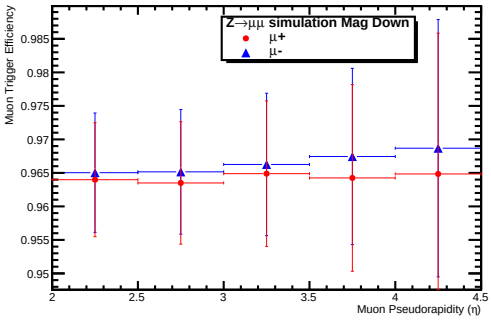

(d) Simulation: Magnet down

Figure 7.7: Muon HLT2 trigger efficiency with respect to muon η in (a) Magnet up data, (b) Magnet down data, (c) Magnet up simulation and (d) Magnet down simulation, in each case the result for the positive (negative) muon is shown in red (blue).

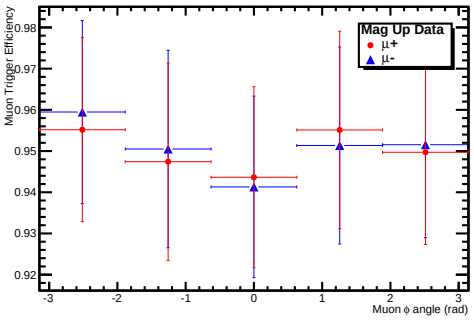

(a) Data: Magnet up

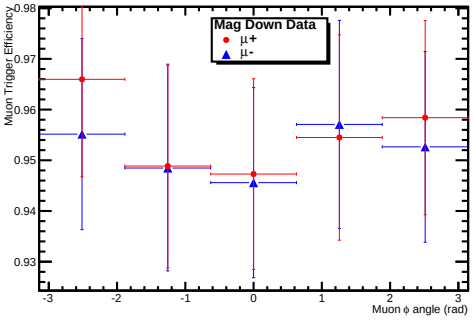

(b) Data: Magnet down

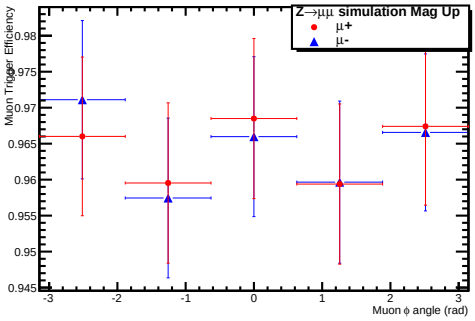

(c) Simulation: Magnet up

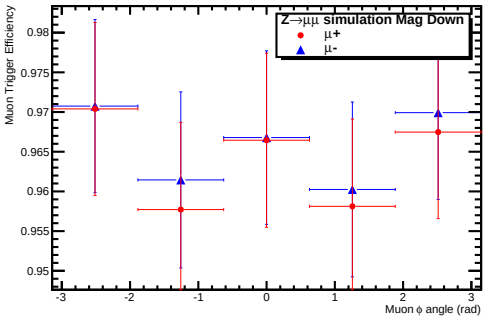

(d) Simulation: Magnet down

Figure 7.8: Muon HLT2 trigger efficiency with respect to muon ϕ in (a) Magnet up data, (b) Magnet down data, (c) Magnet up simulation and (d) Magnet down simulation, in each case the result for the positive (negative) muon is shown in red (blue).

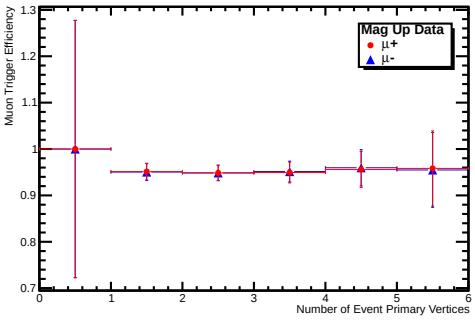

(a) Data: Magnet up

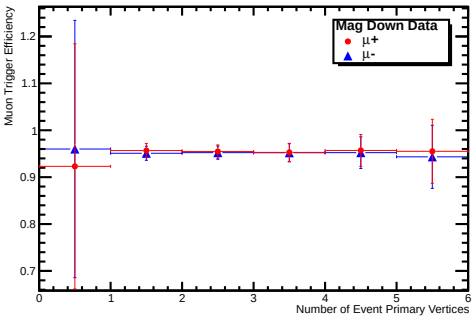

(b) Data: Magnet down

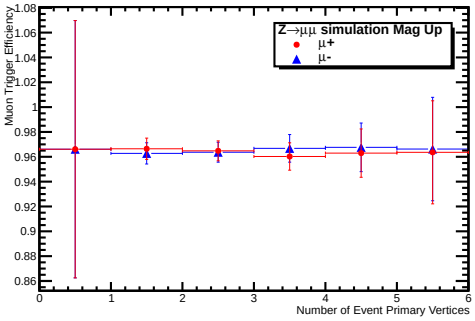

(c) Simulation: Magnet up

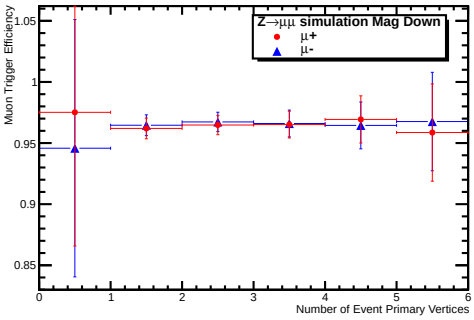

(d) Simulation: Magnet down

Figure 7.9: Muon HLT2 trigger efficiency with respect to the number of primary vertices in (a) Magnet up data, (b) Magnet down data, (c) Magnet up simulation and (d) Magnet down simulation, in each case the result for the positive (negative) muon is shown in red (blue).

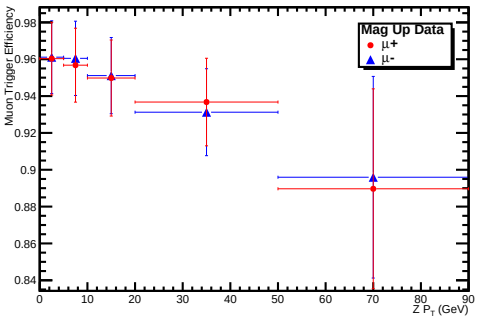

(a) Data: Magnet up

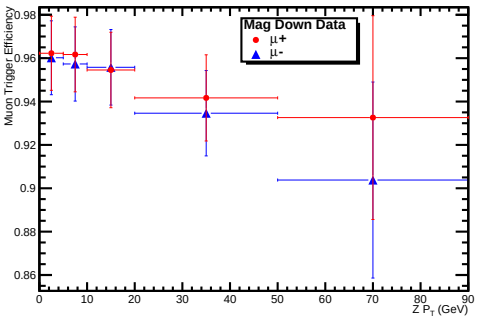

(b) Data: Magnet down

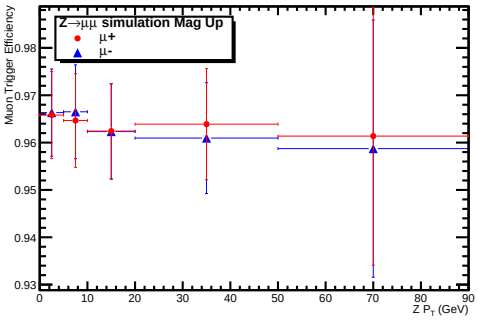

(c) Simulation: Magnet up

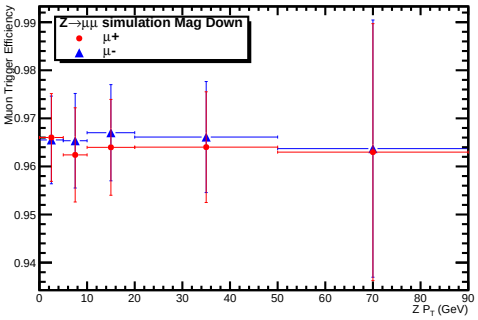

(d) Simulation: Magnet down

Figure 7.10: Muon HLT2 trigger efficiency with respect to the Z P_T in (a) Magnet up data, (b) Magnet down data, (c) Magnet up simulation and (d) Magnet down simulation, in each case the result for the positive (negative) muon is shown in red (blue).

Bibliography

[1] D. Griffiths, *Introduction to elementary particles*. John Wiley and Sons Inc, 2008.

[2] I. Aitchison and A. Hey, *Gauge theories in particle physics: A practical introduction. Vol. 2: Non-Abelian gauge theories: QCD and the electroweak theory*. CRC Press, 2004.

[3] W. Murray, G. Birch, and J. Graham, *Proceedings of the school for experimental high energy physics students*, Tech. Rep. RAL-TR-2010-010, RAL, Oxford, Sept, 2009.

[4] P. A. Dirac, *On the Theory of quantum mechanics*, *Proc.Roy.Soc.Lond.* **A112** (1926) 661–677.

[5] G. L. Kane, *Modern Elementary Particle Physics*. Westview Press, 1987.

[6] F. Mandl and G. Shaw, *Quantum Field Theory*. Wiley-Blackwell, 1985.

[7] A. Pich, *Quantum chromodynamics*, `arXiv:hep-ph/9505231`.

[8] P. Renton, *Electroweak Interactions: An Introduction to the Physics of Quarks and Leptons*. Cambridge University Press, 1990.

[9] M. Kobayashi and T. Maskawa, *CP Violation in the Renormalizable Theory of Weak Interaction*, *Prog.Theor.Phys.* **49** (1973) 652–657.

[10] P. W. Higgs, *Broken symmetries and the masses of gauge bosons*, *Phys. Rev. Lett.* **13** (Oct, 1964) 508–509.

[11] J. Goldstone, *Field theories with superconductor solutions*, *Il Nuovo Cimento (1955-1965)* **19** (1961) 154–164.

[12] H. Yukawa, *On the interaction of elementary particles*, *Proc.Phys.Math.Soc.Jap.* **17** (1935) 48–57.

[13] R. P. Feynman, *Very high-energy collisions of hadrons*, *Phys. Rev. Lett.* **23** (Dec, 1969) 1415–1417.

[14] J. C. Collins and D. E. Soper, *The Theorems of Perturbative QCD*, *Ann.Rev.Nucl.Part.Sci.* **37** (1987) 383–409.

[15] Martin, Stirling, Thorne, and Watt, *MSTW Parton Distribution Functions*, May, 2012.

[16] G. Altarelli and G. Parisi, *Asymptotic Freedom in Parton Language*, *Nucl.Phys.* **B126** (1977) 298.

[17] CTEQ collaboration, *CTEQ Parton Distribution Functions - http://www.phys.psu.edu/cteq/#PDFs*, May, 2012.

[18] NNPDF development group, *http://nnpdf.hepforge.org/*, July 2012.

[19] K. Hennessy, *LHCb - Studies of electroweak boson production in the forward region with LHCb* , April 2011.

[20] S. D. Drell and T.-M. Yan, *Massive lepton-pair production in hadron-hadron collisions at high energies*, *Phys. Rev. Lett.* **25** (Aug, 1970) 316–320.

[21] Particle Data Group, *Review of particle physics*, *J.Phys.G* **G37** (2010) 075021.

[22] C. Balazs and C. Yuan, *Soft gluon effects on lepton pairs at hadron colliders*, *Phys.Rev.* **D56** (1997) 5558–5583.

[23] S. Frixione, P. Nason, and C. Oleari, *Matching NLO QCD computations with Parton Shower simulations: the POWHEG method*, *JHEP* **0711** (2007) 070.

[24] R. Gavin, Y. Li, F. Petriello, and S. Quackenbush, *FEWZ 2.0: A code for hadronic Z production at next-to-next-to-leading order*, *Comput.Phys.Commun.* **182** (2011) 2388–2403, [arXiv:1011.3540].

[25] C. Carloni Calame, G. Montagna, O. Nicrosini, and A. Vicini, *Precision electroweak calculation of the production of a high transverse-momentum lepton pair at hadron colliders*, *JHEP* **0710** (2007) 109, [arXiv:0710.1722].

[26] P. Golonka and Z. Was, *PHOTOS Monte Carlo: A Precision tool for QED corrections in Z and W decays*, *Eur.Phys.J.* **C45** (2006) 97–107, [arXiv:hep-ph/0506026].

[27] ATLAS Collaboration, G. Aad et al., *Measurement of the inclusive W+- and Z/gamma cross sections in the electron and muon decay channels in pp collisions at sqrt(s) = 7 TeV with the ATLAS detector*, *Phys.Rev.* **D85** (2012) 072004, [arXiv:1109.5141].

[28] CMS Collaboration, S. Chatrchyan et al., *Measurement of the Rapidity and Transverse Momentum Distributions of Z Bosons in pp Collisions at sqrt(s)=7 TeV*, *Phys.Rev.* **D85** (2012) 032002, [arXiv:1110.4973].

[29] e. Evans, Lyndon and e. Bryant, Philip, *LHC Machine*, *JINST* **3** (2008) S08001.

[30] LHC public page, *http://public.web.cern.ch/public/en/research/AccelComplex-en.html*, February 2012.

[31] LHC linac page, *http://linac2.home.cern.ch/linac2/default.htm*, May 2012.

[32] A closer look at LHC, *http://www.lhc-closer.es/php/index.php*, May 2012.

[33] Project to prepare the PS Complex to be a Pre-injector for the LHC, *http://ps-div.web.cern.ch/ps-div/LHC-PS/LHC-PS.html*, May 2012.

[34] SPS Group, *http://sl.web.cern.ch/SL/sli/sli.html*, May 2012.

[35] LHCb Collaboration, *The LHCb Detector at the LHC*, *JINST* **3 S08005** (2008).

[36] LHCb publication figures, *http://lhcb.web.cern.ch/lhcb/speakersbureau /html/bb_ProductionAngles.html*, May 2012.

[37] LHCb Collaboration, *LHCb VELO TDR: Vertex locator. Technical design report.* 2001.

[38] LHCb VELO group, *https://lbtwiki.cern.ch/bin/view/VELO /VELO-ConferencePlots/ #HitResolution*, Jan 2012.

[39] LHCb Collaboration, *LHCb inner tracker: Technical Design Report.* Technical Design Report LHCb. CERN, Geneva, 2002.

[40] LHCb IT group, *http://lhcb.physik.uzh.ch/ST/public/material/ index.php*, Jan 2012.

[41] LHCb collaboration, *LHCb: Outer tracker technical design report.* 2001.

[42] LHCb Collaboration, *LHCb magnet: Technical design report.* 2000.

[43] LHCb Collaboration, *LHCb RICH: Technical Design Report.* Technical Design Report LHCb. CERN, Geneva, 2000.

[44] LHCb Collaboration, *LHCb calorimeters: Technical design report.* 2000.

[45] LHCb Collaboration, *LHCb muon system technical design report.* 2001.

[46] T. Meinschad and F. Sauli, *GEM - A novel gaseous particle detector. oai:cds.cern.ch:878708.* PhD thesis, Vienna, Tech. U., Vienna, 2005. Presented on 22 Jun 2005.

[47] LHCb tracking group, *https://twiki.cern.ch/twiki/bin/view/LHCb /LHCbTracking*, June 2012.

[48] LHCb tracking results, *https://twiki.cern.ch/twiki/bin/view/LHCb /TrackingEffStatusUpdated*, July 2012.

[49] LHCb Gauss group, *http://lhcb-release-area.web.cern.ch/LHCb-release-area/DOC/gauss/*, April 2012.

[50] Pythia group, *http://home.thep.lu.se/ torbjorn/pythiaaux/recent.html*, April 2012.

[51] T. Sjostrand, S. Mrenna, and P. Z. Skands, *PYTHIA 6.4 Physics and Manual*, *JHEP* **0605** (2006) 026, [arXiv:hep-ph/0603175].

[52] GEANT4 collaboration, J. Allison et al., *Geant4 developments and applications*, *IEEE Trans.Nucl.Sci.* **53** (2006) 270.

[53] GEANT4 collaboration, S. Agostinelli et al., *GEANT4: A simulation toolkit*, *Nucl. Instrum. Meth.* **A506** (2003) 250.

[54] LHCb collaboration, *http://lhcb-release-area.web.cern.ch/LHCb-release-area/DOC/boole/*, May 2012.

[55] LHCb collaboration, *http://lhcb-release-area.web.cern.ch/LHCb-release-area/DOC/brunel/*, May 2012.

[56] LHCb collaboration, *http://lhcb-release-area.web.cern.ch/LHCb-release-area/DOC/moore/*, May 2012.

[57] LHCb collaboration, *http://lhcb-release-area.web.cern.ch/LHCb-release-area/DOC/davinci/*, May 2012.

[58] D. Xu, *Measurement of QED Final State Radiation in $Z \to \mu\mu$*, 2011.

[59] P. Golonka and Z. Was, *PHOTOS Monte Carlo: a precision tool for QED corrections in Z and W decay*, arXiv:CERN-PH-TH/2005-091.

[60] W. Verkerke and D. P. Kirkby, *The RooFit toolkit for data modeling*, *eConf* **C0303241** (2003) MOLT007, [arXiv:physics/0306116].

[61] W. Verkerke and D. P. Kirkby, *RooFit Users Manual v2.07*, 2006.

[62] S. van der Meer, *Calibration of the effective beam height in the isr. oai:cds.cern.ch:296752*, Tech. Rep. CERN-ISR-PO-68-31. ISR-PO-68-31, CERN, Geneva, 1968.

[63] Y. Amhis et al., *Absolute luminosity measurements at* $\sqrt{s}$ *= 7 tev*, Tech. Rep. LHCb-INT-2011-018. CERN-LHCb-INT-2011-018, CERN, Geneva, May, 2011.

[64] LHCb Collaboration, R. Aaij et al., *Absolute luminosity measurements with the LHCb detector at the LHC*, *JINST* **7** (2012) [arXiv:1110.2866].

[65] Particle Data Group, J. Beringer et al., *Review of particle physics*, *Phys. Rev.* **D86** (2012) 010001.

[66] G. Lanfranchi et al., *The muon identification procedure of the lhcb experiment for the first data*, Tech. Rep. LHCb-PUB-2009-013. CERN-LHCb-PUB-2009-013, CERN, Geneva, Aug, 2009.

[67] CTEQ collaboration, *CTEQ6LL - http://vircol.fnal.gov/LHAPDFv1/cteq6ll.LHpdf*, May, 2012.

[68] J. S. Anderson and R. McNulty, *Testing the electroweak sector and determining the absolute luminosity at LHCb using dimuon final states.* PhD thesis, University College Dublin, Dublin, 2008. Presented on 18 Nov 2008.

[69] RD5 Collaboration, M. Aalste et al., *Measurement of hadron shower punchthrough in iron*, *Z.Phys.* **C60** (1993) 1–10.

[70] M. De Cian, *A measurement of the tracking efficiency for high-*p_T *tracks in reco06-stripping10 collision data.*, Tech. Rep. LHCb-INT-2010-058. CERN-LHCb-INT-2010-058, CERN, Geneva, Dec, 2010.

[71] LHCb luminosity group, *https://twiki.cern.ch/twiki/bin/viewauth/LHCbPhysics/LuminosityMeasurements*, June 2012.

[72] F. Landry, R. Brock, P. M. Nadolsky, and C. Yuan, *Tevatron Run-1 Z boson data and Collins-Soper-Sterman resummation formalism*, *Phys.Rev.* **D67** (2003) 073016.

[73] G. Ladinsky and C. Yuan, *The Nonperturbative regime in QCD resummation for gauge boson production at hadron colliders*, *Phys.Rev.* **D50** (1994) 4239.

[74] P. Nason, *A New method for combining NLO QCD with shower Monte Carlo algorithms*, *JHEP* **0411** (2004) 040.

[75] S. Alioli, P. Nason, C. Oleari, and E. Re, *A general framework for implementing NLO calculations in shower Monte Carlo programs: the POWHEG BOX*, *JHEP* **1006** (2010) 043.

[76] S. Alioli, P. Nason, C. Oleari, and E. Re, *NLO vector-boson production matched with shower in POWHEG*, *JHEP* **0807** (2008) 060.

[77] FEWZ group - Argonne National Laboratory, *http://gate.hep.anl.gov/fpetriello/fewz.html*, August, 2012.